Measurement and Control of Slip-Flow Boundary Conditions at Solid-Gas Interfaces

Dongjin Seo

Dissertation submitted to the faculty of the Virginia Polytechnic Institute and State University in partial fulfillment of the requirements for the degree of

Doctor of Philosophy

In

Chemical Engineering

William A. Ducker

Mark R. Paul

Richey M. Davis

Stephen M. Martin

September 26th, 2014

Blacksburg, Virginia

Keywords: gas, slip flow, accommodation coefficient, boundary condition, lubrication

Measurement and Control of Slip-Flow Boundary Conditions at Solid-Gas Interfaces

Dongjin Seo

ABSTRACT

This thesis describes measurements of the gas-solid flow boundary condition at moderate Knudsen number, i.e., where the dimensions of the flow are similar to the mean free path, and thus partial slip is expected. This regime has become more important with increased focus on nano-scale devices, but there is currently no consensus on how the slip length should vary for different solids and gases, or whether it can be controlled. In this thesis, I describe unambiguous measurements showing that partial slip occurs, that the slip length depends both on gas and solid, and that the slip length can be altered in situ. The slip length is determined from analysis of the vibration of a small sphere adjacent to a solid. I also describe applications of these findings both to the separation of gases, and to inhalants.

The effect of water films, gas species, organic films, and electric fields on gas flow was studied. Water films had a large, but complex effect. On bare hydrophobilic glass, the tangential momentum accommodation coefficient (TMAC) for nitrogen on hydroxyl-terminated silica changed from 0.25 to 0.88 when the humidity changed from 0 to 98 %. On hydrophobized glass, TMAC changed from 0.20 to 0.56 in the same range.

The effect of the gas on TMAC was measured for five different gases (helium, nitrogen, argon, carbon dioxide, sulfur hexafluoride) on octadecyltrichlorosilane-coated glass surfaces. A lower TMAC occurred for greater molar mass, and this trend was explained using a simple model representing both the gas and the monolayer by spheres. The existence of this gas-dependent difference in TMAC suggests that gases can be separated based on their collisions with surfaces.

Methods for controlling the flow boundary condition were also developed by adsorbing monolayers on the solid, and altering the monolayers in situ. Both temperature and electric fields altered the boundary condition, and these changes were attributed to changes in the surface roughness. The effect of roughness was modeled with grooved surfaces. Possible applications of this effect of roughness include changing the flow of aerosol droplets for deeper delivery of therapeutic drugs into the lung.

Acknowledgement

My Ph.D. work so far would have been impossible without the people who have supported me in many different ways, providing emotional reinforcement, intellectual and scholastic support.

I am so thankful for my wife, Hyunjung Cheon, who have trusted, waited and endured for six long years during my journey through becoming a Ph.D., which might have seemed obscure and not promised at the start of my master's degree courses. She has supported me ever since from our start. I also like to thank my children, Lyeoun, Yuru, Jiwhon, who come running toward me with big smiles on their faces when I return home. I also like to thank my mother and deceased father who raised me and supported my interest in science.

Many thanks to my mentor, Dr. William Ducker, who have been patient in guiding me through my Ph.D. He helped me understand how to become a careful and thorough scholar in science by painstakingly explain the principle telling me where to find the solutions and how to use them. I also thank Dr. Mark Paul in Mechanical Engineering, who also patiently taught me about cantilevers to the one who had little knowledge in mechanical engineering. Dr. Walz, now in University of Kentucky, also provided me with much insight in surface science during group meetings.

I also like to thank my lab mates, Dmitri, Dean, Milad, Chiu, David, Greg, Wenli, Prudvi, Shunxi, and others. I thank Brian Robbins in Mechanical Engineering for his willingness to help me in simulations and computational research.

Finally I like to thank my Heavenly Father who gave me this great opportunity.

September 26th, 2014

Dongjin Seo

Table of Contents

List of Figures

Chapter 1

Chapter 2

Chapter 3

Chapter 4

Chapter 5

Chapter 6

Chapter 7

Chapter 8

Chapter 9

Note: The number for the first figure in each chapter starts at 1.

List of Tables

Chapter 3

Chapter 5

Chapter 7

Note: The number for the first table in each chapter starts at 1.

Attribution

The result and discussion in Chapter 4. Effect of Humidity on Slip Boundary Condition includes the calculation according to Lifshitz theory showing van der Waals force between two glass bodies. This calculation was done by Dean Mastropietro who used to be my colleague in Dr. Ducker' lab. He is one of the authors for the paper presented in Chapter 4. He is a now postdocoral research in Chemical Engineering Department at University of Illinois at Urbana Champagne.

Chapter 1. Introduction

1.1. Purpose

My purpose for implementing the series of research projects presented in this dissertation is to find both the principles that determine gas flow near solid surfaces in the high Knudsen number region, and also methods of controlling the flow that may impact applications. The Knudsen number is the ratio of mean free path, λ, to the characteristic length of the system, L, or $Kn = \lambda/L$. A high Knudsen number means the average travel distance of fluid molecules is comparable to the system size. This implies a greater number of interactions between the fluid molecule and system boundary (usually solid or liquid) than between two fluid molecules. For a low Knudsen number, information from collisions with the boundary is lost over a small distance through gas–gas collisions. For high Knudsen number, the lack of gas–gas collisions compared to gas–boundary conditions offers the opportunity to control the flow via modification of the solid.

High Knudsen number occurs for low pressure or for small devices. Since mean free path is inversely proportional to pressure, low pressure situation would lead to high Knudsen number, even for macroscopic objects. One such example is gas flow in the space or at high altitude. There are numerous satellites in different orbits. This orbit altitude can change Knudsen number significantly. Space vehicles are under similar conditions. Vashchenkov et al.[1] simulated a reentry vehicle returning to earth from 120 km to 60 km altitude and calculated the drag force. They reported that the drag force on the surface changed according to altitude while the Knudsen number changes from 3.7×10^{-4} to 4.3×10^{-3}. The situation is similar on other planets, except that the atmospheric pressure and composition is different. For example, on Mars, the pressure is about 100 times lower and the atmosphere is mainly CO_2.[2]

The progress of micro- and nanotechnology and the applications toward the small systems requires understanding of fluid flow in small scales.[3] At atmospheric pressure, bulk fluid flow is affected little by the fluid-solid interaction, since most of the molecules in the systems exist far away from the boundary of the system. However, in nanosystems, the interaction of molecules with the solid boundary is much more frequent compared to bulk systems. This requires a deeper understanding in fluid behavior in micro- and nanoscales.

The lab-on-a-chip devices, for example, use micron-sized devices where the mean free path is comparable to the dimensions. Martini *et al.*[4] devised a conductivity meter that can detect ammonia concentration from 10 to 100 ppm. They first simulated their system with different dimensions for the best fluid transport. Velasquez-Garcia *et al.*[5] fabricated an electron impact ionizer (EII) with carbon nanotubes installed in microsystems. EII is usually used to ionize a neutral gas for detection in mass spectroscopy. This carbon nanotube systems intakes neutral gases into a micron-scale system, ionizes the gases, and emit them. Understanding fluid flow in these small systems would better explain both fabrication and operation of this EII.

High Knudsen number flow is also achieved in human lungs. Although the entrance is macroscopic, lungs branches to smaller tubes (alveoli) that may reach up to $Kn \sim 0.001$. Knowledge of the flow in these tubes is necessary to accurately model the delivery of inhalants that are used as therapies. The principal objective is to prevent premature deposition at the entrance so that the drug is delivered to the narrow tubes where oxygen is exchanged.[6]

A final example of high *Kn* is in head/hard disk lubrication. If actual physical contact is made between two, the disk would be damaged, resulting in loss of stored data. The gap should be kept to a minimum for the head to detect small magnetic field from the disk (down to several nanometers[7]). Therefore the flow of gap between the two is at high *Kn*.

The examples introduced here show that the system with high Knudsen number, either with low pressure or small characteristic length, can show different fluid behavior. From these and other literature, understanding fluid flow in high Knudsen number flow regime can be led to many different scientific and engineering applications. Therefore I wanted to understand the fluid behavior at this regime, especially in small systems.

I mainly mentioned the gas systems in the previous section. Since the mean free path of gas is much larger than that of liquid, the interaction of gas molecules with the solid is much greater in the same dimensions, and the effect of solid is more prominent at gas-solid surfaces. Therefore it was my purpose to understand the effect of solid in gas behavior, in the range where this interaction affects the flow. However, there would be many factors changing the behavior. Though there were many who investigated those factors, I want to explore the variables from my own decision.

I began this investigation by first examining the possibility of using atomic force microscope (AFM) cantilevers as detectors for gas behaviors. Later in this document, the way of using cantilevers as pressure gauge based on density measurement will be described. The next step was to find out the boundary condition change according to two parameters: water film thickness on solid and different species of gases. The final step was to control boundary condition *in situ* with the help from molecules on surfaces responding to external stimuli.

My intent of taking these steps was to find the novel ways of controlling boundary conditions, and understand the effect of non-controllable boundary condition properties of systems to fluid flow.

1.2. Theory

1.2.1. Thermal Motion of Small Object

According to the equipartition theorem[8, 9], a continuum object at a temperature, T, has ½ k_BT of energy in each mode of motion where k_B is Boltzmann constant. This small energy makes objects undergo random vibration, but this motion is usually unnoticed or insignificant in macroscopic objects. For a small and low-stiffness object such as an AFM cantilevers is considered, thermal energy is enough to make it vibrate a few nanometers. The amplitude of vibration is square root of k_BT/k. The collective and averaged motion of a bar-like object, in my case, cantilevers, at a certain temperature in vacuum as well as in fluid is known through the research from Boskovic et al. and Paul et al.[10-12] When the object is surrounded by fluid, this small vibration is affected by fluid conditions and characteristics, such as temperature, pressure, viscosity, density, and so forth. Although at first sight the effect of fluid properties on these vibrations might appear to be complex, the fluctuation-dissipation theorem tells us that the stochastic motion (thermal vibrations) are simply related to the motion that occurs when during the deterministic motion of the cantilever in the linear regime. In case of cantilever fluctuations in fluid, the autocorrelation of deflection of cantilever from the equilibrium position is proportional to the deterministic displacement of the unclamped end of the cantilever after the removal of a step force, F[11]:

$$\langle x(0)x(t)\rangle = \frac{k_BT}{F}X(t), \tag{1}$$

where x is the stochastic deflection of the cantilever tip, t is the time, ⟨ ⟩ denotes an equilibrium ensemble average, and the force was applied at some time in the distant past. This equation signifies that the stochastic motion of cantilever can be interpreted as a ring-

down of harmonic oscillator as it being released from a certain force F. Because the deterministic ring down depends on the fluid properties in a known way, the fluid properties can be calculated by monitoring thermal deflection of cantilevers. In this dissertation, I found the density of gas and hence the pressure of fluid by comparing experimentally measured thermal fluctuations to the theoretical estimates of the fluctuations that were calculated from the deterministic ring down using Eq. (1). The advantage of using fluctuations to measure viscous properties are that no external drive is required and there is no external perturbation of the system, the system simply vibrates with its own thermal energy.

Fluctuations were also used in this thesis to measure the stiffness of AFM cantilevers (Section 2.4.1).

1.2.2. Slip Boundary Condition

It is usually assumed that the fluid flow velocity at solid boundaries is zero, "the no-slip boundary condition," for bulk or macroscopic systems. This assumption is valid for many industrial and practical applications. This no-slip boundary condition at the solid surface arises from two effects: (1) most surfaces are rough, such that the reflections of gas molecules are diffuse – all angles of reflection are equally probable– and thus there is zero net tangential velocity and momentum at the surface; and (2) for macroscopic systems, collisions with other gas molecules occur in such a small distance from the solid that details of the momentum change from the solid are forgotten a small distance away from the solid, and therefore affect a negligible fraction of the entire flow. However, when the characteristic length of the flow approaches the mean free path, the details of the surface collision propagate into a significant fraction of the flow and surface effects cannot be ignored. Therefore, the Knudsen is a useful number to characterize the flow. If Kn <0.001,

the no slip condition is appropriate, for *Kn* between 0.001 and 0.1, the system is in slip flow regime.[13-15] Here the continuum description is appropriate, but with the use of a partial slip boundary condition to account for the surface effects. For *Kn* > 1, the flow cannot in general be described accurately using a continuum approach. The measure of how much fraction of momentum along the surface is conserved after molecules collide with surfaces is called the tangential momentum accommodation coefficient (TMAC), σ, and is defined as:

$$\sigma = \frac{p_{x,i} - p_{x,f}}{p_{x,i}}, \tag{2}$$

where p_x is the average gas momentum tangent to the solid surface, and *i* and *f* refer to the momentum before and after the collision. If the tangential momentum is conserved on average, the numerator is zero, thus $\sigma = 0$, referred as specular reflection. Because the tangential momentum is unchanged the slip length, *b*, is infinite. The slip length is considered to be the extra distance of fluid that would be required to give the same flow. If no average tangential momentum is conserved, $\sigma = 1$, referred as diffuse reflection, which results in the minimum slip length. Note that the minimum is not zero, it is approximately equal to the mean free path. The slip length thus has an enormous range: from the mean free path to infinite.

Many people have studied the relationship between the slip length and the accommodation coefficient, for example, Maxwell showed that:[16]

$$b = \lambda\left(\frac{2}{\sigma} - 1\right). \tag{3}$$

There are others who modified or revised the equation for specific circumstances.[17-19] For example Lilley and Sader[18] used the calculation result from Direct Simulation Monte Carlo method to relate the slip length with TMAC as follows:

$$b = \lambda\left(\frac{2.01}{\sigma} - 0.73 - 0.16\sigma\right). \quad (4)$$

Tekasakul et al.[20] used a spinning rotor gauge to measure the slip length of different gases. By comparing the theory they developed to the actual measurement, they reported the following relation between TMAC and the slip length.

$$b = \lambda\frac{2-\sigma}{\sigma}\left[(1-\sigma)\frac{\sqrt{\pi}}{2} + 0.9875\sigma\right]. \quad (5)$$

The calculated slip lengths over mean free path (b/λ) as function of TMAC with each equation (Eqs. (3), (4) and (5)), are shown in Figure 1(a) of this chapter. Figure 1(b) shows the relative errors calculated as (Maxwell value – comparing value)/(Maxwell value). The deviation of each equation is less than 11 % in the TMAC range from 0.2 to 0.9, which are the lowest and highest values reported in this dissertation. Since other equations provide little deviation from Eq. (3) in the range of my experiment, the TMAC values presented in this thesis were calculated using Maxwell's equation, Eq. (3).

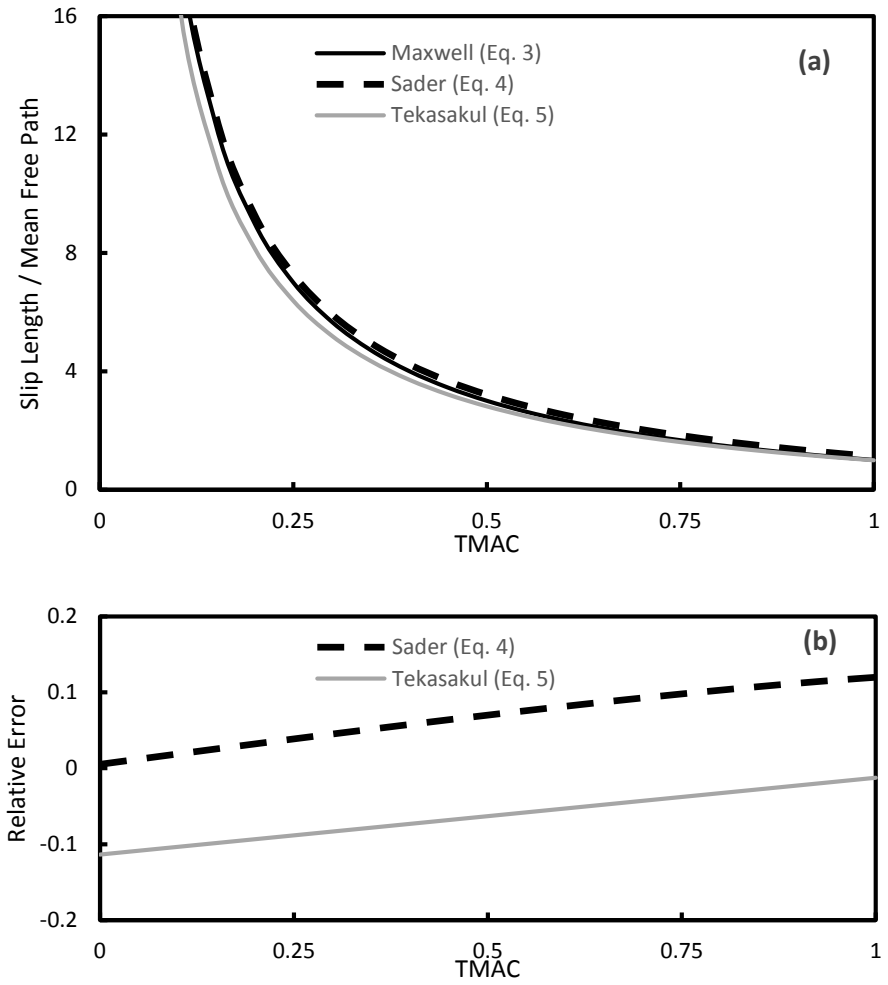

Figure 1. (a) Calculated slip length/mean free path (b/λ) according to three different equations suggested by Maxwell (Eq. (3), solid black line), Sader (Eq. (4), black dash lines), and Tekasakul (Eq. (5), solid gray lines). (b) Relative error of Eq (4) and Eq. (5), respectively, compared to Eq. (3).

Since TMAC is not directly measured, in this thesis, it was inferred from the slip length. However, the slip length is also not a directly measured quantity, but is normally obtained by fitting to a measured flow. Therefore, the equation or model relating slip length to some other measurable quantity was sought. Vinogradova[21] provided a model which relates slip

length to the force, F, on a sphere surrounded by a fluid, viscosity, μ, when the sphere approaches the plate normal to a wall with velocity, v. She assumed slip lengths from both surfaces were much smaller than the radii of spheres. In this thesis, my interest is in the damping for a vibrating sphere, $D = F_{\text{damp}} / v$. When a sphere is far from any object, it undergoes damping due to surrounding fluid. When the sphere is closer to other objects the damping increases due to restriction of flow in the channel between the two objects. The increase in D due to proximity to the wall is defined as $D_{lub} = D(h) - D(\infty)$, where $D(h)$ is the damping at separation, h. For the case in which two spheres approaching each other, and at the limit where the radius of one sphere is infinite (flat surface), D_{lub} is:[22]

$$D_{lub} = \frac{6\pi\eta r^2}{h} f^*, \tag{6}$$

$$f^* = -\frac{2\alpha h}{\beta\gamma} - \frac{2h}{\gamma-\beta}\left[\frac{(\beta+h)(\beta-\alpha)}{\beta^2}\ln\left(1+\frac{\beta}{h}\right) - \frac{(\gamma+h)(\gamma-\alpha)}{\gamma^2}\ln\left(1+\frac{\gamma}{h}\right)\right], \tag{7}$$

$$\begin{aligned} \alpha &= b_1 + b_2\,, \beta = 2b_1\left(2+q+\sqrt{1+q+q^2}\right), \\ \gamma &= 2b_1\left(2+q-\sqrt{1+q+q^2}\right), q = \frac{b_2}{b_1} - 1, \end{aligned} \tag{8}$$

where r is the radius of a sphere when the other is flat surface (infinite radius), h is the separation, η is dynamic viscosity of fluid, and b_1 and b_2 are the slip lengths of the two solids. Therefore, the relation between measurable variables, D_{lub}, η, h, and, r, and slip length is known.

When the sphere and plate have the same slip length, Eqs. (6) to (8) reduces to

$$D_{\mathrm{lub}}(h) \;=\; \frac{6\pi\eta r^2}{h} f^*(h,b), \tag{9}$$

where $f^* = \frac{h}{3b}\left[\left(1+\frac{h}{6b}\right)\ln\left(1+\frac{6b}{h}\right)-1\right]$.

The effect of slip length on Normalized $D_{\mathrm{lub}} = D_{\mathrm{lub}}(h)/(6\pi\eta r^2)$ is calculated as a function of slip length and separation in Figure 2. Note that the effect of the slip length becomes more pronounced at smaller h. Recall that the slip length is proportional to the mean free path, so for a fixed accommodation coefficient, the variation in slip length could be considered to be due to changes in mean free path, for example by changing the pressure of the gas.

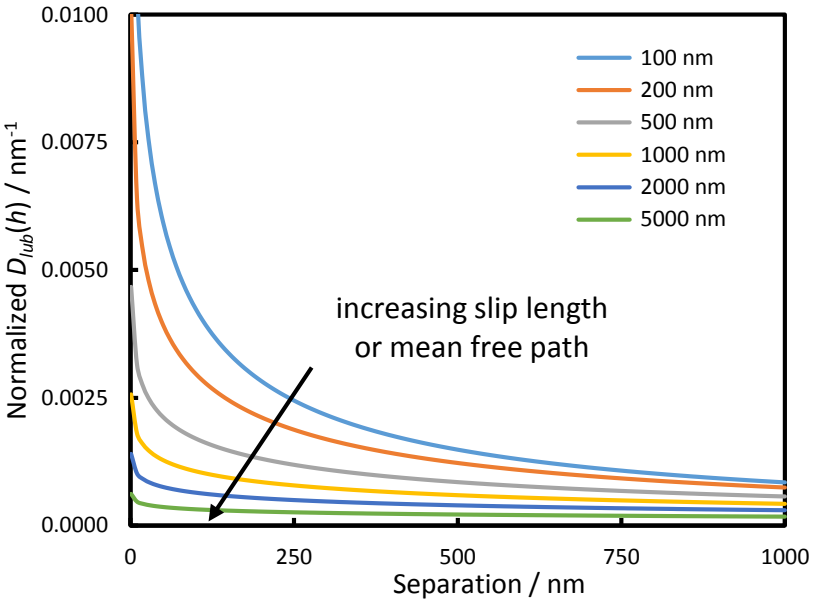

Figure 2 Effect of slip length and mean free path on lubrication

1.3. Literature Review

1.3.1. Pressure Measurement with Cantilevers

There are many different kinds of pressure gauges. In this section, the ones closely related to my research will be discussed, namely pressure measurement with cantilevers. Many of them are related to measuring quality factor, Q. When an oscillating object is concerned, the quality factor describes how much energy is dissipated after a cycle. For example, the energy dissipation of vibrating cantilever is low at vacuum since nothing except for the internal damping hinders the cycle, making Q higher. However, if the same cantilever is surrounded by a fluid, Q becomes lower.

When one specific gas is concerned, higher pressure would result in lower Q since there are more molecules interacting with the cantilever. This is the principle Bianco *et al*.[23] used to related Q to pressure, P. They observed the behavior of microfabricated cantilever and related the parameters from the behavior with theories presented by Christian,[24] Bao *et al.*[25], and Hosaka *et al*.[26] By finding the relation between Q and resonance frequency, they presented a way to use their cantilevers as a pressure gauge. Lissandrello *et al.*[27] observed the behavior of a double-clamped micron bridge throughout all fluid regimes to characterize each regime with theory. They also found that Q is inversely proportional to the square root of pressure. Other researchers[28, 29] also calculated the pressure using the theory by Christian[24] and Hosaka et al.[26] They also reported that $Q \sim 1/P^{1/2}$ in the continuum regime and $Q \sim 1/P$ in the molecular regime. Boskovic et al.[10] made a further use of cantilevers by measuring density and viscosity of fluid. All these examples clearly shows that cantilever can be used to measure fluid properties

1.3.2. Slip Length and TMAC Measurement

As stated earlier, tangential momentum accommodation behavior is closely related to slip length. There are many researchers who studied TMAC with different methods in different circumstances.

One such method is spinning rotor gauge (SRG), mainly developed to measure different fluid properties and parameters such as viscosity and drag coefficient. This same technique has been used to measure tangential momentum accommodation.[20, 30-33] The principle is measuring deceleration of a spinning sphere after it is released with a known momentum and angular velocity. Then the impingement of surrounding molecules in different circumstances would show different deceleration. If this difference is from gas species, for instance, the relation between gas species and TMAC can be known. One example of measuring TMAC with spinning rotor gauge is a work by Tekasakul et al.[20] in which they prepared a steel sphere in a closed tube, and controlled the angular velocity of the sphere, which is magnetically levitated. After measuring initial angular velocity, the sphere was freed from other forces but the impingement of gases inside. The torque data was compared with the theory from Loyalka[34] to extract slip length. This slip length was converted to TMAC with Eq. (5).

Another method is by measuring flow in a microchannel.[35-37] Colin et al.[35] used a rectangular microchannel made from silicon wafer and Deep Reactive Ion Etching to form rectangular shapes and other micron-scale features. They measured the flow rate and pressure drop of helium and nitrogen at low pressure, and compared them with a model. The model they have used is based on second-order slip model under the assumption (later proved true with experiments) that first-order slip model underestimate the flow rate. This

model by Deissler[38] provides solution to Navier-Stokes equation on a wall at high *Kn*, which was further simplified to be used in the rectangular geometry.[39] TMAC was used as a fitting parameter to better align the data and the model. They reported the model with TMAC = 0.93 for both nitrogen and helium to best represent the experiments.

Arkilic *et al.*[37] also used microchannels to calculate TMAC of different gases on a single-crystal silicon surfaces near atmospheric pressure. They also solved the Navier-Stokes equation yielding one term for continuum and the other to account for slip flow. They did not use the second-order slip but Maxwell model. (See Eq. **(**3)) They reported TMAC values less than unity, ranging from 0.75 to 0.85.

There is also a method using microstructures and interpreting their behavior when surrounded fluid at different conditions. For example, Laurent *et al.*[40] measured the slip length of air and helium when they are squeezed between gold plate and gold sphere. This is essentially the same method as used in this thesis. They found that slip length at low pressure is very high. According to Eq.(3), slip length is high when mean free path is long, which is common in low pressure. Therefore relation between pressure and slip length is confirmed.

Honig et al.[41] studied the effect of surface coating. After attaching a glass sphere to a cantilever, they measured the thermal motion of cantilever as a function of separation between the sphere and a glass plate. The slip length of a clean glass surface was reported to be 630 ± 90 nm, while that of methylated surface was 270 ± 90 nm.[41] This experiment shows the effect of surface coating to boundary conditions.

However, there is little consensus on TMAC. Arkilic *et al.*[37]measured TMAC of nitrogen gas measured in micromachined silicon channel. They reported the TMAC were between 0.75 and 0.85 while Colin et al.[35] reported 0.93 in a similar system. Hsieh et al.[42] reported that TMAC is between 0.3 – 0.7 for nitrogen in oxidized silicon channel. I believe this difference arise from details from fabrication, such as roughness or contamination. My interest was to measure TMAC in well-defined surfaces like methylated surfaces from Honig et al.[41]

The effect of gas species has also been investigated. One of such reports is that of Cooper *et al.*[43] reporting TMAC values for nitrogen, along with oxygen and argon. His value was 0.52 ± 0.1 for all three. Arya *et al.*[44] simulated the collision of different gas species with solids. Their results showed that different gas properties can lead to difference in TMAC. Sedmik *et al.*[45] measured lubrication of different gases between gold-coated spheres and gold-coated plates. This lubrication was interpreted into TMAC. They reported the relation between mean free path of gas species and the TMAC. They reported as mean free path became smaller, TMAC became lower. There is no consensus on whether or not different gas species have different TMAC according to the reports previously mentioned and others.[46-48] However, prior to this thesis, there was no work on functionalized surfaces other than Honig *et al.* My intention was utilizing a functionalized surface for TMAC measurement, to see if different gases exhibited different TMACs. Since different species should interact differently with the monolayer, I expected that the TMAC should vary according to the species.

Chapter 2. Methods

2.1. General Experiment Setup and Procedure

This section presents a typical setup for the experiments that are described in Chapter 4 to Chapter 7. For better understanding, a schematic is shown in Figure 1 of this chapter.

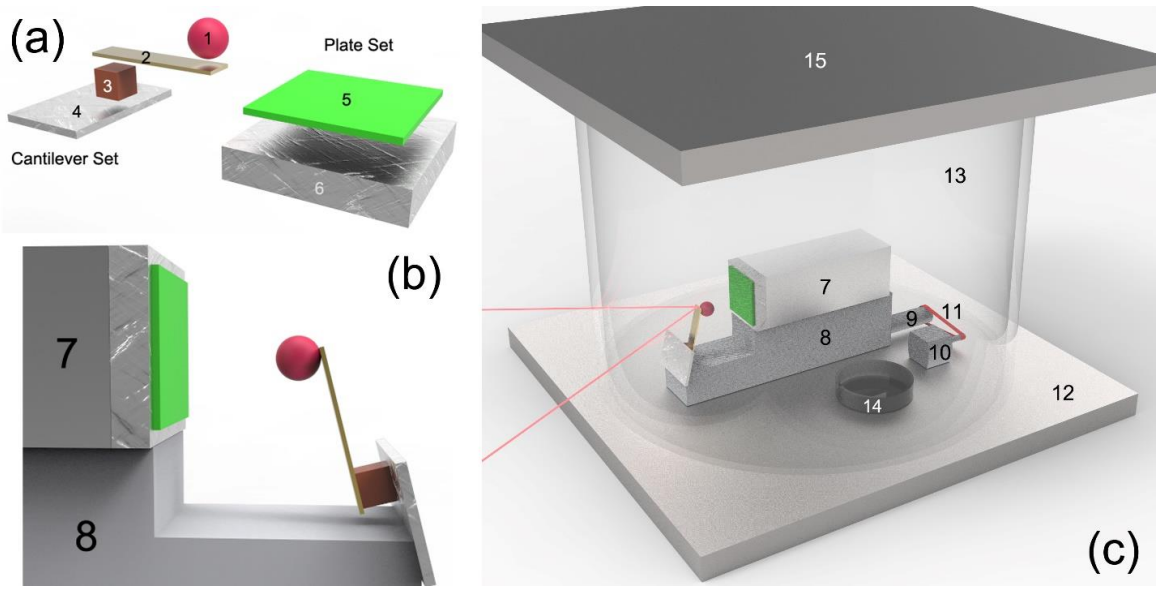

Figure 1 Schematic for the assembly of different parts and samples. Note that neither scale nor dimensions are correct. In particular, the sphere (1) is positioned on the cylinder axis such that the laser beam strikes approximately normal to the surface of the glass chamber (13).

The first step is to prepare samples. When I refer to 'samples', I mean a glass spheres or a plate, each of which can also be coated in gold or an organic monolayer. A glass sphere (nominal diameter 30 μm, Duke Standard Cat. No. 9030, Thermo Scientific), #1, is attached to a cantilever (ORC8-10, D cantilever, Bruker Co.), #2 using heat responsive epoxy glue to form a "colloidal

probe." The colloidal probe is attached to a small piezoelectric crystal (PL022.31, Physik Instrumente GmbH & Co. KG.), #3, which is used to vibrate the colloidal probe. The changes is frequency and amplitude of this vibration are used to sense the damping. The piezoelectric crystal was previously glued to a custom-made aluminum plate, #4, with screw bit holes. While the steps so far are performed, the plate sample, #5, were prepared and attached to another aluminum piece, #6. After the cantilever set comprised of #1, #2, #3, and #4, and the plate set made of #5 and #6 are all ready, they are irradiated with α-polonium source (Static Master). This irradiated results in an electrostatically neutral surface, which removes the large forces that are associated with static charge. The plate set is attached to the piezoelectric crystal translational stage (P-753K082, Physik Instrumente GmbH & Co. KG), #7, which is attached to a micron-level translational stage, #8. The piezoelectric crystal (#7) is used to change the separation between the sphere and plate over the range 0–15 μm and the translation stage is used to change the separation over the range 1μm –5 mm. The cantilever set is then attached to #8 of which position is controlled by the knob, #9, a part of #8. Parts #1 to #9 are bolted to the bottom plate, #12.

Experiments on the damping are performed in a controlled environment, either vacuum, controlled humidity, or in a specific gas, by enclosure in an airtight chamber, which consists of the bottom plate, a glass cylinder (#13) and the top plate (#14). The bottom plate has an o-ring grove to constrain a Viton o-ring for maintaining a seal against the glass cylinder. It also has through-hole for the passage of eight electrical wires. Because only moderate vacuums were required for this work, the seal in this hole was made by simply filling with instant epoxy glue which cures by mixing two components. To operate the micrometer without breaking the seal, control knob #9, was turned using a rubber band #11 that was driven by a DC motor, #10. The wires are connected to each relevant part: two for #3, two for #10, two for thiolated gold plate,

#5, in Chapter 7, and two in reserve. Immediately prior to sealing the chamber, a small petridish filled with dry silica gel, #14, is placed inside, which helps to remove water.

The top plate, #15, has three electric feed-throughs for control of the piezoelectric drive, two valves to introduce or excavate gas, and one connection hole for the pressure gauge, thermometer, or humidity meter, all of which are not shown in Figure 1, but marked with a red arrow in part (a) of Figure 2 in this chapter. Two wires for #3 are connected to a lock-in amplifier, two for #10 to a function generator, and two for #5 also to the function generator. Three connectors on #15 are connected with a data transfer cable to the controller. Laser from a source (681 nm, Schäfter+ Kirchhoff GmbH) is focused on the back of the cantilever #2, of which reflection is focused to a split photodiode (Phresh Photonics). The laser mount with lens and the diode were mounted on rigid rods which were screwed into an optical breadboard. After positioning the laser so that the laser path was toward the cantilever, the focus and alignment was made with knobs on the mount which allowed movement in a few millimeters vertically and horizontally. After the laser was aligned, the photodiode was aligned by changing the position of the diode so that the measured laser intensity would be the maximum. Then, the vertical and horizontal alignments were made by zeroing both signals (refer to Section 2.2.1).

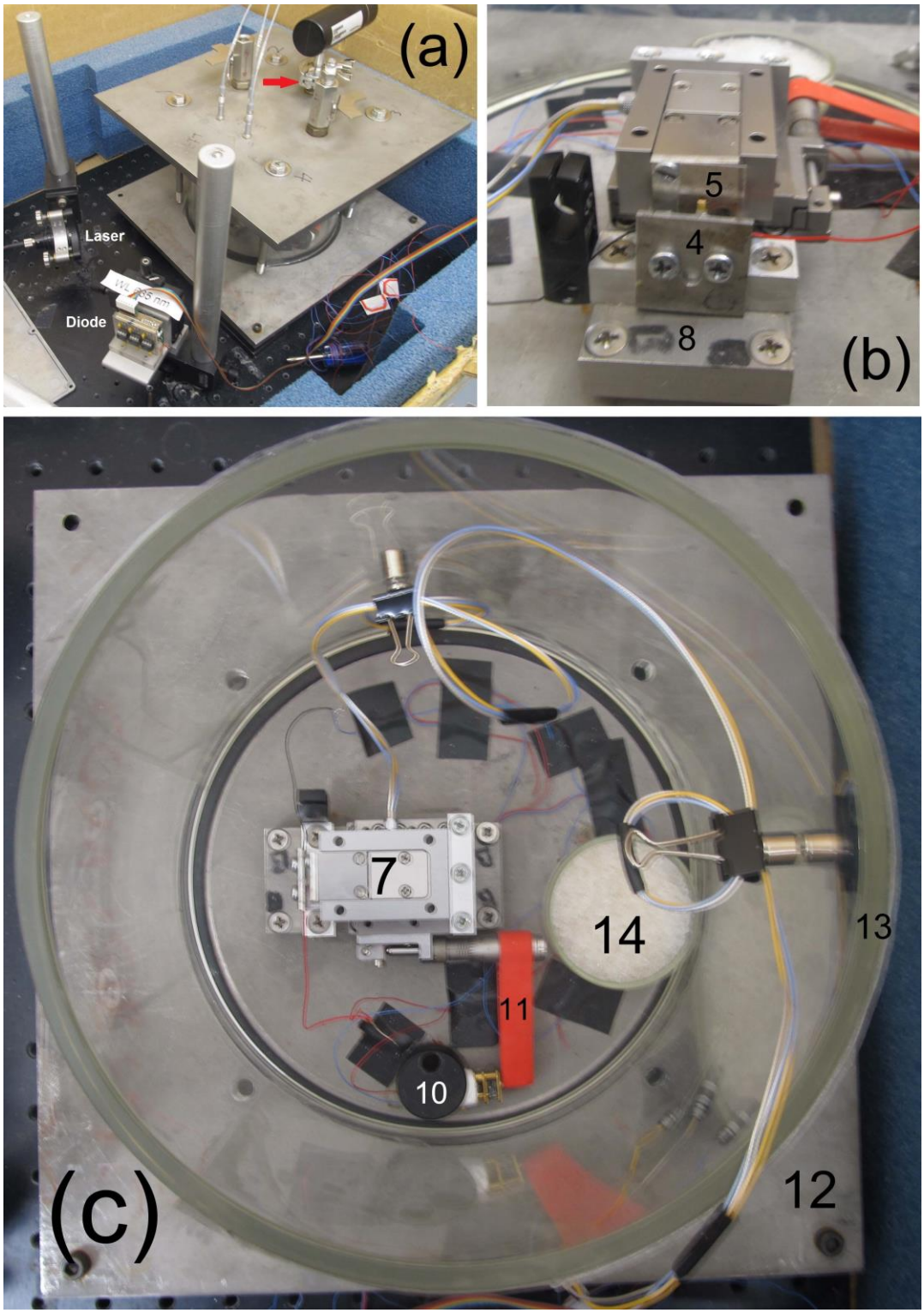

Figure 2. Photographs of the experiment with part numbers labeled.

2.2. Equipment and Materials

2.2.1. Atomic Force Microscopy

Since its development in 1986, AFM was used not only for imaging but also for many other purposes, including usage as biological and physical sensors[49, 50] These applications are based upon the fact that small objects like cantilevers are subject to small forces, such as thermal energy or damping from the fluid. The technique capturing this small deflection was also needed in capturing small forces. Conventional AFMs use light-lever technique along with split photodiodes in measuring endslope of cantilevers from equilibrium position. This endslope can be converted into deflection by examining the change in endslope when the probe is in contact with a rigid solid, and then into force using the spring constant.

Ducker *et al.*[51] developed a way to measure force between colloidal particles and a planar surface by attaching a colloidal sphere at the end of cantilever. This technique not only allows direct measurement of force, but also make it easier to set up a model by simplifying the geometry. The sphere-plate geometry was used for all slip length and TMAC measurements in my research.

The deflection of free end of cantilever was detected by focusing laser at the end, then detecting the reflective laser with split photodiode. The split photodiode has four sectors, here called Parts A, B, C, and D, as shown in part (a) of Figure 3 in this chapter, in which each measure the intensity of light falling on that sector. The magnitude of the sum signal (A+B+C+D) can be used to determine whether the laser is completely on the diode. The position of the reflected laser beam can be determined from other combinations of the four

signals. For example, (A+B)-(C+D) gives the vertical deflection and (A+C)-(B+D) gives the horizontal deflection.

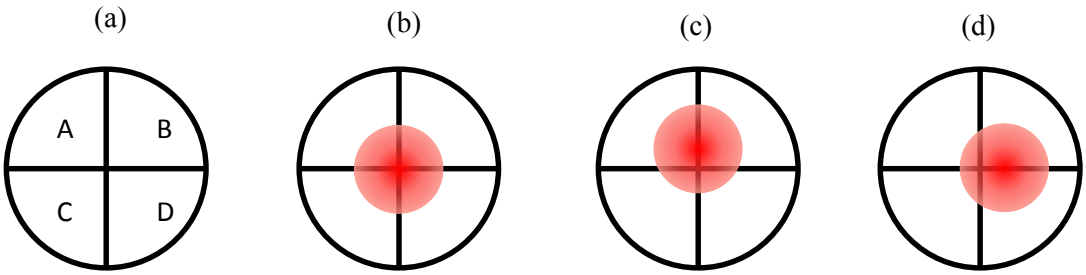

Figure 3. Example of laser incident on a photodiode when detecting the two dimensions of cantilever deflection

The photodiode output is in voltage. Therefore, a factor is needed to convert the voltage to deflection in meters. This value can be obtained by first letting the cantilever make contact with a rigid surface. I will assume at the initial contact, the focus on the diode looks like part (b). If the cantilever or the surface moves toward the other with a known distance, for example 10 nm, there would be change in the location of the focus, for example as in part (c). Assume that the value (A+B)-(C+D) = 0.2 mV. Therefore, 0.2 mV corresponds to 10 nm. Thus the voltage output of the diode can be calibrated for all deflections using the calibration of 0.02 mV/nm.

2.2.2. Lock-in Amplifier

In Section 2.4, I will discuss how I measured damping of fluid between solid surfaces. One of two methods is what I call ‘driven method.’ In the driven method, the clamped end of cantilever was oscillated with a reference signal, and the response of the free end of cantilever was measured. This section explains how the parameters needed for damping

calculation were recorded with a lock-in amplifier. In my research, I have used DSP Lock-in Amplifier (SR830, Stanford Research Systems). The explanation is for this specific equipment, and based on its manual.[52]

The lock-in amplifier is used to detect the signal buried under other noises with higher amplitude. It extracts signal only in a narrow bandwidth around a reference frequency. It extracts signal only at a desired frequency comparing phases from the reference signal. That is a reason lock-in amplifier is called phase-sensitive detector (lower case "psd").

When the lock-in amplifier generates a sinusoidal wave with frequency ω_L with a phase at θ_{ref} relative to the reference signal, this wave ($V_{lock\text{-}in}$) can be expressed as $V_{lock\text{-}in} = V_L \sin(\omega_L t + \theta_{ref})$. If this wave excites the resonator in the experiment, the signal from the experiment has V_{sig}, the amplitude of the measured signal, with the reference frequency ω_r, and the phase relative to reference is θ_{sig}, the wave from experiment, V_{exp} can be expressed as $V_{exp} = V_{sig}\sin(\omega_r t + \theta_{sig})$. Note that $V_{lock\text{-}in}$ has one frequency, but V_{exp} has many different frequencies. The product of these two signal can be used to eliminate the signal at unwanted frequency. The product $V_{psd} = V_{lock\text{-}in} \cdot V_{exp}$ can be written as:

$$\begin{aligned} V_{psd} &= V_{sig}V_L \sin\left(\omega_r t + \theta_{sig}\right)\sin\left(\omega_L t + \theta_{ref}\right) \\ &= \frac{1}{2}V_{sig}V_L \cos\left([\omega_r - \omega_L]t + \theta_{sig} - \theta_{ref}\right) \\ &\quad -\frac{1}{2}V_{sig}V_L \cos\left([\omega_r + \omega_L]t + \theta_{sig} + \theta_{ref}\right). \end{aligned} \tag{10}$$

Processing this signal product with a low pass filter would remove the high frequency component ($\omega_r + \omega_L$) in Eq (**10**), which leaves:

$$V_{psd} = \frac{1}{2} V_{sig} V_L \cos\left([\omega_r - \omega_L]t + \theta_{sig} - \theta_{ref}\right) \quad (11)$$

Unwanted signals can be further eliminated when the frequency of the signal is the same as the amplifier's frequency, $\omega_r = \omega_L$, then it becomes:

$$V_{psd} = \frac{1}{2} V_{sig} V_L \cos\left(\theta_{sig} - \theta_{ref}\right). \quad (12)$$

This is a DC signal proportional to the signal voltage, which provides information of the amplitude of the measurement at the reference frequency. Other signals with frequencies close to the reference frequency, but not $\omega_r = \omega_L$, also survive. When the signal frequency at $\omega_r + \Delta\omega$ is considered, V_{psd} through a low-pass filter becomes weaker as $\Delta\omega$ becomes larger, because it generates higher frequency terms. Therefore the components closer to the reference frequency has stronger signal, having the strongest signal at $\omega_r = \omega_L$. The period at which these signals are averaged can be controlled by changing 'time constant', or simply $1/\Delta\omega$, at the lock-in amplifier which designates the filter frequency.

The phase dependency can also be removed by making the second signal, V_{psd2} by adding 90° to the phase, which gives;

$$V_{psd2} = \frac{1}{2} V_{sig} V_L \sin\left(\theta_{sig} - \theta_{ref}\right). \quad (13)$$

Therefore two output, one proportional to cosine and the other to sine, are generated. The lock-in amplifier calculate the 'in-phase' component $X = V_{sig} \cos\theta$ which is proportional to V_{psd} and 'quadrature' component $Y = V_{sig} \sin\theta$ proportional V_{psd2}. θ is defined as $\theta_{sig} - \theta_{ref}$.

The lock-in outputs two signals: the amplitude, R,

$$R = \sqrt{X^2 + Y^2} = V_{sig}, \tag{14}$$

and the phase difference, θ:

$$\theta = \tan^{-1}\frac{Y}{X}. \tag{15}$$

which I use to calculate the damping in this thesis.

2.3. Pressure Measurement

Paul *et al.*[11] provided a way to relate gas density to the resonance behavior of a bar-like structure. Out of their work presented in Ref. 11 , I derived relation between pressure, resonance frequency, ω_0, and quality factor. The detailed calculation and derivation are also presented in Chapter 3, therefore a brief summary is presented here.

The first task is interpreting the stochastic behavior with the fluctuation-dissipation theorem as described earlier. The thermal motion of a single cantilever was collected for 1 second for 1 MHz frequency. This data was Fourier-transformed and multiplied by its own complex conjugate to generate power spectra density. If considered a simple harmonic oscillator, ω_0 and Q can be fitted.

The next step is to relate these two variables to density. I started from Eq. (29) of ref 3, the simplest equation relating the resonance behavior and density. I made steps to directly relate them by using Eqs. (25) and (41). The final equation for ideal gas which relates P and ω_0, Q is

$$\frac{\alpha\pi w^2 L m_m \omega_0^2}{4k}\frac{P}{RT}\Gamma''\left(\frac{P}{RT}\frac{m_m\omega_0 w^2}{4\eta}\right)=\frac{1}{Q}, \tag{16}$$

where $\alpha = 0.243$, w and L is the width and length of cantilever, m_m is molar mass of surrounding fluid, k is force constant of cantilever, R is the gas constant, T is the temperature of the system, η is dynamic viscosity of surrounding fluid. Γ" is the imaginary part of the function Γ described below:

$$\Gamma(\omega_0) = 1 + \frac{4i\,K_1(-i\sqrt{iR_\omega})}{\sqrt{iR_\omega}\,K_0(-i\sqrt{iR_\omega})}, \tag{17}$$

where K_n is Bessel function of nth kind, while R_ω is defined as below.

$$R_\omega = \frac{\rho\omega_f w^2}{4\eta}. \tag{18}$$

2.4. Damping Measurement

Two different methods were used to calculate damping, which are compatible to each other. Measured damping can be related to slip length using Vinogradova's equation[21] and and the TMAC using Maxwell's equation.[16] One method is measured with thermal deflection with the help of fluctuation dissipation theorem and the other method is 'driven method' based on the work by Ducker and Cook.[53]

2.4.1. Thermal Method

The basic concept of this method is the same as that described in Section 2.3. The thermally –stimulated deflection of cantilever at a certain distance from a planar surface is measured. The power spectra density (PSD) at the separation and fluid condition is generated by

taking Fourier-transform. With the help of fluctuation dissipation theorem, the PSD can be interpreted as if it is from deterministic motion of damped harmonic oscillator as below.

$$m\ddot{z} + m\gamma(h)\dot{z} + kz = f_{therm}(t), \tag{19}$$

where m is the loaded mass (sum of the actual mass of the cantilever and the mass of the fluid), $\gamma(h)$ is damping as a function of separation, h, and $f_{therm}(t)$ is random thermal force acting on the cantilever, considered white noise independent of frequency. z is the deviation of free end of cantilever from equilibrium value of z. Taking Fourier-transform of Eq. (19) yields;

$$m(i\omega)^2 Z + m\gamma(h)(i\omega)Z + kZ = F_{therm}(\omega) \tag{20}$$

where Z and F are frequency-dependent Fourier-transformed function of $z(t)$ and $f_{\text{therm}}(t)$. Substituting m with $m = k/\omega_0^2$, then arranging Eq. (20) in terms of Z, and multiplying Z by the complex conjugate of Z yields:

$$|Z|^2 = \frac{(\omega_0^4/k^2)F^2}{(\omega^2 - \omega_0^2)^2 + \gamma^2\omega^2} \tag{21}$$

The numerator is constant, and thus the frequency dependence of the the amplitude of Z all arises from the denominator. The PSD can be obtained by dividing Eq. (21) by the time period (time to take measurement), also a constant. Therefore, Eq. (21) is a form of PSD. A fit of Eq. (21) is then made to an experimental measurement to obtain ω_0, γ, as a function of the separation for my experiments.

The focus in this thesis is on the damping, D, which can be obtained from:

$$D = \gamma m = \gamma \frac{k}{\omega_0^2} \tag{22}$$

The second expression is more useful in this thesis, because I never explicitly calculate the mass, whereas the spring constant and resonant frequency are easy to determine. By repeating this calculation for each separation, including the one at $h = \infty$ (or more than 1 mm in practice), damping-separation relation can be known to calculate slip length with Eq. (6).

2.4.2. Driven Method

Ref. 53 describes the fast measurement of surface forces when the clamped end of cantilever is driven at a certain frequency, ω. The force balance is:

$$m\ddot{z} + m\gamma(h)\dot{z} + kz = kA\cos(\omega t) + C, \tag{23}$$

where A is the amplitude of oscillation at the clamped end, and C is a constant to account for constant forces. The solution is:

$$z = R(h)\cos(\omega t + \theta(h)) + Z, \tag{24}$$

where $R(h)$ is the amplitude of oscillation at the free end as a function of separation, h, while $\theta(h)$ is phase lag at the free end relative to that of the clamped end. Z is the equilibrium position of z. The damping and stiffness can then be calculated from the *R(h)* and *θ(h)* as follows:

$$\gamma(h) = -\frac{[\omega_0(\infty)]^2}{\omega}\frac{A}{R(h)}\sin\theta(h) \tag{25}$$

$R(h)$ is the amplitude of oscillation at the free end as a function of separation, h, while $\theta(h)$ is phase lag at the free end relative to that of the clamped end. $\omega_0(\infty)$ is the resonance

frequency at infinite separation. The driving frequency ω is always set to $\omega_0(\infty)$. With this fact and, again using $m = k/\omega_0^2$, the damping coefficient can be calculated as:

$$D(h) = m\gamma(h) = -\frac{k}{\omega_0(\infty)}\frac{A}{R(h)}\sin\theta(h) \tag{26}$$

Since A and $\omega_0(\infty)$ are controlled variables, knowledge of $R(h)$, $\theta(h)$, and k allows calculation $D(h)$. k is calculated with Hutter method.[54] $R(h)$ and $\theta(h)$ be obtained from the lock-in amplifier as discussed in Section 2.2.2.

2.4.3. Comparison of Driven and Thermal Methods

For most of this thesis, I used the driven method. This is because it is much faster and also simpler to implement. For a typical measurement of the slip length or TMAC, I needed the damping coefficient as a function of the separation, with at least about 10-15 different separations. For the thermal method, each damping measurement at each separation required the measurement of the thermal (PSD) which took about 3 minutes to capture with sufficient accuracy to obtain a good fit. This not only was time-consuming for me, it also introduced the problem of thermal drift. Thermal drift is the fact that small changes in temperature with time lead to changes in both the separation between the sphere and the plate and the deflection with time. Thus, after each PSD was measured, the sphere had to be driven into the plate so that the final position of the sphere during the PSD could be estimated. This was also time consuming and introduced errors.

In contrast, the driven method was much faster. The time taken to collect $R(h)$ and $\theta(h)$ was only about one tenth of the integration period, which itself was typically about 0.01 s. Thus in 0.01 s, I could obtain 10 values of $R(h)$ and $\theta(h)$ at different points. By experiment,

I found that the drift in separation was about 0.4 nm in 60 s. So I selected 100 s for the time period of a run. In that time, (a) the thermal drift was 0.7 nm, which I considered to be negligible compared to the typical range of separations of 70 to 1800 nm, and (b) I was able to measure 100,000 values of $R(h)$ and $\theta(h)$, each at a different separation. Collecting data from 100,000 separations decreased the error in making the fit of the slip length. Also, because the data points were so closely spaced in distance, I simply ramped the piezoelectric crystal translational stage and measured the signal continuously. Finally, there were considerable advantages in data analysis: (a) for each separation, I needed to record only two values, $R(h)$ and $\theta(h)$ rather than an entire PSD (about 400 kilobytes), and (b) there was no need to do a fit to the spectrum. The only disadvantage was that, by not collecting the full spectrum, I did not actually test that the response was consistent with the harmonic oscillator model at each position. But having checked that for many thermals, I no longer considered it necessary to check further.

Though it is not utilized for my experiments, the driven method can also be used to measure pressure. From Eq. (16), one has to know Q and ω_0, but this time, depending on P. At certain P, ω_0 can be measured by finding the frequency from the function generator at which $R(P)$ is maximum. Q can be related to $D(P) = k/(D\,\omega_0)$, k obtained from Hutter method.[54]

2.5. Determination of Zero Separation

Since the values of D are all dependent on separation between the glass sphere and the plate, accurate measurement of separation is crucial to data interpretation. Thanks to the piezoelectric crystal translational stage, *changes* in the displacement of the plate can be accurately measured

at sub-nanometer level. However, the zero of separation was required for absolute measurement of the separation between the plate and the sphere.

For both thermal and driven method, I decreased the unknown distance between surfaces little by little until the contact was made. Assuming no water film on the sample surfaces, the sign of making contact was characterized by decrease in deflection. When the sphere is in contact with the plate, the vibrations of the cantilever are drastically reduced due to the stiffness and damping of the plate, resulting in significantly less vibration of cantilever. After making contact, the average value of deflection increased linearly with more displacement of the plate.

Additional phenomena confirmed the contact. For the thermal method, the contact was also characterized by no distinct peak near the resonant frequency at large separation (although there were some peaks at low frequency). For the driven method, $R(h)$ value near zero indicated the contact, because the tightly fixed translational stage did not allow the vibration.

Another phenomena which indicated the contact was "jump in" of cantilevers toward the plate. When the attractive force was greater than the force constant of cantilevers (around 0.05 N/m) due to small separation, the mechanical instability made cantilevers jump toward the plate. This phenomenon is shown with the solid black line in Figure 4 of this chapter. This kind of data was not recorded for the thermal method, but was observed and utilized as an evidence of making contact. As shown in Figure 4, the jump distance J_M is different from each humidity level as represented by different lines. The jump distance became larger with high humidity, in other words, thicker water film. I interpreted larger jump distance was a result from capillary after the glass sphere with water film made a contact with the plate with water film. More humidity means thicker water film, thus increasing the jump distance. The water film thickness can be

inferred from this J_M. However for determining zero separation, the position at the dip minus 16 nm was used as zero separation. The calculation based on Lifshitz theory predicted the separation at which the attractive force between two semi-infinite glass plates with various water thickness overcame the nominal force constant (0.05 N/m) was between 13 to 17 nm. To simplify the problem, 16 nm was used.

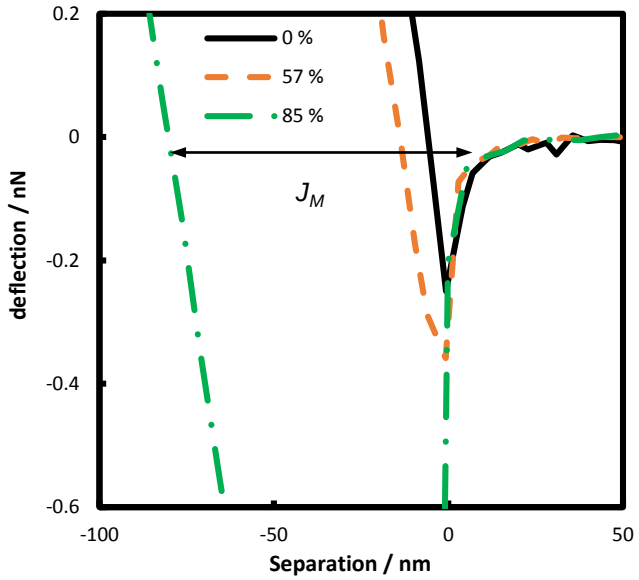

Figure 4 Force curve from deflection data according to humidity

In addition to determining zero separation, I also corrected the separation. With thermal method, the fluctuation was less than 1 nm, which I neglected when fitting the data to the model. However for the driven method, $R(h)$ was about 5 nm, even to 10 nm. With deflection data recorded, moving toward and away from the plate was taken into account in correcting the distance between the sphere and the plate.

Chapter 3. Micron-scale Pressure Gauge

In this chapter, the article published at Review of Scientific Instrument on May 15, 2012 on volume 83, page 055005 in as-published format is presented. The significance of this work is that the pressure of relatively small interior dimensions (under micron scale) can be measured with relatively small error compared to conventional pressure gauges used for macroscopic systems without calibration.

This project is about investigating the possibility of using cantilevers to detect gas motion, and my getting accustomed to measurement with AFM cantilevers.

A pressure gauge based on gas density measurement from analysis of the thermal noise of an atomic force microscope cantilever

Dongjin Seo,[1] Mark R. Paul,[2] and William A. Ducker[1,a)]
[1]*Department of Chemical Engineering, Virginia Tech, Blacksburg, Virginia 24061, USA*
[2]*Department of Mechanical Engineering, Virginia Tech, Blacksburg, Virginia 24061, USA*

(Received 5 March 2012; accepted 28 April 2012; published online 15 May 2012)

We describe a gas-density gauge based on the analysis of the thermally-driven fluctuations of an atomic force microscope (AFM) cantilever. The fluctuations are modeled as a ring-down of a simple harmonic oscillator, which allows fitting of the resonance frequency and damping of the cantilever, which in turn yields the gas density. The pressure is obtained from the density using the known equation of state. In the range 10–220 kPa, the pressure readings from the cantilever gauge deviate by an average of only about 5% from pressure readings on a commercial gauge. The theoretical description we use to determine the pressure from the cantilever motion is based upon the continuum hypothesis, which sets a minimum pressure for our analysis. It is anticipated that the cantilever gauge could be extended to measure lower pressures given a molecular theoretical description. Alternatively, the gauge could be calibrated for use in the non-continuum range. Our measurement technique is similar to previous AFM cantilever measurements, but the analysis produces improved accuracy. [http://dx.doi.org/10.1063/1.4717678]

I. INTRODUCTION

The accurate measurement of pressure is essential in many areas of science and engineering. Many types of pressure gauges are available, using either mechanical or electrical mechanisms to sense the pressure; the preferred method depends on the range of gas pressure. One of the most common methods in the range 0.1–1000 Pa ($10^{-3} \sim 10$ torr) is the Pirahni gauge, which senses the thermal conductivity of the gas. At constant temperature, the thermal conductivity is proportional to the number density of gas molecules so the Pirahni gauge is essentially a gas density sensor.[1] The Pirahni gauge measures the resistance of a wire exposed to the gas, and the resistance decreases at lower temperatures. The wire is heated by an electrical current and cooled by heat transfer into the gas. Heat transfer into the gas is lower at lower pressure, so at lower pressure, the temperature increases and so does the resistance.[2]

Existing commercial gauges provide good performance for large volumes of gas, but there is a need for accurate pressure measurement in small volumes for micro- and nano-sized devices such as microelectromechanical systems.[3] Micron-sized structures, such as microfabricated cantilevers, have been used to study and measure a number of chemical, biological, and physical properties,[4,5] including pressure, P, which has been obtained from the quality factor, Q, and the resonance frequency of driven cantilevers in fluid. For example, Bianco *et al.*[6] examined driven microfabricated cantilevers, then related the quality factor and the resonance frequency to pressure using theories from Christian,[7] Bao *et al.*,[8] and Hosaka *et al.*[9] Bianco *et al.* showed that the quality factor is inversely proportional to pressure in the molecular region, and inversely proportional to the square root of pressure in the continuum region. Ekinci *et al.*[10] examined driven doubly clamped micron beams (micron bridges) and cantilevers. They also reported that the quality factor was inversely proportional to the square root of P in the continuum region and inversely proportional to P in the molecular region. Other researchers[11,12] determined the pressure using the theory by Christian[7] and Hosaka *et al.*[9] They also reported that their results were in good agreement with the theories, concluding that $Q \sim 1/P^{1/2}$ in the continuum regime and $Q \sim 1/P$ in the molecular regime.

Instead of relating pressure to the quality factor and resonant frequency using theory, Mortet *et al.*[13] calibrated a specific piezoelectric bimorph microcantilever by measuring the resonant frequency change as a function of pressure and temperature, i.e., pressure was determined empirically.

To be practical, a gauge should be able to measure the pressure over some defined range with a specified error, and preferably the pressure should be predicted from Q and the resonance frequency using theory. At this point there are several good measurements and theories, but what is lacking is an AFM cantilever pressure gauge that has a specified agreement with theory over a useful and specified range of pressures. In this paper, we describe a method that is based on the theory of Paul and Cross[14] that can be used to measure the gas pressure in the range 10–225 kPa with an error that is 5% on average.

II. THEORY

There have been many analytical investigations of the dynamics of small objects such as cylinders and cantilevers immersed in a viscous fluid.[15–19] Of particular relevance to our approach is the work of Sader,[19] which provided a detailed analytical description of the dynamics of oscillating cantilevers immersed in a viscous fluid for the case of long

a)Author to whom correspondence should be addressed. Electronic mail: wducker@vt.edu.

and thin cantilevers where the cantilever length is much larger than its width. Paul and Cross[14] then developed a theoretical description of the stochastic behavior of a cantilever immersed in a viscous fluid that is driven by Brownian motion. We have used this theoretical description in our analysis here. In the following, we present only the essential details of the theoretical background (for more details see Ref. 20). The frequency dependence of the Brownian force is included via the fluctuation-dissipation theorem which states that the thermal fluctuations of a system at equilibrium are directly related to the dissipation in the system. Using linear response theory it has been shown that the deterministic response of the cantilever to a small perturbation away from equilibrium can be used to find the stochastic dynamics. Using deterministic numerical simulations for the cantilever ring-down allows one to quantify the stochastic dynamics of the cantilever for the precise conditions of experiment. In the limit of long and slender cantilevers, as is the case in our experimental measurements presented here, it is possible to develop an analytical description of the stochastic cantilever dynamics. Specifically, the auto-correlation of equilibrium fluctuations of the cantilever displacement can be found from the deterministic ring down of the cantilever to the removal of step force. This can be represented as

$$\langle x(0)x(t)\rangle = \frac{k_B T}{F} X(t), \tag{1}$$

where x is the stochastic deflection of the cantilever tip, t is the time, k_B is the Boltzmann constant, T is the absolute temperature, F is the magnitude of force applied to the cantilever tip at some time in the distant past that is removed at time zero, $\langle\ \rangle$ denotes an equilibrium ensemble average, and $X(t)$ denotes the deterministic displacement of the cantilever tip due to the removal of the force. Equation (1) relates an easily measurable quantity, the autocorrelation of the thermal motion, to a deterministic and more easily modeled quantity, the displacement of a cantilever.

If the deterministic ring-down of the cantilever is modeled as a simple harmonic oscillator as with Paul *et al.*,[20] the time-dependent displacement of the cantilever is given by

$$X(t) = \frac{F}{k} e^{-\omega_f t/2Q}\left(\cos(\omega' t) + \frac{\omega_f}{2Q\omega'} sin(\omega' t)\right), \tag{2}$$

where

$$\omega' = \omega_f \sqrt{1 - \frac{1}{4Q^2}}, \tag{3}$$

where k is the equivalent spring constant of the cantilever and ω_f is the resonant frequency of the cantilever when immersed in fluid which we determine as the frequency at the maximum amplitude of power spectral density. The quality factor can then be related to the mass density of the fluid, ρ, by combining Eqs. (25), (29), and (41) in Paul *et al.*[20] to yield

$$\frac{\alpha\pi w^2 L\omega_f^2}{4k}\Gamma''(R_\omega) = \frac{1}{Q}, \tag{4}$$

where w is the width of the cantilever, L is the cantilever length, $\alpha = 0.243$ is a parameter accounting for our representation of the cantilever as a lumped mass, and R_ω is the nondimensional frequency parameter.

$$R_\omega = \frac{\rho\omega_f w^2}{4\eta}, \tag{5}$$

where η is the dynamic viscosity of the surrounding fluid which depends on temperature but not on pressure in general. Γ'' is the imaginary part of the complex hydrodynamic function,

$$\Gamma(\omega_f) = 1 + \frac{4iK_1(-i\sqrt{iR_\omega})}{\sqrt{iR_\omega}K_0(-i\sqrt{iR_\omega})}, \tag{6}$$

where K_1 and K_0 are Bessel functions.

Equation (4) can be used to obtain either the density or the viscosity from the quality factor and the resonant frequency. Here, we use the known viscosity (which is almost independent of pressure, but depends on temperature) to obtain the gas density. Pressure can be calculated from the density with an appropriate equation of state. At the pressures considered in this paper, the compressibility of air and nitrogen is very close to one so they obey the ideal gas equation, $P = (\rho/m_m)RT$, where m_m is the molar mass of the gas, and R is the gas constant. Substitution of the ideal gas equation into Eq. (4) yields

$$\frac{\alpha\pi w^2 L m_m \omega_f^2}{4k}\frac{P}{RT}\Gamma''\left(\frac{P}{RT}\frac{m_m\omega_f w^2}{4\eta}\right) = \frac{1}{Q}, \tag{7}$$

which we use here to obtain the pressure from the quality factor.

III. EXPERIMENTS

AFM cantilevers were purchased from Bruker Corporation (Model No. OCR8-W).[21] Two nominally identical cantilevers (B and C) and one different cantilever (A) were used (see Table I). The unclamped end of the cantilevers is tapered. The spring constants, k, were measured from the thermally stimulated changes in endslope (the Hutter method)[22] using the light-lever technique in an Asylum instruments MFP-3D, then the length and width were measured using an optical microscope. Equations (4) and (7) do not require knowledge of the cantilever thickness.

The resonance properties of each cantilever were measured in a cylindrical glass jar with a screw-top lid. The endslope of the cantilever was measured with a homebuilt light lever sensor consisting of a laser (681 nm, Schäfter + Kirchhoff GmbH) and a split photodiode (Phresh Photonics) connected via an A/D card (PCI-6110, National Instruments) to a computer. Temperature was recorded with a thermometer (TH-3, AMPROBE).

TABLE I. Measured spring constants and dimensions of cantilevers.

Designation	A	B	C
k, pN/nm	102	46	42
Length, μm	202	202	198
Width, μm	37	18	18

The pressure was reduced below atmospheric pressure with a vacuum pump, and increased with pure dry nitrogen. The pressure inside the glass jar was measured with a DPG25V gauge (SUPCO) for $P > 7$ kPa with a manufacturer's stated error of $\pm 0.5\%$ of the reading, and Digivac 276 (Digivac Co.) for $P < 7$ kPa with varying errors listed on their product information page.[23] Digivac 276 senses the electric properties of a thermocouple with varying pressure, while DPG25V is a differential gauge. In our implementation, various commercial pressure gauges did not agree with each other (within the stated error) so the actual errors in gas measurement in our implementation were greater than under the manufacturer's conditions. This was particularly a problem for 1.5 kPa $> P >$ 12 kPa. We limit our conclusions to pressures greater than 10 kPa because of uncertainty in the known pressure for comparison to our measurement from the cantilever-gauge.

After the desired pressures were reached, a time series of the cantilever deflection was collected for 15 s (cantilevers A and B) or 5 s (cantilever C) with 1 μs intervals between periods of data collection. For cantilevers A and B, the 15 million data points were divided into 500 sequential windows of 30 000 data points. The data in each window was detrended by subtraction of the best linear fit and was then processed using a fast Fourier transform. The transformed data was multiplied by its complex conjugate to provide the power spectral density for one window. The average power spectral density was computed by averaging the spectrum from all 500 windows. The auto-correlation of the equilibrium fluctuations was then determined by computing the inverse fast Fourier transform of the averaged power spectral density. For cantilever C, 5 million data points were divided into 500 sequential windows of 10 000 data points.

Our deflection measurements were in arbitrary units, which we then normalized such that the auto-correlation at zero time lag was unity. This is equivalent to setting the area under the power spectral density to $k_B T/k$ as was done to calibrate the spring constant. As shown in Eq. (1) the auto-correlation of the equilibrium fluctuations are directly related to the deterministic ring-down of a simple harmonic oscillator which is given by Eq. (2). We obtained values for Q and ω_f by fitting our experimental results with Eq. (2). The cantilever-gauge pressure is the gas pressure calculated using Eq. (7). The analytical theory we are using is for a cantilever with a constant value of the width for the entire length of the cantilever. However, the cantilevers used in the experiments had a slight taper in width near the unclamped end, so there is no unique width. Since our cantilevers had no unique width we measured an "effective width" at atmospheric pressure (where the pressure was known) and we have used this constant width for all the data sets to calculate pressures with Eq. (7). For example, the effective width of the cantilever B was 14 μm, rather than the nominal width of the cantilevers, 18 μm. The significant discrepancy between the fitted width and the measured nominal width suggests that this parameter may also be accounting for effects other than the width of the cantilevers. Note that the molar mass of the gas can be included in this effective width, if unknown.

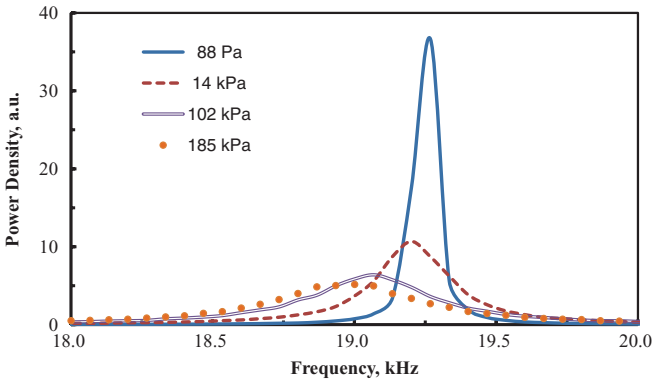

FIG. 1. Power spectral density for cantilever B at 4 different pressures. At higher pressure, the fundamental resonance shifted to lower frequency and the width of the peak was broader.

IV. RESULTS

For cantilever A, 28 data sets were obtained for the power spectral density and auto-correlation. The first set was measured at the atmospheric pressure of the day, recorded as 102 kPa, which was used to calculate the effective width of the cantilever. For cantilever B, 19 data sets were collected along with the data set at atmospheric pressure. For cantilever C, 37 data sets were measured. Combining the experiments from all three cantilevers the pressure varies from 33 Pa to 225 kPa. The temperature in the lab varied between 292 K and 297 K. Examples of the power spectral density are shown in Figure 1 for a variety of gas pressures. The spectra in Figure 1 (and other spectra not shown here) were in accordance with the qualitative expectation that an increase in pressure led to both a shift to lower resonance frequency and a broadening of the resonance peak (lower Q).

The pressure from Eq. (7), using the fitted values of Q and ω_f, is shown as a function of the pressure measured by the commercial gauge in Figure 2. Figure 2(a) shows the comparison over all pressures for all three cantilevers on a log scale, whereas Figure 2(b) shows a subset of data where the pressure exceeds 10 kPa, on a linear scale.

Clearly the pressure obtained from the cantilever agrees well with the pressure from the differential gauge in the range 10–225 kPa. The percentage deviation between the two measured pressures is shown in Figure 3; on average there is only a 5% deviation between the two gauges.

Figure 2(a) shows the pressure predicted by Eq. (7) systematically deviates from the thermocouple gauge, Digivac 276, at pressures below 10 kPa for cantilevers B and C. This is expected because we have used a continuum theory of the gas. The transition between continuum and molecular behavior is characterized by the Knudsen number, Kn = mean free path/characteristic length. In this case, the characteristic length is the effective width of the cantilevers $\approx$14 μm for cantilever B and C. Typically, the continuum regime applies to Kn < 0.1.[6,24] For air, 10 kPa is equivalent to Kn $\approx$0.07, so the deviation occurs approximately at the expected pressure. Cantilever A is wider, with an effective width of 35 μm, and therefore the pressure is lower before the mean free path reaches one tenth of the cantilever width (Kn = 0.1). This is consistent with observation: Figure 2(a) shows that pressure

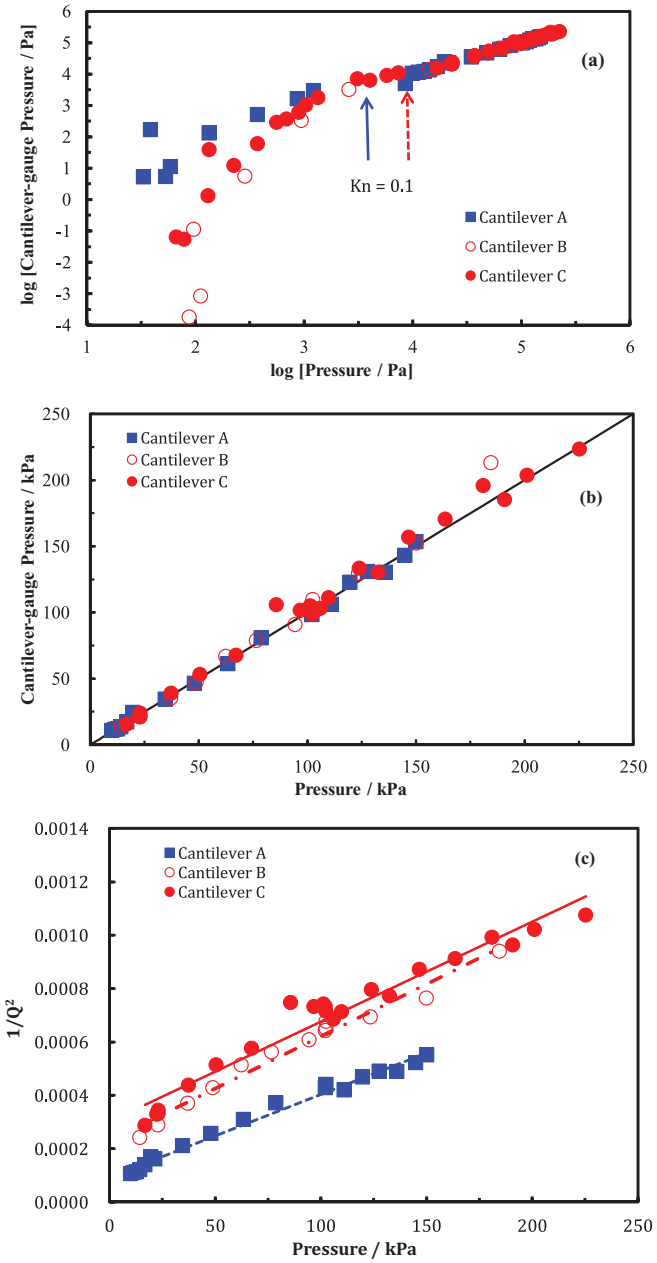

FIG. 2. Cantilever-gauge pressure as a function of the measured pressure. Cantilever-gauge pressure is the pressure calculated with Eq. (7). (a) All data is shown using a log scale. The arrows point to the pressure where Kn = 0.1 (solid blue for cantilever A, dashed red for B and C), and thus to the approximate limit of applicability of equations assuming continuum behavior. (b) $P > 10$ kPa on a linear scale. The solid black line shows equal pressure on the commercial and cantilever gauges. (c) Comparison of our experiments with the trend $Q \sim 1/P^{1/2}$ as suggested in the literature.[6,9–12] The dashed blue line is the linear trend for cantilever A, the red dash-dot line is the linear trend for cantilever B, and the solid red line is for cantilever C.

measurements from the wider cantilever A using Eq. (7) have better agreement with the commercial gauge at lower pressure than the narrower B and C cantilevers.

For comparison to previous work (see Sec. I), we have also examined how well our data agrees with the relation, $P \propto 1/Q^2$. Figure 2(c) shows the fitted values of $1/Q^2$ plotted as a function of measured differential gauge pressure for data in the range 10–225 kPa along with a best fit line for each cantilever. The mean deviation of the points from the line is 15%, which is worse than the deviation of 5% using the analysis from Paul *et al.* (see Sec. II) but still useful for more approximate work. Note that simply using $P \propto 1/Q^2$ to determine pressure also requires fitting a line to data points at several pressures (i.e., a calibration set), whereas our method requires only calibration of an effective width at atmospheric pressure. Also, the errors in our method (see Fig. 3) are roughly distributed about zero whereas the $1/Q^2$ method shows a trend to lower $1/Q^2$ at higher pressure and higher $1/Q^2$ at lower pressure.

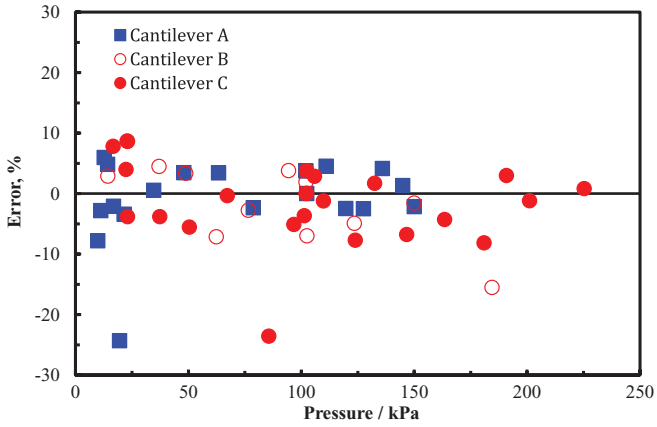

FIG. 3. Percentage error of cantilever-gauge pressure from the commercial-gauge pressure in the range 10–225 kPa. The error is calculated as 1-(cantilever-gauge pressure/commercial-gauge pressure). Except for three data points, the errors are within 10%. The mean error is 5%.

V. DISCUSSION: EFFECT OF TEMPERATURE AND HUMIDITY

Equation (7) explicitly depends on the temperature, but the main effect of temperature is through the effect on the viscosity. In the analysis described here, we measured the temperature, and used the measured temperature in Eq. (7), but it is interesting to also examine the sensitivity of the pressure calculated from Eq. (7) to changes in temperature, for use of the gauge without a thermometer. For a measurement at 19 °C, an input of 18 °C in Eq. (7), yields a pressure that is 1% greater; an input of 25 °C, yields a pressure that is 2% lower. Thus, the use of an approximate guess of the temperature results in only small errors in the measured pressure.

Humid environments can potentially affect the operation and interpretation of the gauge in two ways; by forming a wetting film on the cantilever and by affecting the gas properties. Cantilevers typically have a finite water contact angle, so adsorbed water films will be thin, even compared to the thickness of the cantilever (< 1 μm). The combination of a very hydrophilic (clean) cantilever and variable humidity above 80% at high pressure (~1 atm) should be avoided so as to avoid errors due to changing mass of the cantilever after calibration. Humidity also affects the density and viscosity of the gas, but these effects can be included explicitly through the use of tabulated data for the density and viscosity of humid air (e.g., in Ref. 25). The effects of an unknown humidity on the measurement can be estimated from tabulated data. At 1 atm and room temperature, the partial pressure of saturated

water vapor is only about 2% of the total pressure, and thus neglect of a humidity change from 0%–100% only affects the measured density and viscosity by about 1% and 2%, respectively, which would cause a 6% error in the measured pressure if ignored. The partial pressure of water vapor increases with temperature, so the effect of humidity on viscosity and density should not be ignored nearer to the boiling point of water. So, in summary, the effects of both humidity and temperature are simply included if the humidity and temperature are measured. If they are not, this neglect causes only a minor effect on the measured pressure, except at high temperature, and possibly for a cantilever that is completely wet by water.

VI. CONCLUSION AND OUTLOOK

The pressure of gases near one atmosphere was obtained from measurements of the auto-correlation of equilibrium fluctuations in AFM cantilever displacement. In the pressure range 10–225 kPa, the cantilever pressure gauge deviated by an average of 5% from values measured by a commercial differential gauge. At lower pressure, where the Knudsen number is greater than 0.1 and the theory is not expected to be valid, our pressure measurements were systematically lower than those from other gauges. The deviation of the cantilever gauge at low pressure was smaller when a wider cantilever was used (i.e., there was a lower Knudsen number at a given pressure). The quality factor and resonant frequency are still functions of pressure below 10 kPa, so the range of the pressure gauge could be extended to lower pressures using either a calibration curve (e.g., Figure 2(a)) or a theoretical description applicable at lower pressures.

The largest dimension of the cantilever is 200 μm, so the detector takes up a very small space in the gas. This device should be useful in microscale applications such as lab-on-a-chip and microflow applications. It may also find application in aeronautical applications where many sensors could be added in close proximity with little weight gain or interference with the flow. The sensor can be used to measure pressures above and below atmospheric pressure.

ACKNOWLEDGMENTS

The work described in this paper was funded by the National Science Foundation via Award No. CBET-0959228 and by Virginia Tech. The authors acknowledge useful discussions with John Walz, Brian Robbins, and Milad Radiom.

[1] A. Ellett and R. M. Zabel, Phys. Rev. **37**, 1102 (1931).
[2] J. F. O'Hanlon, *A User's Guide to Vacuum Technology*, 3rd ed. (Wiley, Hoboken, 2003), p. 89.
[3] W. P. Eaton and J. H. Smith, Smart Mater. Struct. **6**, 530 (1997).
[4] F. G. Barth, J. A. C. Humphrey, and T. W. Secom, *Sensors and Sensing in Biology and Engineering* (Springer-Verlag, New York, 2003), pp. 338–341.
[5] A. Raman, J. Melcher, and R. Tung, Nanotoday **3**, 20 (2008).
[6] S. Bianco, M. Cocuzza, S. Ferrero, E. Giuri, G. Piacenza, C. F. Pirri, A. Ricci, L. Scaltrito, D. Bich, A. Merialdo, P. Schina, and R. Correale, J. Vac. Sci. Technol. **24**, 1803 (2006).
[7] R. G. Christian, Vacuum **16**, 175 (1966).
[8] M. Bao, H. Yang, H. Yin, and Y. Sun, J. Micromech. Microeng. **12**, 341 (2002).
[9] H. Hosaka, K. Itao, and S. Kuroda, Sens. Actuators, A **49**, 87 (1995).
[10] K. L. Ekinci, V. Yakhot, S. Rajauria, C. Colosqui, and D. M. Karabacak, Lab Chip **10**, 3013 (2010).
[11] J. Lübbe, H. Schnieder, and M. Reichling, e-J. Surf. Sci. Nanotech. **9**, 30 (2011).
[12] G. Keskar, B Elliott, J Gaillard, M. J. Skove, and A. M. Rao, Sens Actuators, A **147**, 203 (2008).
[13] V. Mortet, R. Petersen, K. Haenen, and M. D'Olieslaeger, Appl. Phys. Lett. **88**, 133511 (2006).
[14] M. R. Paul and M. C. Cross, Phys. Rev. Lett. **92**, 235501 (2004).
[15] H.-J. Butt and M. Jaschke, Nanotechnology **6**, 1 (1995).
[16] E. O. Tuck, J. Eng. Math. **3**, 29 (1969).
[17] L. Rosenhead, *Laminar Boundary Layers* (Oxford University Press, Oxford, 1963).
[18] R. J. Clarke, O. E. Jensen, J. Billingham, A. P. Pearson, and P. M. Williams, Phys. Rev. Lett. **96**, 050801 (2006).
[19] J. E. Sader, J. Appl. Phys. **84**, 1 (1998).
[20] M. R. Paul, M. T. Clark, and M. C. Cross, Nanotechnology **17**, 4502 (2006).
[21] See http://www.brukerafmprobes.com/Product.aspx?ProductID=3378 for more information about the cantilevers.
[22] J. L. Hutter and J. Bechhoefer, Rev. Sci. Instrum. **64**, 1868 (1993).
[23] See http://www.digivac.com/get-educated/digivac-accuracy.html for more information about Digivac 276.
[24] S. Kakaç, L. L. Vasiliev, Y. Bayazitoglu, and Y. Yener, *Microscale Heat Transfer: Fundamentals and Applications* (Springer, Norwell, 2004), p. 3.
[25] P. T. Tsilingiris, Energy Convers. Manage **49**, 1098 (2008).

Chapter 4. Effect of Humidity on Slip Boundary Condition

In this chapter, the article published at Journal of Physical Review C on March 1, 2013 on volume 117, pages 6235−6244 in as-published format is presented. In this chapter and the next, I investigated the parameters which would affect TMAC. In here, I studied effect of surface coatings and water film on them as formed from humidity. Humidity is everywhere and its effect is not known or considered much. There are many reports mentioned in Section 1.3 which measures TMAC but not reporting humidity values. I wanted to find out if it is because it is not affecting TMAC or not important.

For the sake of Chapter 6 and Chapter 7, the variable in this and the next chapter is not something that can be changed easily. Rather, they are determined when systems are set.

THE JOURNAL OF PHYSICAL CHEMISTRY C

Article

pubs.acs.org/JPCC

Gas Flows near Solids Coated with Thin Water Films

Dongjin Seo, Dean Mastropietro, and William A. Ducker*

Department of Chemical Engineering, Virginia Tech, Blacksburg, Virginia 24061, United States

ABSTRACT: We determined the tangential momentum accommodation coefficient (TMAC) of nitrogen gas at glass surfaces that were coated in thin water films produced by controlling the humidity. The accommodation coefficients were determined by measuring the damping of a spherical particle which was separated from a flat plate by a distance of 10 nm to 10 μm. We examined two solids: hydrophilic glass terminated in hydroxyl groups and hydrophobic glass terminated in methyl groups. At the same relative humidity, thicker films of water form on the hydroxyl-terminated films than on the methyl-terminated films, consistent with formation of hydrogen bonds on the hydroxyl-terminated solid and not on the methyl-terminated solid. The TMACs are surprisingly interesting functions of the humidity. For the hydroxyl-terminated silica, the TMAC is 0.5 at 0% relative humidity and increases almost to 1 when the humidity increases to a few percent. The TMAC decreases to 0.25 at around 87% humidity before rising to 0.9 at 100% humidity. We rationalize the increase in TMAC at low humidity in terms of interactions with a very thin layer of water with significant lateral mobility and vibrational and rotational modes to receive momentum; the increase near saturation is explained by nitrogen interacting with near-bulk water. The minimum at intermediate humidity is totally unexpected. The TMAC on methyl-terminated silica follows roughly the same trend, but with more variability between samples.

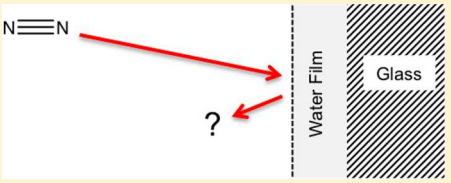

INTRODUCTION

Narrow channels of gas between solids are encountered in engineering systems utilizing small particles, such as catalytic converters, fluidized beds, and cyclone separations[1] as well as lab-on-a-chip systems, microelectromechanical systems (MEMS), and nanoelectromechanical systems (NEMS).[2] The details of gas−solid interactions become important for understanding gas flows when at least one dimension of the flow, l, approaches the mean free path, λ, that is, for large Knudsen numbers (Kn = λ/l). For large Knudsen numbers, the gas-flow boundary condition depends on the degree of momentum conservation during collisions with the solid, and thus on the chemistry and topography of the solid.[2]

Our interest is in processes and devices that operate in ambient air, subject to various levels of humidity, which cause the formation of water films on the solids. The purpose of this paper is to understand the effect of humidity on gas flows near solids, and in particular, N_2 gas flows between two glass solids that are separated by micro- to nanometer dimensions in humid air at one atmosphere of pressure. The introduction of water vapor causes a small change in viscosity of air, which will be ignored here. For example, the viscosity of air falls from 18.176 to 18.134 μPa·s when the humidity is increased from 0 to 93% at 20 °C.[3] The more important effect of humidity is the formation of thin water films on the solids in equilibrium with humid air[4,5] (see Figure 1).

The mean free path of air at one atmosphere of pressure is about 70 nm at room temperature. Thus for channels of dimension 700 nm to 70 μm, the Knudsen number is in the range 0.1−0.001, which corresponds to the slip flow regime. Dimensions down to 7 nm correspond to the transition regime. Maxwell described the slip length, b, in terms of the tangential momentum accommodation coefficient (TMAC), σ,[6]

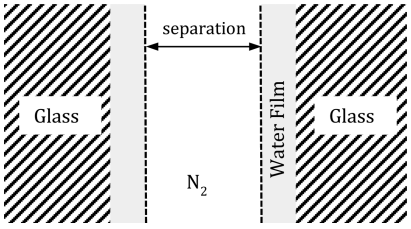

Figure 1. Schematic showing thin water films on the glass walls of a microchannel.

$$b = \lambda\left[\frac{2}{\sigma} - \sigma\right] \quad (1)$$

Since that time, more sophisticated relationships have been developed between b and σ (e.g., refs 2 and 7) but in general our error in resolving b does not justify their usage at this point. The TMAC summarizes the degree to which tangential momentum of gas molecules is conserved during collision with the solid. When the momentum of molecules is conserved (specular reflection) $\sigma = 0$; when the tangential momentum is randomized by collision with the solid (diffuse reflection) $\sigma = 1$. Therefore, the maximum slip length is $b = \infty$ when $\sigma = 0$, and the minimum slip length is the mean free path when $\sigma = 1$. The values of the TMAC depend on the topography and chemistry of the solid. Local variation in the surface normal (roughness) leads to a distribution of changes in tangential momentum during collisions and therefore to increased TMAC. Molecular beam[8,9] and other studies[10] have shown that gas molecules can

Received: December 20, 2012
Revised: February 26, 2013
Published: March 1, 2013

also lose momentum in inelastic collisions with soft surfaces and therefore transfer different amounts of momentum to the solid depending on the stiffness and mass of the atoms with which they collide. This should also increase the TMAC. Thus, the insertion of a liquid layer between the gas and the solid (Figure 1) is expected to have a large effect on the TMAC and the measured flow. Our naïve expectation at the beginning of this work was that insertion of a water film would lead to an increase in accommodation (greater lubrication force) because some fraction of the N_2 gas molecules would penetrate into the water film and be re-emitted with randomized momentum. The results show that the situation is more complex.

In this work, we probe flow using atomic force microscope (AFM) measurements where a flat plate is driven normally toward a spherical particle. We measure the damping coefficient on the sphere, D, and to this fit a theoretical damping using the slip length as a fitting parameter. Vinogradova[11] derived the force in a squeeze film, which is simply the velocity, v, multiplied by D_{lub}. This is a modification of Brenner's no-slip result[12] for the same geometry:

$$D_{lub} = \frac{6\pi\eta r^2}{s} f^* \tag{2}$$

$$f^* = -\frac{2\alpha s}{\beta\gamma} - \frac{2s}{\gamma-\beta}\left[\frac{(\beta+s)(\beta-\alpha)}{\beta^2}\ln\left(1+\frac{\beta}{s}\right) - \frac{(\gamma+s)(\gamma-\alpha)}{\gamma^2}\ln\left(1+\frac{\gamma}{s}\right)\right] \tag{3}$$

$$\alpha = b_1 + b_2, \quad \beta = 2b_1(2+q+\sqrt{1+q+q^2}), \quad \gamma = 2b_1(2+q-\sqrt{1+q+q^2}), \quad q = \frac{b_2}{b_1} - 1 \tag{4}$$

where r is the radius of the sphere, s is the separation, η is dynamic viscosity of fluid, and b_1 and b_2 are the slip lengths of the two solids. We measure the damping as a function of separation, $D(s)$, but our interest is in the lubrication force, so we subtract the damping at infinite separation $D(\infty)$: $D_{lub} = D(s) - D(\infty)$. Thus, the slip-lengths are obtained by fitting to the measured damping to eqs 2−4. In the current work, we use two very similar solids, so there is only one slip length and one fitting parameter.

Prior experimental work on lubrication forces in gas using AFM includes that of Ducker and Cook who measured the damping from the phase and amplitude of response when an AFM tip was driven near a plate.[13] Maali and Bhushan[14] attached a glass sphere to the free end of the cantilever, and measured a slip length of 118 nm for glass in air. A previous study in our lab by Honig et al.[15] analyzed the thermal motion of an undriven cantilever to determine the damping. They showed that the lubrication force depended on the nature of the surface coating. They report the slip length of a clean glass surface was 630 ± 90 nm when exposed to normal room humidity (50−70%), while that of methylated surface was 270 ± 90 nm.[15] This was the first lubrication measurement in gas to show an effect of surface coating. A later study by Bowles and Ducker[16] showed that molecularly smooth mica had a very high slip length.

Laurent et al.[17] examined the slip length of gold surfaces surrounded by a gas (air or helium) by attaching a gold-coated sphere at the free end of a AFM cantilever. They reported a large increase in the fitted slip length at low pressure, which is consistent with eq 1, but at very low pressures, the Knudsen number is no longer in the slip-flow regime so the slip length was simply a fitting parameter. Lissandrello et al.[18] also studied lubrication flows using AFM. They examined the damping over a large range of low pressures, and developed a scaling function to describe damping in terms of mean free path, radius, separation and the viscous boundary layer thickness.

Meanwhile, a parallel effort to understand lubrication in thin films of *liquids* between solids shows much less interesting behavior. Most solid−liquid interfaces obey the no-slip boundary conditions,[19−21] but there are some that exhibit small slip lengths (up to 20 nm)[22,23] when there is a weak interaction between the solid and the liquid. The principal difference is that the mean free path in a liquid is very small, so the effect of collision with the solid is lost over a very short distance.

THEORY OF MEASUREMENT

Two different methods were used to measure the damping, analysis of thermally stimulated vibrations,[24] and analysis of mechanically driven oscillations.[13] The two methods were previously shown to produce similar results.[18]

Thermal Vibrations. An AFM cantilever undergoes vibrations of deflection with an average amplitude that depends on the temperature and a spread of frequencies that depends on the damping. The power spectral density (PSD) of these vibrations is the product of the Fourier-transform of thermal displacement fluctuations and its complex conjugate. We interpret this PSD in terms of a simple harmonic oscillator. Thus:

$$\mathrm{PSD}(\omega) = \frac{B}{(\omega^2-\omega_0^2)^2 + \omega^2\omega_0^2/Q^2} \tag{5}$$

where B is the amplitude of the PSD, ω is frequency, ω_0 is the resonant frequency, and Q is the quality. The damping is obtained from quality as follows:

$$D(s) = \frac{k}{Q(s)\omega_0(s)} \tag{6}$$

where k is the spring constant, which we model here as independent of s or expected water film thickness. More detail can be found in the paper by Seo et al.[25]

Mechanical Driving. In this method, the clamped end of the cantilever is driven (AC drive) at a fixed frequency, $\omega/2\pi$, and amplitude, A, which causes the free end to oscillate with an amplitude, R, and relative phase, θ. The clamped end is also driven toward the plate at a fixed velocity (DC drive) so that the damping can be determined at various separations. The DC drive is sufficiently slow that we ignored the DC motion for analysis of the AC motion, except insofar as the position of the sphere affects the forces acting on it. Again the cantilever motion is analyzed as a simple harmonic oscillator where equation of motion is:

$$m\ddot{z} + m\gamma(s)\dot{z} + kz = kA\cos(\omega t) + C \tag{7}$$

with solution:

$$z = R\cos(\omega t + \theta) \tag{8}$$

$$R(s) = \frac{kA}{m}\left[\omega^2\gamma(s)^2 + \left(\frac{k}{m} - \omega^2\right)^2\right]^{-1/2} \tag{9}$$

dx.doi.org/10.1021/jp312568y | J. Phys. Chem. C 2013, 117, 6235−6244

$$\theta(s) = \tan^{-1}\left(\frac{\omega\gamma(s)}{k/m - \omega^2}\right) \quad (10)$$

where m is the effective mass of the cantilever, z is the cantilever deflection, γ is the damping coefficient, and C is a constant to account for constant forces. In the experiments where water layers form on the cantilever and sphere, m depends on the humidity, and needs to be calibrated at each level of humidity. m is calibrated by measuring the resonant frequency, $\omega_0 = (k/m)^{1/2}$, assuming that the water layers do not affect the cantilever stiffness. In our experiments, the cantilever was always driven at the frequency of maximum amplitude, which is very close to ω_0 for high quality, Q, cantilevers, in air, as is the case here. The frequency of maximum amplitude was determined at each humidity to account for changes in m from adsorbed water. From eqs 9 and 10, at the resonant frequency, the damping coefficient, D is given by:

$$D(s) = m\gamma(s) = -\frac{k}{\omega_0(\infty)}\frac{A}{R(s)}\sin\theta(s) \quad (11)$$

Note that the paper by Ducker and Cook[13] omits (in error) the negative sign in eq 11. R and θ were measured with a lock-in amplifier in which the phase of the response was set to $-\pi/2$ at $s = \infty$ at the amplitude maximum. In this research, the typical value for R at $s = \infty$ was about 2 nm. R decreased at smaller separations.

In general, the stiffness is the sum of the spring constant and the gradient of surface forces, but in the current work, the measurements are at sufficiently large separations that van der Waals forces and other forces are negligible. The probe and plate were irradiated with alpha particles to reduce static charge so that electrostatic forces were negligible. Thus k is simply the spring constant, which was determined by the Hutter method at large separation[26] and was in the range 0.042−0.055 N·m^{-1}.

Determination of Separation. This separation is one of key parameters in calculating slip length because an error in separation propagates into approximately the same magnitude of error in slip length. The separations of interest are quite large, so errors due to the surface roughness are small. We define the separation as the distance between the water films (see Figure 1) and the critical uncertainty in these measurements is in determining the separation between the water films. Since we have no method for measuring changes in thickness of the water films during the measurement, we assume that they have constant thickness during approach at any given humidity. That is, we assume that the deformation of the water films due to surface forces and lubrication forces is zero.

The zero of separation between the solids is relatively easy to establish, and we follow the standard procedure of setting the separation to zero when the deflection is linear with drive distance.[27] For the time immediately before this region, we observe that there is a mechanical instability ("jump"). We interpret the beginning of this instability to be when the surface forces gradient exceeds the spring constant. The unstable region continues when the two water films touch, a bridging capillary is formed, and the sphere again reaches mechanical equilibrium when it rests against the plate (see Figure 2). With this model, the zero of separation between the water films (used in our data figures) is the separation at the start of the measured jump, minus J_v, where J_v is the calculated separation at which the instability should occur from van der Waals forces. Likewise the thickness of each water film is given by:

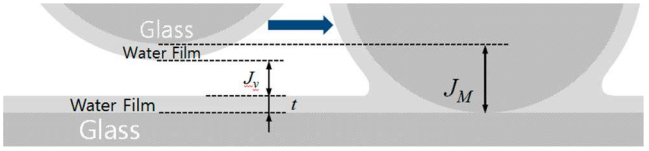

Figure 2. Schematic of capillary formation. We measure a "jump" (range of mechanical instability), J_M. We interpret that jump as initiating with a van der Waals force and finishing with contact between the glass sphere and plate, after the sphere has passed through the water capillary. Thus $J_M = J_v + 2t$.

$$t = (J_M - J_v)/2 \quad (12)$$

where J_M is the experimentally measured jump distance.

J_v was calculated using Lifshitz theory. Good agreement between Lifshitz theory and experiment has been found previously for glass−water systems.[28] Figure 3 shows Lifshitz calculations for the configuration from Figure 1 with different water film thickness, t. The instability begins where the force gradient equals the spring constant. Figure 3 shows that J_v varies in the range 14−17 nm when the film thickness varies between zero and infinity. The small range means that we can know J_v to within a couple of nanometers without knowledge of the water film thickness. Also, the correction is small compared to the measured separations and fitted slip lengths. In practice, we set J_v = 16 nm for all film thicknesses.

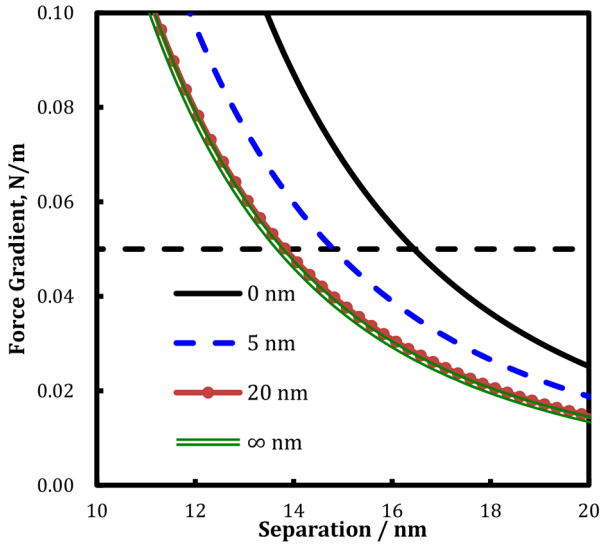

Figure 3. Force gradient for the glass−water−air−water−glass system. Lifshitz theory was used to calculate the energy per unit area between flat plates, converted to force/radius between a sphere and a plate using the Derjaguin approximation, then differentiated and multiplied by the radius to obtain the force gradient. The nominal spring constant (force gradient) of the cantilever (0.05 N/m) is shown as the dotted line parallel to the separation axis. The dimensions in the legend refer to the thickness of the water film on each solid. Films of thickness 0−∞ produce jumps of 14−17 nm.

EXPERIMENTAL SECTION

Materials Preparation. Colloid probes were prepared by gluing (Epikote 1004, Shell) soda lime glass spheres, $R \sim 15$ μm, (Duke Standard Cat. No. 9030, Thermo Scientific) to AFM cantilevers (ORC-8 Cantilever D, Bruker Corporation). The force constants of these cantilevers (with spheres attached)

dx.doi.org/10.1021/jp312568y | J. Phys. Chem. C 2013, 117, 6235−6244

were measured with the Hutter method[26] using the light-lever technique in an Asylum instruments MFP-3D. Methods of cleaning samples followed those of Mastropietro and Ducker:[28] glass plates were prepared by cleaning microscope slide cover glass (FisherFinest Premium Cover Glass, thickness No. 1; Fisher Scientific) with deionized water, drying with ultrahigh purity nitrogen (AirGas), rinsing with ethanol, (200 Proof, Decon Laboratory Inc.), followed by drying with nitrogen. Both the colloid probes and the cleaned glass plates were cleaned in O_2-plasma cleaner (200 mTorr, 5 min, 100 W). The O_2-plasma-cleaned glass plate became hydrophilic with advancing water contact angle of 5−10° and the RMS roughness was ∼0.5 nm over a 20 μm × 20 μm surface. Samples prepared in this way are referred to as "hydrophilic". To prepare "hydrophobic" surfaces, hydrophilic samples were further treated with trimethylchlorosilane (TMCS, Aldrich 99+%) in a closed chamber with 3 mL liquid TMCS for more than 2 h. The advancing water contact angle of the hydrophobic plates was 89°. Two hydrophilic and three hydrophobic sets of samples were examined. All five sets were exposed to a polonium α-source at least for an hour to reduce static surface-charge.

AFM Measurements. The damping was measured using a home-built AFM inside a controlled-humidity chamber shown schematically in Figure 4. The deflection of the cantilever was

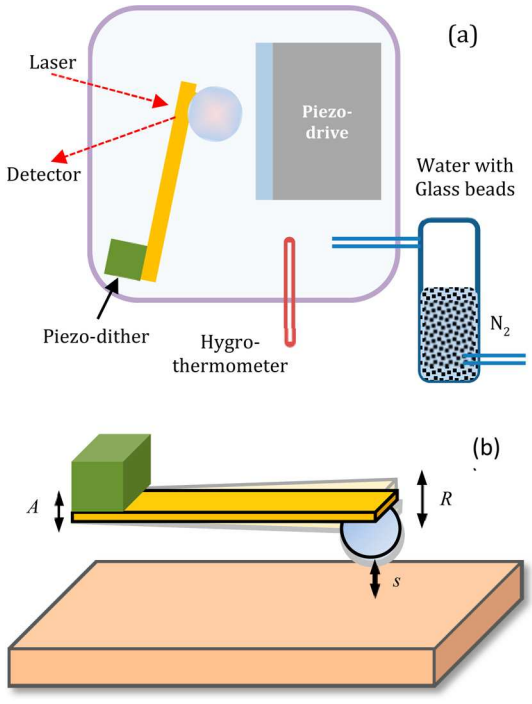

Figure 4. Schematic of apparatus: (a) For controlling the humidity; (b) for measuring the damping.

determined from the cantilever end slope using the light lever technique, and the separation was altered by using a mechanical translation stage (coarse control) and a piezoelectric crystal, (P-753K082, Physik Instrumente GmbH & Co. KG) ("piezo-drive") to which the plate was attached. The piezo-drive was controlled with computer software (E-816, Physik Instrumente GmbH & Co. KG.). The cantilever endslope deflection was monitored with a laser (681 nm, Schäfter + Kirchhoff GmbH) and a split photodiode (Phresh Photonic), amplified, and recorded by an A/D card (PCI-6110, National Instruments).

Thermal Method. The deflection at a particular separation was collected for 1 s at 1 MHz data acquisition frequency. These one million data points were divided into 500 sequential windows of 2000 data points. The data in each window was detrended by subtraction of the best linear fit and then processed using a fast Fourier transform. The transformed data was multiplied by its complex conjugate to provide the power spectral density for one window. The average power spectral density was computed by averaging the spectrum from all 500 windows, and we refer to the result as the measured PSD.[25] At the beginning of each experiment, the PSD was measured when $s = \infty$, and $D(\infty)$ was determined from eqs 5 and 6. The plate was then brought within piezo-drive range (15 μm) using the micrometer. A series of PSDs was measured at series of discrete but diminishing separations, until the plates made contact with the spheres. Figure 5 shows an example of how the PSD changed with separation.

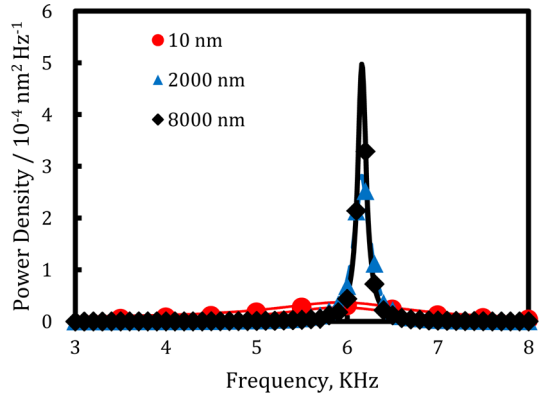

Figure 5. PSD generated from thermal fluctuation as a function of separation. Symbols are from measured data, and lines of the same color are fits to eq 5.

Driven Method. For driven measurements, the clamped end of the cantilever was oscillated with a small piezoelectric crystal (PL022.31, Physik Instrumente GmbH & Co. KG.) ("piezo-dither"). A lock-in amplifier (SR830, Standford Research Systems) was used to sinusoidally drive the piezo-dither and to record the amplitude and phase of the cantilever endslope with a 10 or 100 ms low pass filter. The maximum in R as a function of frequency, R_{max}, was determined at each humidity at $s > 1$ mm, and the relative phase was set to $-\pi/2$ at this frequency. This frequency is called ω_{max}, and the cantilever was driven at ω_{max}, for the rest of the experiment at that humidity. The micrometer was used to bring the plate within range of the piezo-drive. The proximity to the sphere was clear where R dropped to about $R_{max}/2$. The piezo-drive was then used to drive the plate toward the sphere at about 20 nm·s^{-1} for 100 s while the piezo-drive, the deflection of cantilever, R and θ were all recorded with the A/D card at 1 kHz data acquisition frequency. The R and θ data were averaged (100 point running average) to remove noise and then input into eq 11 to determine $D(s)$. The deflection data was used to measure the position of glass−glass contact and the mechanical instability. Typical changes of R and θ with separation are shown in Figure 6.

Humidity Changes. Data measured at 0% relative humidity were measured after dried silica gel was kept in the measurement chamber for 2 h or until the hygro-thermometer indicated zero. The relative humidity was altered by flowing wet

dx.doi.org/10.1021/jp312568y | J. Phys. Chem. C 2013, 117, 6235−6244

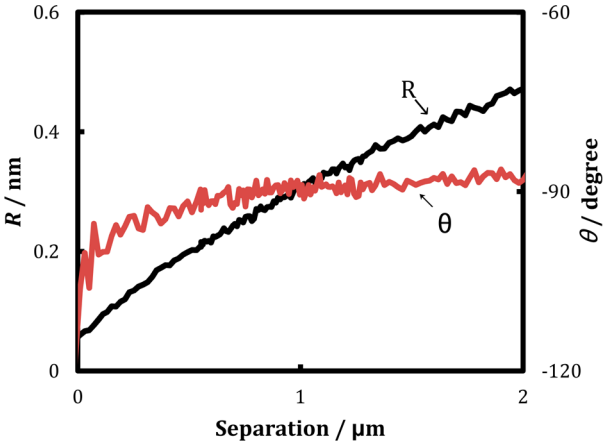

Figure 6. Typical averaged R and θ data.

nitrogen (UHP grade, AirGas) through the chamber until the humidity reached the desired level, as measured by a hygrometer (TH-3, AMPROBE). The error in the humidity measurement is ±3% RH in the range 5−95% RH and ±5% at higher and lower humidity. The nitrogen gas was made humid by passing though water. When the humidity reached the desired level, the nitrogen supply valve and the outlet valve for the chamber were closed at the same time and there was no flow through the chamber. The pressure was maintained at 1 atm, and the temperature was measured by the same TH-3 probe. The temperature in all experiments was 24 ± 1 °C.

QCM Measurements. The borosilicate QCM sensor (QSX336, Q-Sense) was prepared in the same way as the hydrophilic/hydrophobic solids. The sensor was placed inside QCM cell (QCM-D E1, Q-Sense) whose space was saturated with deionized water.

RESULTS

Lubrication in Air between Hydrophilic Solids. Examples of D_{lub} measurements for various humidities are shown in Figure 7a: it is clear that the force is a function of humidity and that the trend with humidity is not monotonic. We also compared our measured data to the Vinogradova equation (eqs 2−4); best fit lines with the slip length as the fitted parameter are shown in in Figure 7a. These fits were made for s > 70 nm because at smaller separations, Kn > 1 and the slip flow theory does not apply. We have included data from the transition region (70−700 nm) in the fit because previously,[16] and here (Figure 7a), the Vinogradova equation still fits the data in this range. Note that we are assuming no flow within the liquid films. The quality of the fits can be seen from the residual plot in Figure 7b. We plot:

$$\text{normalized residual} = \frac{\text{data} - \text{model}}{\text{model}} \qquad (13)$$

The magnitude of the residual varies for different experiments as a result of differences in laser focus, but in general is scattered around zero, so we conclude that the Vinogradova equation provides a good fit to the data. Thus we use the fitted slip lengths as a parameter to describe the data. An exception is the data shown at 88% humidity where the relative residual is systematically high at large separation. For this condition, the D_{lub} is very small (see Figure 7a) so there is a large relative error propagated from our subtraction of $D(\infty)$. Note that the plate and sphere are not identical and may have slightly different slip

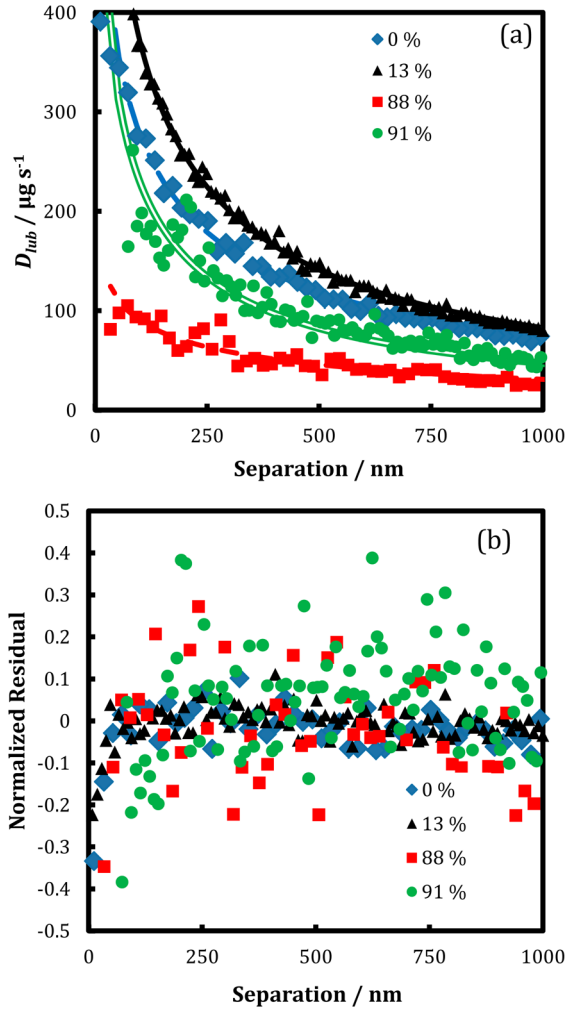

Figure 7. (a) Measured D_{lub} (symbols) for a hydrophilic plate/sphere combination and best fit (lines) to the Vinogradova model as a function of humidity. (b) Normalized residual for fits in part a.

lengths. Previously we showed that small degrees of asymmetry do not have a large effect on the fit,[16] so we cannot resolve asymmetry from the measured data here.

Figure 8 summarizes the fitted slip lengths as a function of humidity for hydrophilic surfaces: clearly the slip length is not a monotonic function of humidity. At 0% humidity the average slip length is 221 ± 17 nm for three samples. The slip length decreases to a minimum at about 6% humidity but then increases to a maximum at 88% humidity before falling again to about 80 nm near 100% humidity. There is agreement between data for the thermal and driven methods.

Lubrication in Air between Hydrophobic Solids. Water cannot form hydrogen bond to the methyl groups on the TMCS surface, so a higher chemical potential (relative humidity) of water is required to drive the same amount of water onto the solid. In addition, the water may be in an altered state in proximity to a non-hydrogen bonding solid, so it is interesting to compare lubrication forces near hydrophilic and hydrophobic solids. Examples of measured damping as a function of separation are shown in Figure 9a,b. The solid lines are fits to the Vinogradova equation for separations greater than 70 nm, again assuming the slip lengths are the same on both surfaces. We again conclude that the Vinogradova model fits

dx.doi.org/10.1021/jp312568y | J. Phys. Chem. C 2013, 117, 6235−6244

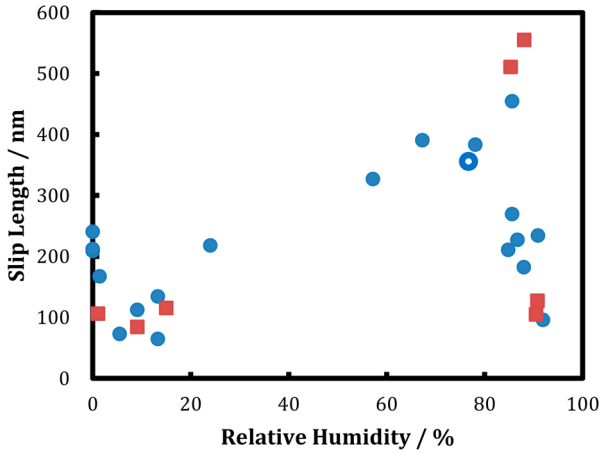

Figure 8. Slip length as a function of relative humidity for hydrophilic glass surfaces. Closed symbols represent measurements using the driven method, whereas the open circles represent data for the thermal method. The squares and circles represent data for two different sets of solids.

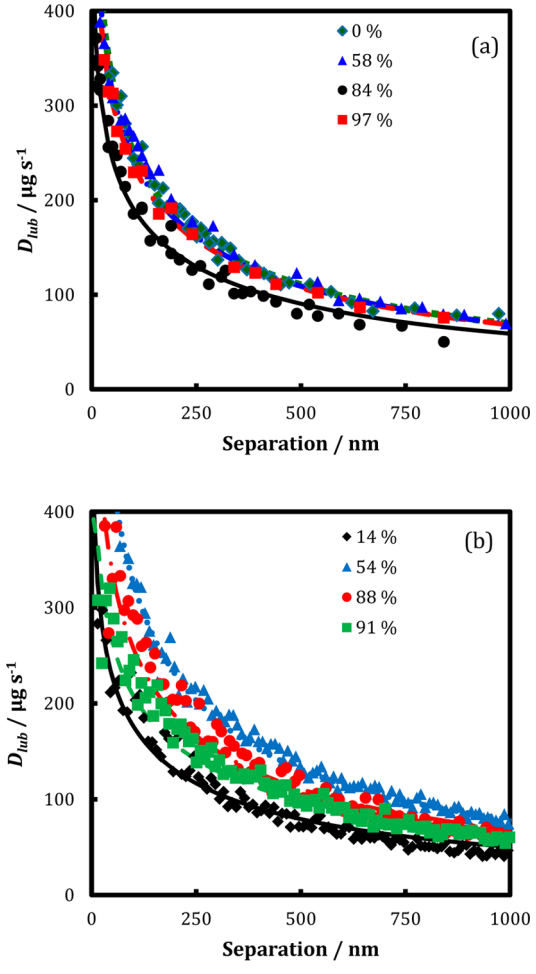

Figure 9. Damping for air between hydrophobic solids as a function of separation and relative humidity. Symbols show the measured data using (a) thermal method and (b) driven method, and lines show best fits to the Vinogradova model.

the data well and that there is little difference between the driven and thermal measurements.

These fitted slip lengths are shown in Figure 10 for three different sphere-plate sets. It is noteworthy that the data is not the same for the three sets, which we attribute mainly to slight differences in the preparation of the TMCS films (as well as to error in the spring constant, ~15%, and sphere radius, ~5%) Although the magnitudes vary even at 0% humidity all three data sets show a constant slip length below 75% humidity (for the humidites measured) then a maximum slip length at about 90 − 92% humidity. The three open points in Figure 10c are for the data collected with the thermal method (while other points are from driven method), again showing that the two methods produce similar results.

To summarize all the data so far, the damping has the same functional form as the Vinogradova equation and shows a strong dependence on humidity. The damping for each of the hydrophilic and hydrophobic solids shows a minimum at high humidity (60−90%), and a maximum near 100% humidity. There is a minimum at low humidity for the hydrophilic solid. Thus the presence of a water film has a large effect on the flow. In the next section we examine the thickness of the water film.

Thickness of Water Layers on Hydrophilic Solids. To enhance interpretation of the lubrication measurements, we would like to know the thickness of the water films. Previous work by Pashley and Kitchener[4] reported a water film thickness of 150 nm on a clean and hydroxylated *quartz* surface at 100% relative humidity, and it would be useful to know how thick the water film is at each humidity for our solids. Here we describe three methods for estimating the film thickness.

The first method is based on the deflection-drive curves, which are shown in Figure 11. From these we can extract J_M, and thus the water film thickness, t, using eq 12. These are shown in Figure 12 as a function of humidity. Clearly the measured water film thickness increases with humidity.

A very approximate estimate of the trends in water film thickness can also be made by comparing ω_{max} at 0% humidity and finite humidity because the added mass of the water layers changes the resonant frequency of the colloid probe. In the experiment here, the distributed load consists of the sphere, with its accompanying water film, and the distributed mass of the cantilever, with its accompanying water film. Therefore:

$$m = [m_s + A_s t_s \rho] + 0.243[m_c + A_c t_c \rho] = \frac{k}{\omega_0^2} \quad (14)$$

where m_s is the mass of the sphere, A_s is its area, t_s is the thickness of the water layer on the sphere, m_c is the mass of the cantilever, A_c is its area, t_c is the thickness of the water layer on the cantilever, and ρ is the density of the water film. The factor of 0.243 accounts for the distribution of the mass of the cantilever and its adsorbed water film along the length of the cantilever. If we assume that the thickness of the water is the same on the sphere and on the cantilever, then the thickness of the water film is given by:

$$t = \frac{k}{\rho(A_s + 0.243A_c)}\left(\frac{1}{\omega_0(H)^2} - \frac{1}{\omega_0(0)^2}\right) \quad (15)$$

where $\omega_0(H)$ is the resonant frequency at a given humidity, H. For the cantilevers used here, $k/\rho(A_s + 0.243A_c) = 9.86 \times 10^{12}$ nm·rad^2·s^{-2}. Note that one side of the cantilever is gold, which could, or is even likely, to have a different thickness of water. The 0.243 factor and the fact that the sphere has a similar area to the entire cantilever means reduces the magnitude of this error, but for this reason, the thickness obtained from the

dx.doi.org/10.1021/jp312568y | J. Phys. Chem. C 2013, 117, 6235−6244

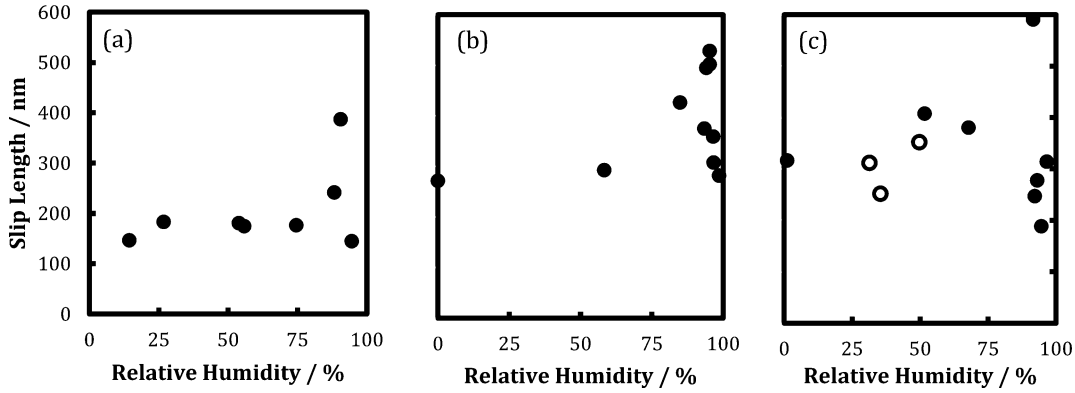

Figure 10. Fitted slip lengths for air between hydrophobic TMCS-coated glass solids as a function of humidity. (a–c) are for different sphere-plate sets. Closed circles are data collected using the driven method, and open circles are for the thermal method.

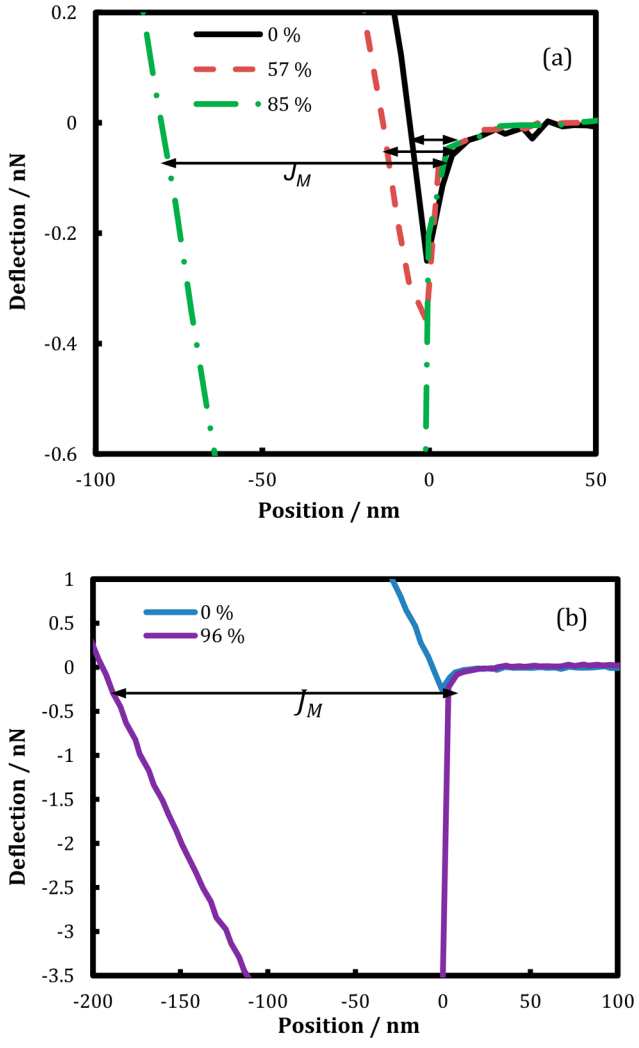

Figure 11. Force curves for a hydrophilic surfaces as a function of piezo-drive position. The jump distance, J_M, increased with increased humidity.

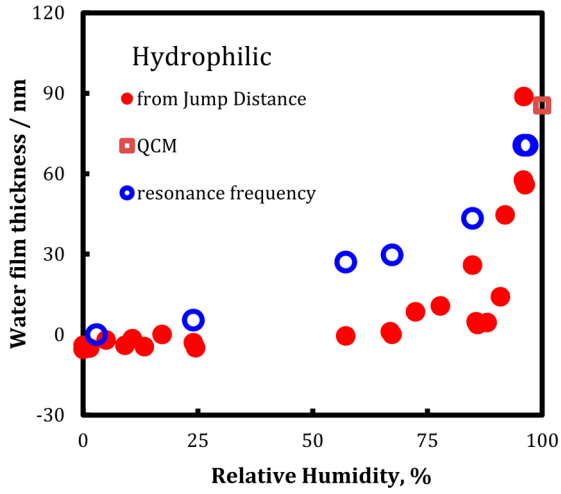

Figure 12. Estimated thickness of water film on hydrophilic solids as a function of relative humidity. The film thickness was estimated from the jump distance (eq 12), the change in resonant frequency (eq 15), and QCM.

frequency is only an approximate estimate. A better estimate could be obtained by measuring the resonant frequency at each humidity with and without the sphere, thereby separately obtaining the average thickness of water on the cantilever. From Figure 12, we see that the thicknesses follow the same trend of increasing thickness with increasing humidity.

Our third estimate of the trends in water film thickness come from quartz crystal microbalance (QCM) measurements of a sensor coated with borosilicate glass at zero and 100% humidity. The difference in frequency enabled us to estimate the film thickness at 100% humidity. The water film thickness can be calculated either with Sauerbrey equation,[29] which assumes a rigid adsorbate, and yields a lower bound for the mass change, or the Maxwell model, which assumes a viscoelastic layer. The Sauerbrey equation gave a minimum film thickness of 85 nm, whereas the Maxwell model gave a thickness of 320 nm for the data. In either case, QCM showed that there was a thick film and provided a thickness that was in the range of those measured by the jump method and the value of 150 nm measured by Pashley and Kitchener[4] at 100% relative humidity. Thus the three different measurements give the same trends, although there is some variation.

Recall that the slip lengths were obtained using a model in which there was no flow within the thin liquid films. The accuracy of this assumption depends on the much greater (50×) viscosity of water compared to air and the relative thinness of the water film compared to the air. We expect to see some failure for small separations at >90% humidity where the water films are up to 90 nm thick. There is some evidence for this in Figure 7b. However, the overall trend to low fitted slip

dx.doi.org/10.1021/jp312568y | J. Phys. Chem. C 2013, 117, 6235–6244

length at high humidity cannot be explained from ignoring flow within the water: unaccounted flow in the water would lead to a greater fitted slip length, yet the fitted slip length falls in this region and is close to the theoretical minimum at high humidity.

Thickness of Water Films on Hydrophobic Solids. The jump distances are shown in Figure 13 and the calculated film thicknesses from the jump distances, changes in cantilever resonant frequency, and QCM are shown in Figure 14. The jump distance and resonant frequency methods agree well. In common with the hydrophilic solids, the water film thickness increases with humidity, but the thickness are much smaller, as expected for a high contact angle solid. The water film thickness remains below 10 nm for humidities up to 80% but then climbs steeply. Pashley and Kitchener[4] report a water film thickness to be about 2 nm at 100% RH on TMCS surfaces prepared with placing the silica plates in 0.04 *M* TMCS solution in benzene,[30] with a water contact angle of about 80° in water. This is much smaller than the values obtained from the force curves and the frequency shift. Therefore, we also estimated the thickness using a borosilicate QCM sensor that was treated with TMCS and had a measured water contact angle of 82°. The water film thickness was 33 nm with the Sauerbrey equation and 44 nm with Maxwell model, confirming that the water film thickness was much greater than determined by Pashley and Kitchener for their samples.

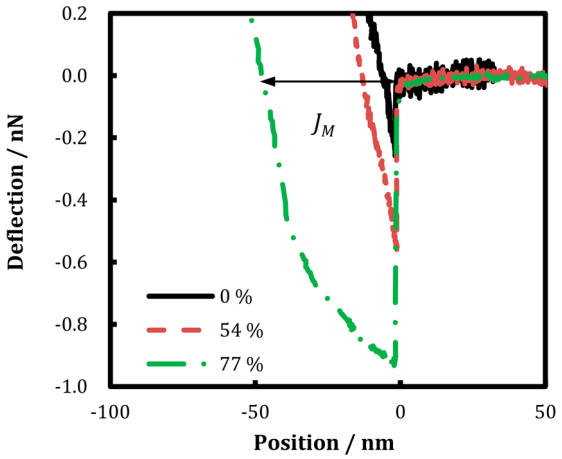

Figure 13. Deflection as a function of piezo-drive position for a (hydrophobic) TMCS-coated sphere and plate as a function of humidity. The jump distance, J_M, increased with increased humidity.

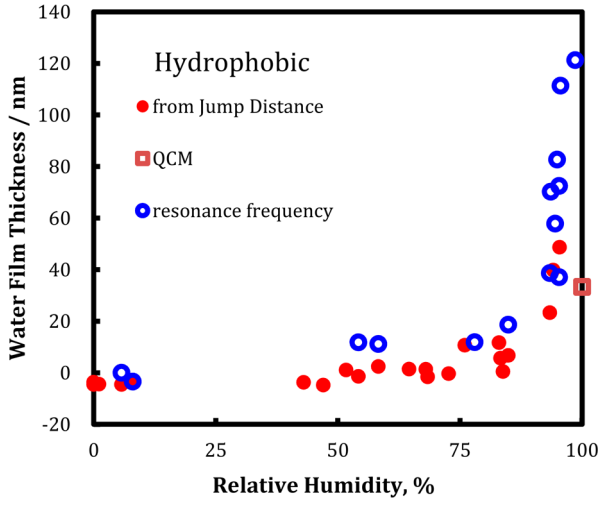

Figure 14. Estimated thickness of water film on TMCS-glass solid water film thickness as a function of humidity determined from the jump distance, from the change in resonant frequency (eq 15), and from QCM.

DISCUSSION

Accommodation Coefficients. The fitted slip lengths for both hydrophilic and TMCS-silica have been converted to accommodation coefficients using eq 1 (see Figure 15). This conversion requires prior knowledge of the mean free path of the gas, which is 70 nm for N_2 at 25 °C and 1.0 atm. Small changes in mean free path due to the varying levels of water vapor (0−0.03 atm) have been neglected. The hydrophilic glass is a smooth (although not atomically smooth) stiff surface, with heavy silicon atom so there is only moderate accommodation on the surface (TMAC ∼ 0.5). When a small amount of water vapor is introduced (<5% RH), the accommodation coefficient increases dramatically (to 0.8−1). We interpret this in terms of the thin layer of water offering opportunities for the N_2 to transfer momentum into translation, vibration and rotation of the light and mobile water molecules.

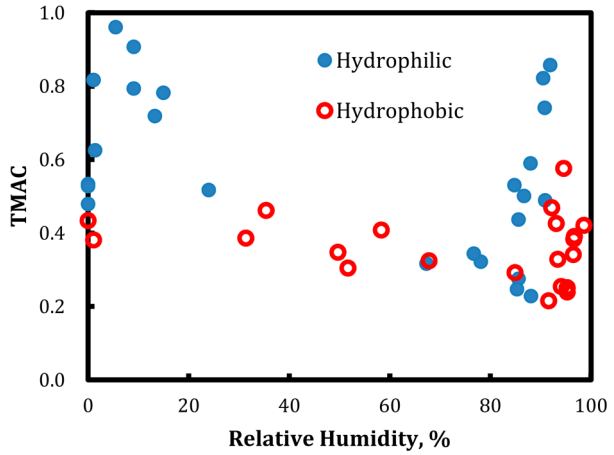

Figure 15. Tangential momentum accommodation coefficients calculated from slip lengths using eq 1, for both hydrophilic and hydrophobic surfaces. Data from Figure 10a not shown.

High accommodation of N_2 is observed near 100% relative humidity for both films. This is easy to rationalize in terms of the N_2 molecules penetrating into a liquid that is similar to bulk water, with opportunities to randomize its momentum through many interactions with the liquid. In contrast, the decrease in accommodation at intermediate humidity is a totally unexpected result, for which the authors have no current explanation. We note only that the effect occurs on both solids, but at different relative humidity (80−88% on hydrophilic silica and about 90−92% on TMCS silica), and occurred for every sample that we prepared.

Effect of Thick Water Films. By experiment, we find that the damping and the accommodation coefficient are independent of the underlying solid when the water film is thick. This is shown in Figure 16, which plots the slip length as a function of film thickness for both the hydrophilic and TMCS silica. This suggests that the nitrogen molecules do not

dx.doi.org/10.1021/jp312568y | J. Phys. Chem. C 2013, 117, 6235−6244

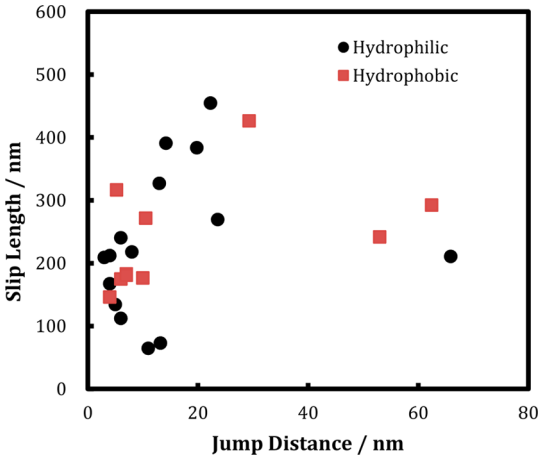

Figure 16. Slip length trends as a function of jump distance for both hydrophobic and hydrophilic solids.

penetrate sufficiently far into the water film to interact with the solid. Note that for each film thickness, the relative humidity and thus the chemical potential of the water is different for the hydrophilic silica compared to the TMCS-silica. Thus the chemical potential of the water is not a good indicator of the accommodation coefficient at all chemical potentials.

Water as a Lubricant in Air. It is interesting that water does act as a lubricant, providing the water layer is not very thick or very thin. On hydrophilic surfaces, the water increases the slip length for the large and frequently encountered humidity range of 25−85% (Figure 8). For TMCS-coated surfaces, water films at least do no harm at low humidity and act as a lubricant in the range 80−92% humidity.

CONCLUSIONS

Increasing the humidity increases the thickness of water films on both hydrophilic and (hydrophobic) TMCS-glass surfaces. The principal difference is that thicker films are formed on the hydrophilic solids for the same relative humidity, as expected for a solid that can hydrogen bond to water. The formation of thin water films leads to changes in the lubrication forces in nitrogen gas and concomitant changes in the fitted slip lengths and accommodation coefficients. Tiny amounts of water greatly increase the accommodation coefficient on hydrophilic glass. We conclude that thin layers of either water provide extra modes of momentum transfer to the solid compared to the stiff and heavy atoms in the silicon oxide. At very high humidity, the nitrogen also accommodates to the solid, which we rationalize in terms of a thick liquid water film that both allows penetration of the nitrogen (and therefore loss of tangential momentum) and provides extra modes for transferring momentum to the solid during reflection. There is also a distinct minimum in accommodation coefficient at intermediate humidity for both the hydrophilic and TMCS-coated silica, for which we do not have an explanation.

AUTHOR INFORMATION

Corresponding Author

*E-mail: wducker@vt.edu.

Notes

The authors declare no competing financial interest.

ACKNOWLEDGMENTS

The authors thank Milad Radiom and Mark Paul for useful discussions, Dmitri Iarakov for help with QCM measurements, and Mike Vaught for machining parts. This research was funded by the National Science Foundation via Award Number CBET-0959228.

REFERENCES

(1) Sundararajakumar, R. R.; Koch, D. L. Non-continuum lubrication flows between particles colliding in a gas. *J. Fluid Mech.* **1996**, *313*, 283−308.
(2) Karniadakis, G.; Beskok, A.; Aluru, N. *Microflows and Nanoflows*; Springer-Verlag: New York, 2005.
(3) Tsilingiris, P. T. Thermophysical and transport properties of humid air at temperature range between 0 and 100 °C. *Energy Converse. Manage.* **2008**, *49*, 1098−1110.
(4) Pashley, R. M.; Kitchener, J. A. Surface forces in adsorbed multilayers of water on quartz. *J. Colloid Interface Sci.* **1979**, *71*, 491−500.
(5) Gee, M. L.; Healy, T. W.; White, L. R. Hydrophobicity Effects in the Condensation of Water Films on Quartz. *J. Colloid Interface Sci.* **1990**, *140*, 450−465.
(6) Maxwell, J. C. On stresses in rarefied gases arising from inequalities of temperature. *Philos. T. Roy. Soc.* **1879**, *170*, 231−256.
(7) Lilley, C. R.; Sader, J. E. Velocity profile in the Knudsen layer according to the Boltzmann equation. *Proc. R. Soc. A: Math. Phys. Eng. Sci.* **2008**, *464*, 2015−2035.
(8) Toennies, J. P. Scattering of molecular beams from surfaces. *Appl. Phys.* **1974**, *3*, 91−114.
(9) Day, B. S.; Shuler, S. F.; Ducre, A.; Morris, J. R. The dynamics of gas-surface energy exchange in collisions of Ar atoms with omega-functionalized self-assembled monolayers. *J. Chem. Phys.* **2003**, *119*, 8084−8096.
(10) Trott, W. M.; Castaneda, J. N.; Torczynski, J. R.; Gallis, M. A.; Rader, D. J. An experimental assembly for precise measurement of thermal accommodation coefficients. *Rev. Sci. Instrum.* **2011**, *82*, 035120.
(11) Vinogradova, O. I. Drainage of a Thin Liquid-fikm Confined Between Hydrophobic Surfaces. *Langmuir* **1995**, *11*, 2213−2220.
(12) Brenner, H. The slow motion of a sphere through a viscous fluid towards a plane surface. *Chem. Eng. Sci.* **1961**, *16*, 242−251.
(13) Ducker, W. A.; Cook, R. F. Rapid Measurement of Static and Dynamic Surface Forces. *Appl. Phys. Lett.* **1990**, *56*, 2408−2410.
(14) Maali, A.; Bhushan, B. Slip-length measurement of confined air flow using dynamic atomic force microscopy. *Phys. Rev. E* **2008**, *78*, 027302.
(15) Honig, C. D. F.; Ducker, W. A. Effect of Molecularly-Thin Films on Lubrication Forces and Accommodation Coefficients in Air. *J. Phys. Chem. C* **2010**, *114*, 20114−20119.
(16) Bowles, A. P.; Ducker, W. A. Gas flow near a smooth plate. *Phys. Rev. E* **2011**, *83*, 056328.
(17) Laurent, J.; Drezet, A.; Sellier, H.; Chevrier, J.; Huant, S. Large Variation in the Boundary-Condition Slippage for a Rarefied Gas Flowing between Two Surfaces. *Phys. Rev. Lett.* **2011**, *107*, 164501.
(18) Lissandrello, C.; Yakhot, V.; Ekinci, K. L. Crossover from Hydrodynamics to the Kinetic Regime in Confined Nanoflows. *Phys. Rev. Lett.* **2012**, *108*, 084501.
(19) Honig, C. D. F.; Ducker, W. A. No-Slip Hydrodynamic Boundary Condition for Hydrophilic Particles. *Phys. Rev. Lett.* **2007**, *98*, 028305.
(20) Honig, C. D. F.; Ducker, W. A. Thin film lubrication for large colloidal particles: Experimental test of the no-slip boundary condition. *J. Phys. Chem. C* **2007**, *111*, 16300−16312.
(21) Honig, C. D. F.; Ducker, W. A. Squeeze Film Lubrication in Silicone Oil: Experimental Test of the No-Slip Boundary Condition at Solid-Liquid Interfaces. *J. Phys. Chem. C* **2008**, *112*, 17324−17330.

(22) Bowles, A. P.; Honig, C. D. F.; Ducker, W. A. No-Slip Boundary Condition for Weak Solid−Liquid Interactions. *J. Phys. Chem. C* **2011**, *115*, 8613−8621.
(23) Cottin-Bizonne, C.; Cross, B.; Steinberger, A.; Charlaix, E. Boundary slip on smooth hydrophobic surfaces: intrinsic effects and possible artifacts. *Phys. Rev. Lett.* **2005**, *94*, 056102.
(24) Honig, C. D. F.; Sader, J. E.; Mulvaney, P.; Ducker, W. A. Lubrication forces in air and accommodation coefficient measured by a thermal damping method using an atomic force microscope. *Phys. Rev. E* **2010**, *81*, 056305.
(25) Seo, D.; Paul, M. R.; Ducker, W. A. A pressure gauge based on gas density measurement from analysis of the thermal noise of an atomic force microscope cantilever. *Rev. Sci. Instrum.* **2012**, *83*, 055005.
(26) Hutter, J. L.; Bechhoefer, J. Calibration of Atomic-Force Microscope Tips. *Rev. Sci. Instrum.* **1993**, *64*, 1868−1873.
(27) Ducker, W. A.; Senden, T. J.; Pashley, R. M. Measurement of Forces in Liquids Using a Force Microscope. *Langmuir* **1992**, *8*, 1831−1836.
(28) Mastropietro, D. J.; Ducker, W. A. Forces between Hydrophobic Solids in Concentrated Aqueous Salt Solution. *Phys. Rev. Lett.* **2012**, *108*, 106101.
(29) Sauerbrey, G. Verwendung von Schwingquarzen zur Wägung dünner Schichten und zur Mikrowägung. *Zeitschrift für Physik* **1959**, *155*, 206−222.
(30) Laskowski, J.; Kitchener, J. A. The hydrophilic-hydrophobic transition on silica. *J. Colloid Interface Sci.* **1969**, *29*, 670−679.

Chapter 5. Effect of Gas Species on Tangential Momentum Accommodation

The work present here is published in Journal of Physical Review C on August 12, 2014 on volume 118, pages 20275−20282. This work presented here discusses another parameter affecting TMAC. A simple hypothesis, rather suspicion for me when I started, that gas species might affect TMAC was proven with experiments. As discussed earlier in Section 1.3, there is no consensus on what property of different gas species affects TMAC. I found out molar mass is the one, proving the point with a mathematical model.

THE JOURNAL OF PHYSICAL CHEMISTRY C

Article

pubs.acs.org/JPCC

Effect of Gas Species on Gas–Monolayer Interactions: Tangential Momentum Accommodation

Dongjin Seo and William A. Ducker*

Department of Chemical Engineering, Virginia Tech, Blacksburg, Virginia 24061, United States

ABSTRACT: The tangential momentum accommodation coefficient (TMAC) of five gas species—He, N_2, Ar, CO_2, and SF_6—was measured on an octadecyltrichlorosilane-coated glass surfaces at 1.0 atm and 24 ± 2 °C. The TMAC was determined from measurement of the damping on a glass sphere near a glass plate when the separation between the sphere and plate was less than 1500 nm so that the flow was at or near the slip-flow regime. The results show that the damping depends on the gas species and that the fitted accommodation coefficient for these gases decreases as the molar mass increases. This trend can be explained using a simple physical model of the collision between two spheres, consisting of an incoming sphere to model the gas and an initially stationary sphere to model part of the monolayer adsorbed on the solid. In this simple model, heavier incoming molecules conserve more average tangential momentum than do lighter molecules. We also consider the possibility of separating a mixture of gases based on differences in TMACs.

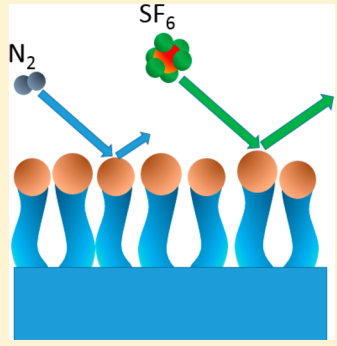

INTRODUCTION

The flow of gas past a solid depends on the flow boundary condition. For macroscopic systems, at atmospheric pressure, the flow is consistent with zero net velocity of the molecules relative to the solid, commonly referred to as the "no-slip" boundary condition. In general, the flow will depend on the Knudsen number

$$Kn = \lambda/L \tag{1}$$

where λ is mean free path of the fluid and L is the characteristic length of the system. The no-slip boundary condition applies only in the continuum limit, $Kn < 0.001$. In the "slip flow regime", $0.001 < Kn < 0.1$, the resistance to flow is lower, which is characterized by a partial slip boundary condition.[1,2] For $Kn > 0.1$, collisions with the solid become a sufficiently high fraction of total collisions that prediction of the flow may require molecular modeling, which has been the subject of much recent interest (e.g., see refs 3−8).

Our focus here lies with the slip flow regime, which applies to two interesting classes of experience: small dimensions and low pressures. For nitrogen at 1 atm, the mean free path is about 70 nm, so the slip flow regime is applicable for 700 nm < L < 70 μm. This is the dimension of nanomicrofluidics and nano-microelectromechanical systems (NEMS and MEMS). In fact, previous measurements show that the assumption of slip flow remains reasonable even for $L \sim 70$ nm at 1 atm ($Kn < 1$),[9−11] which broadens the applicability of the partial slip model. For macroscopic systems ($L \sim 1$ m), the applicable pressure for the slip flow regime is 10^{-4}−10^{-6} atm for N_2. The main application is the reentry of space vehicles, where the vehicle must transition from high vacuum to a full atmosphere. For planets such as Mars, where the surface pressure is 0.004−0.0087 atm (predominantly CO_2),[12] the slip-flow regime applies to a lower part of the atmosphere.

The boundary condition for flow in the slip flow regime is parametized by the slip length, b. The slip length is related to σ, the tangential momentum accommodation coefficient (TMAC), which is defined as

$$\sigma = \frac{p_{x,i} - p_{x,f}}{p_{x,i}} \tag{2}$$

where p_x is the average gas momentum tangent to the solid surface, and i and f refer to the momentum before and after the collision, respectively. In a system of many molecules and a real (inhomogeneous) solid, σ will be an average value over an experiment. In this paper we refer to the TMAC as the "accommodation coefficient" for brevity; we consider no other types of accommodation coefficient here. The accommodation coefficient ranges from zero to one. Starting with Maxwell,[13] many have described the relationship between the slip length and the accommodation coefficient.[14−16] Here we use Maxwell's original expression

$$b = \lambda\left(\frac{2}{\sigma} - 1\right) \tag{3}$$

because more complex formulations result in relatively small corrections to our data and produce the same trends.

Full slip corresponds to $b = \infty$, $\sigma = 0$, and the minimum slip corresponds to $b = \lambda$, $\sigma = 1$. With a range of 70 nm to infinity in air at 1 atm, the accommodation coefficient can have a significant effect on microflows and may also be important for macroflows at low pressure.

Calculation of the accommodation coefficient is very complicated because it depends on the details of the collision

Received: April 7, 2014
Revised: June 24, 2014
Published: August 12, 2014

between the gas and the solid, i.e., the bonding and arrangement of the atoms and the modes energy storage, and requires averaging over all the possible trajectories.

Measurement of the accommodation coefficient has been achieved with a variety of methods,[17−21] but to date, there is considerable variation among results. For example, Arkilic et al.[17] reported TMAC of nitrogen is between 0.75 and 0.85 on micromachined silicon channels, while Colin et al.[18] reported a value of 0.93 in a similar system. Much of the variation probably arises from differences in the solid samples. Often the reported accommodation coefficient is close to one, and sometimes the roughness and details of the sample are not given. For highly roughened or fouled surfaces the accommodation coefficient should approach unity. For smoother and cleaner surfaces, the accommodation coefficient may depend on many factors such as surface chemistry, gas adsorption, and surface roughness, which are not identical in each case. For example, Seo and Ducker[22] showed that the TMAC of N_2 on octadecyltrichlorosilane films on glass surface increases with the surface roughness and changes with humidity.[11] The same group[23] also showed that lubrication can be changed by application of an electric field to an organic monolayer.

Our objective in this paper is to determine whether the species of gas affects the accommodation coefficient and the flow of gas over a solid. We are interested in relatively smooth and well-characterized surfaces, i.e., *not* in the limit where $\sigma = 1$. We examine solids that have been coated with octadecyltrichlorosilane. This coating presents a relatively homogeneous, stable, and hydrophobic layer that allows us to maintain constant conditions over a long period of time and thus to use exactly the same samples for a series of gases. The coating also interacts with the gas. We examine a range of common unreactive gases—He, N_2, Ar, CO_2, and SF_6—which span a range of sizes, molecular masses, and structures. By using smooth surfaces, we expect to be able to distinguish the flow of the gases, based on the differences in the gas−solid collisions. The method we use is to measure the damping of a sphere near a plate in an atmosphere of the gas. The damping is used to determine the slip length and thus the accommodation coefficient as described previously. Note that because different gases can have different viscosities and mean free paths at the same pressure (see Table 1), trends in damping force for different gases cannot be used to determine trends in accommodation coefficients.

Table 1. Gas Data[a]

gas	m	η	λ
He	4	19.9	200
N_2	28	17.9	68
Ar	40	22.7	72
CO_2	44	15.0	45
SF_6	146	15.3	25[24]

[a]Values are from ref [25] except λ for SF_6. m = molar mass/(g mol^{-1}), η = viscosity/(μPa·s) at 300 K, and λ = mean free path/nm at 1 atm and 298 K.

Previous researchers have investigated the relationship between gas species and measured TMAC, but there is no clear consensus. For example, TMAC was found to decrease as molar mass increases on silica tubes and channels,[26−28] whereas others found no clear relation between TMAC and molar mass.[9,29,30] The TMAC should also depend on the surface roughness, and there may be an interaction between the effects of roughness and gas species. The solids investigated in refs 26−30 were all silica surfaces; the roughness varied but was about 20 nm. Recently, Sedmik et al.[9] measured the TMACs of a variety of gases on gold surfaces with the same sphere-and-plate geometry used here. The root-mean-square (rms) roughness of the plate was 2.5 ± 0.3 nm and of the sphere was 9.7 ± 3.3 nm. They did not find a relationship between TMAC and molar mass; instead, they reported that TMAC decreases as the mean free path increases. In this paper, we investigate the relationship between TMAC and the gas species, but with smoother, coated surfaces that we expect to enable us to discern the effect of the gas molar mass.

THEORY OF EXPERIMENT

The outline of our procedure is to measure the damping on a sphere that is near a plate and then compare the theoretical and experimental values of the lubrication force to obtain the best fit to either the slip length or the accommodation coefficient.

For the sphere−plate geometry when the radius of the sphere is much greater than the slip length, the mean free path, and the separation between the sphere and the plate, the lubrication coefficient $D_{lub}(h)$ is[31]

$$D_{lub}(h) = D(h) - D(\infty) = \frac{6\pi\eta R_s^{\,2}}{h} f^*(h, b) \tag{4}$$

where

$$f^* = \frac{h}{3b}\left[\left(1 + \frac{h}{6b}\right)\ln\left(1 + \frac{6b}{h}\right) - 1\right]$$

and h is the distance between the sphere and the plate, $D(h)$ is the damping coefficient, η is dynamic viscosity of the gas, R_s is the radius of the sphere, and b is the slip length, which we have assumed is identical on both surfaces. This expression is the limit of the damping for two spheres when the radius of one sphere becomes very large.

Thus, the slip length can be determined by comparing a measurement of the damping to eq 4, providing η, r, and h are known. The accommodation coefficient can be determined by substituting eq 3 into eq 4 and comparison to experiment. In practice, greater accuracy is obtained when the lubrication force is measured as a function of separation because a range of separations constrains the fit. In any case one usually needs to measure a range of separations in order to establish the zero of separation.

The damping was obtained from the colloid probe technique[32] in which the force on the sphere ("probe") is measured with the deflection of a cantilever to which the sphere is attached. In our experiment, we measured the damping by the method of Ducker and Cook[33] where the "clamped end" of the cantilever was oscillated while the amplitude and phase of the "free end" of the cantilever are measured. When the driving frequency of the clamped end of cantilever is set to $\omega_0(\infty)$, the damping is given by

$$D(h) = -\frac{k}{\omega_0(\infty)}\frac{A}{R(h)}\sin\theta(h) \tag{5}$$

where k is the spring constant, $\omega_0(\infty)$ is resonance frequency of the cantilever at $h = \infty$, A is the amplitude of oscillation at the clamped end of cantilever, $R(h)$ is the amplitude of oscillation at the free end of cantilever, and $\theta(h)$ is the phase difference between the free and clamped ends of the cantilever.

dx.doi.org/10.1021/jp503416x | J. Phys. Chem. C 2014, 118, 20275−20282

A, $R(h)$, and $\theta(h)$ are obtained from a lock-in amplifier. $D_{lub}(h)$ is then obtained from $D_{lub}(h) = D(h) - D(\infty)$.

EXPERIMENTAL SECTION

Materials Preparation. A soda lime glass sphere, $r \sim 15$ μm (Duke Standard Cat. No. 9030, Thermo Scientific), was glued to the free end of a cantilever (ORC-8 Cantilever D, Bruker Corporation) with epoxy glue. A microscope cover glass (FisherFinest Premium Cover Glass, thickness No. 1; Fisher Scientific) was cut to the appropriate size (around 1 cm by 1 cm) and will be described as the "plate". The plate was cleaned with ethanol (200 Proof, Decon Laboratory Inc.) and deionized water and dried with compressed ultrahigh purity nitrogen (AirGas). The plate and sphere were further cleaned with oxygen plasma cleaner (200 mTorr, 5 min, 100 W). Immediately after plasma cleaning, they were immersed in 5 mM octadecyltrichlorosilane (OTS, ≥90%. Sigma-Aldrich) solution in hexadecane for 24 h. The plates were rinsed twice by immersion in chloroform and sonicated to remove residual hexadecane. The plate was blown dry with nitrogen. The cantilever−sphere was immersed in pentane to remove hexadecane. After they were rinsed three times, they were dried by blowing with nitrogen. These steps were repeated five times to produce five sets of one sphere and one glass plate.

Roughness of Plates and Spheres. The surface roughness was measured by an Asylum Research Cypher atomic force microscope with an ORC-8 cantilever B (Bruker). The rms roughness of the plate was in the range 0.22−0.25 nm.

Damping Measurement. After the materials were ready, they were placed in a sealed chamber as soon as possible. The overall setup is shown in Figure 1. The cantilever with the sphere was glued on to a small piezoelectric crystal (PL022.31, Physik Instrumente GmbH & Co. KG.) ("piezo-dither"). One of the OTS-coated microscope cover slides was attached to a piezoelectric translational stage (P-753 K082, Physik Instrumente GmbH & Co. KG) ("piezo-drive"), which was attached to a mechanical translation stage (coarse control). Both the sphere and the glass plate were exposed to polonium α-source at least for 30 min to remove static charge. Dry silica gel was added to the chamber to remove any residual humidity. After sealing, the chamber was purged with desired gas (helium, nitrogen, argon, carbon dioxide, or sulfur hexafluoride).

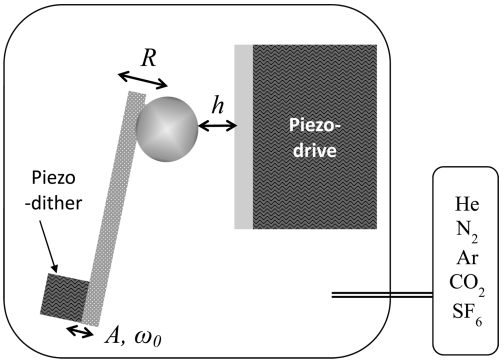

Figure 1. Schematic of experiment. The cantilever is driven at the "clamped" end by the piezo-dither with an amplitude, A, and frequency, ω, which, in this paper, is always fixed at the resonant frequency at large separation. The piezo-drive alters the separation between the sphere and the plate. The chamber is sealed then purged with one of the gases.

While piezo-dither was driven with a lock-in amplifier (SRS830, Stanford Research Systems), the cantilever deflection was monitored with a laser (681 nm, Schäfter+ Kirchhoff GmbH) and a split photodiode (Phresh Photonic), and the phase and amplitude relative to the drive were monitored by the lock-in amplifier. The separation, h, was measured from the change in movement of the piezo-drive and the deflection of the cantilever. The zero of separation was determined from the sudden and linear change in deflection that occurs when the sphere touches the plate.[34] The R and θ outputs from the lock-in amplifier were recorded with an A/D card (PCI-6110, National Instruments) connected to a computer. The range of the piezo-drive was 2 μm over a period of 100 s. R, θ, and raw cantilever deflection data were recorded at 1 kHz frequency with a 10 ms time constant. Typical values are R = 4 nm and A = 0.05 nm. These data were averaged by 100 to reduce the data size. The detailed discussion regarding determining h data processing is found in ref 11. k was obtained from the Hutter method.[35]

Each "experiment" used a different sphere−plate set. For each experiment, damping was measured on 3−5 different gases. For each gas, about five different damping-separation "runs" were measured to reduce measurement error. The temperature of the apparatus was maintained in the range 22−26 °C and measured with an uncertainty of ±0.8 °C (AMPROBE TH-3). Both the viscosity and the mean free path of a gas depend on the temperature, so in the analysis of each run, we adjusted the values shown in Table 1 to the measurement temperature using the ideal gas approximations, $\eta \propto T^{1/2}$ and $\lambda \propto T$,[36] where T is the temperature in K.

In our analysis, we attribute all the distance dependence of the damping of the AFM probe to the sphere and ignore the distance dependence of the contributions from the cantilever. We examined this assumption by measuring the damping on a cantilever (without sphere attached) as a function of separation. When the cantilever was separated from the plate by distances greater than one sphere diameter, we found by experiment that the variation in damping with distance was insignificant.

RESULTS

Damping Coefficient Depends on the Gas Species. The measured damping coefficient for the lubrication force, $D_{lub}(h)$, in the sphere−plate geometry is shown in Figure 2 for both N_2 and He gases at 1.0 atm for a single run in one experiment. $D_{lub}(h)$ was obtained using eq 5. The first conclusion of this paper is that the damping coefficient depends on the gas species for these OTS-coated surfaces.

Damping Coefficient Is Well-Described by the Vinogradova Equation. As described in the Introduction, Vinogradova derived the expected functional form of this damping coefficient (eq 4). Figure 2 shows the best fit of eq 4 in the range $\lambda < h < 1700$ nm to the measured data when the slip length is a fitted parameter. The upper limit of h was chosen because of (a) the need to maintain $h \ll r$ and (b) the increasing error of subtracting D_∞ at larger separation, and the lower limit was chosen to keep $Kn < 1$. The quality of the fit is good, as assessed by the residual plot for He in Figure 3. For He, the fit is good even to for $h = \lambda/2 = 100$ nm. It is interesting that the fit of the continuum model is still good in the transition regime, all the way to $Kn \sim 1$. We find a similar result for the other gases: departures from the continuum (Vinogradova) theory start to occur in the range $Kn > 0.5$. The

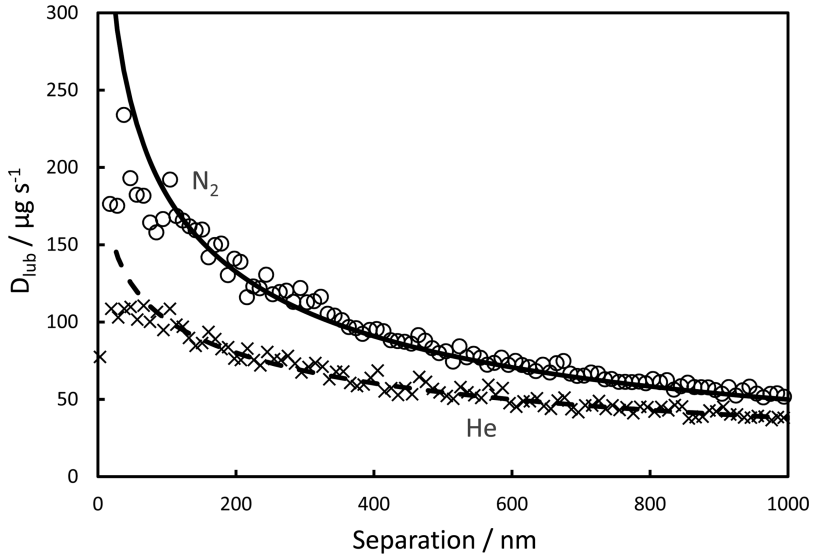

Figure 2. Measured damping coefficient attributed to the lubrication force (D_{lub}) as a function of separation between the sphere and the plate. Points are for experimental data (○: nitrogen; ×: helium) whereas lines are the best fit to eq 4. where the slip length is treated as a free parameter while pressure and temperature are kept at 1.0 atm and 298 K. The best fits for the data in this figure are b = 440 nm for nitrogen and b = 780 nm. It is important to note that differences in the accommodation coefficients cannot be inferred, even qualitatively, from the damping data. Although helium has much lower damping that N_2 at a given separation, there is a modest contribution due to the viscosity difference and a large effect of the difference in mean free path that must be removed to reveal the accommodation coefficient.

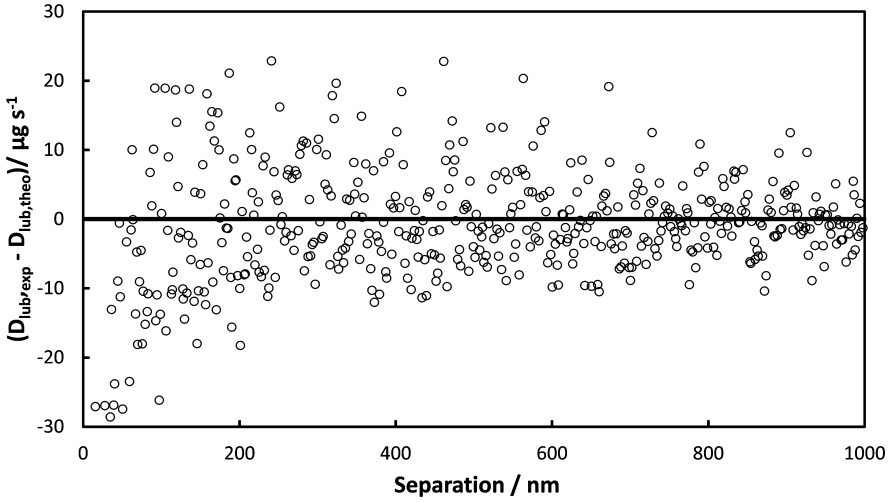

Figure 3. Residual plot for fit for b on the He data shown in Figure 2.

quality of the fit suggests that Vinogradova theory applies and that the data can be used to obtain the slip length.

Accommodation Coefficient Depends on the Gas Species. Values of σ for each gas were obtained from fits of D_{lub}(measured) to D_{lub}(theoretical). An expression for D_{lub}(theoretical) as a function of σ was obtained by substituting eq 3 into eq 4. As stated in the Introduction, several authors have derived different versions of eq 3 with slightly different dependences on σ. These alter the exact values of σ, but not the trend. However, a different dependence on λ could, in principle, alter the trend. In this work, we performed four experiments, each with a different sphere−plate combination. For each experiment, we performed several (∼5) R−θ−h runs. For each run, we obtained a fitted value of σ. We also separately fitted b from equation eq 4. We then averaged σ values to obtain σ for that experiment and likewise averaged b for each run to obtain b for the experiment. The reason for not simply fitting b and then obtaining σ from the average b is that σ and b are not linearly related. The average values of σ and b for each gas are shown in Table 2 and plotted as closed circles in Figure 4. Because changes in the value of R dominate changes in D_{lub}, and the two are inversely proportional, we also investigated using minimizing the residuals on $1/D_{lub}$, but the differences in fitting parameters were small. The errors shown in Table 2 are standard errors calculated from the distribution of results from different experiments and do not include uncertainty in the mean free path, viscosity, or error associated with the use of eq 3.

The data in Figure 4 show a systematic trend in the accommodation coefficient: it decreases with increasing molar mass. In contrast, the slip length does not show an obvious trend with molar mass. For example, CO_2 and Ar have about the same molar mass, yet the measured slip lengths were 375 and 600 nm, respectively, for the conditions measured here.

dx.doi.org/10.1021/jp503416x | J. Phys. Chem. C 2014, 118, 20275−20282

Table 2. Tangential Momentum Accommodation Coefficient and Slip Length[a]

		σ		b (nm)	
	molar mass (g/mol)	av	95% conf	av	95% conf
He	4	0.38	0.1	840	230
N_2	28	0.25	0.015	490	40
Ar	40	0.21	0.05	600	20
CO_2	44	0.203	0.003	375	80
SF_6	146	0.142	0.03	325	40

[a]av = average value 95%; conf = critical value of t-distribution × standard error. Note: the accommodation coefficients and the slip length were each obtained from a separate fit to the same D_{lub} data.

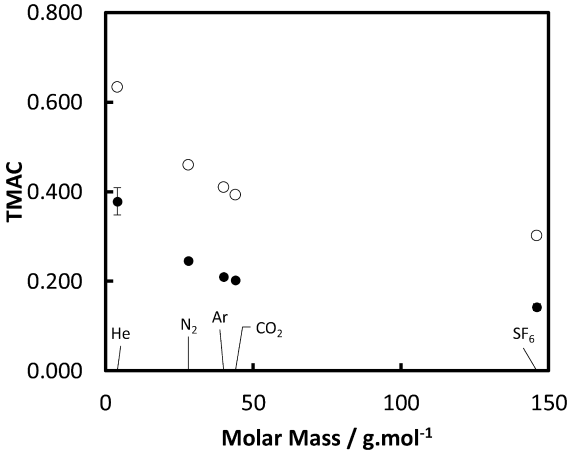

Figure 4. Relationship between TMAC and molar mass of colliding gas molecules on OTS-coated surfaces at 1.0 atm and 298 K. TMAC was obtained from the best fit of σ to eqs 3 and 4. Closed circles represent the result from four different sets of a glass sphere and plate. The standard errors are shown in Table 2. Open circles are for a single experiment using a plate with greater rms roughness.

The significance of differences in the measured values of σ was assessed using a t-test, and the results are shown in Table 3. The results show that there is a high likelihood ($p < 0.05$) that the accommodation coefficients of the various gases are different, with the exception of Ar and CO_2.

Table 3. p-Values from t-Tests Comparing Accommodation Coefficients from Two Gas Types

	N_2	Ar	CO_2	SF_6
He	0.021	0.021	0.010	0.0013
N_2		0.0089	0.012	<0.001
Ar			0.19	0.0078
CO_2				0.017

Accommodation Coefficient Depends on the Surface Roughness. A preliminary study of the effect of the surface roughness on the accommodation coefficient was performed by measurement of the damping coefficient on a single sample set that was rougher (0.48 nm) than those described above (in the range 0.22−0.25 nm). The results for the rougher sample, shown by the open circles in Figure 4, suggest that (a) rougher samples produce a higher accommodation coefficient for each gas and (b) the overall trend of smaller accommodation coefficient for larger molar mass is maintained even for rougher samples.

DISCUSSION

Relationship between Accommodation Coefficient and Molar Mass. The accommodation coefficient is a parameter that accounts for the average conservation of gas tangential momentum during collisions with the solid and therefore depends on all the details of the collision between the gas and solid, including the masses and forces acting on all the atoms in both the gas and solid, and the modes in which energy can be dissipated or transferred. In this paper we have a limited set of data for one type of solid at a single pressure and temperature, but we do observe a simple trend in the data: the accommodation coefficient decreases with molar mass. One possible reason for this trend is that molar mass is in some way a proxy for size. Smaller molecules are able to respond to a smaller scale of roughness. If such a length scale existed on the surface, it would be additional roughness for the smaller molecules, which would lead to greater accommodation. The comparison between Ar and CO_2, which have very similar accommodation coefficients and masses, yet very different sizes, provides some limited argument against this hypothesis.

In this discussion, we examine a simple reason why the accommodation coefficient might depend on mass and ignore for now the complexities of the transfer of energy into various modes by considering the collision between two structureless spheres. The rationale behind a sphere−sphere model is that the solid is coated with OTS molecules. Our coarse model is that the omega (terminal) part of the OTS molecule is a sphere that can move. Clearly, an OTS molecule has internal structure, and the movement of the omega portion is restricted by intermolecular interactions and binding to the solid. This is simply a first-order model to examine the effect of the adsorbed molecule on the collision with the gas.

For simplicity, we start by considering a one-dimensional collision between a moving object of mass m_1 (modeling our gas) and an initially stationary object m_2 (part of our solid) that conserves both total kinetic energy and total momentum. The velocity of object 1 after the after collision, v_1, is

$$v_1 = \left(\frac{m_1 - m_2}{m_1 + m_2}\right)u_1 \tag{6}$$

where u_1 is the velocity before the collision. From this equation, we see that if m_2 is the same order as m_1, then $v_1(m_1)$ is a monotonically increasing function with a limit of u_1 when $m_1 \gg m_2$: the greater the initial mass on the gas molecule, the larger the fraction of velocity and thus momentum is retained. This is equivalent to a lower accommodation coefficient with greater mass, as observed in our experiments.

Of course, this is a highly simplified picture. The easiest part to remedy is to consider a two-dimensional collision, which is a much more realistic picture of the collision that we are examining; yet we see below that the outcome is much the same. Figure 5 shows a model where we now consider two spheres of equal radius where the incident sphere collides with an incident angle, φ, relative to the overall plane of the surface of the solid. We define the collision angle, θ_C, as the angle between the incident velocity and the line between the centers of the spheres in contact. After the collision mass 1 moves at an angle θ_1' relative to the surface plane and mass 2 moves at an angle θ_2'. Note that u_1, v_1, and v_2 are all scalars representing the magnitude of velocity vectors. In this model, we assume or designate m_1, m_2, u_2 (= 0, stationery), and θ_2' are known. Therefore, we are left with three unknowns: v_1, θ_1', and v_2. To

dx.doi.org/10.1021/jp503416x | J. Phys. Chem. C 2014, 118, 20275−20282

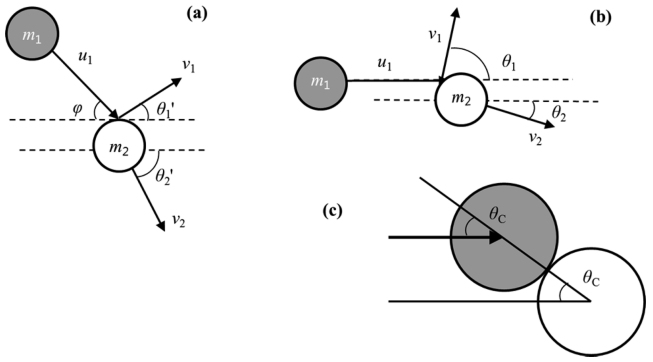

Figure 5. Collision schematics. (a) m_1 colliding with m_2 with incident angle φ. (b) Same as (a), but the trajectories have been rotated by $-\varphi$ so that u_1 in the vertical direction is zero. (c) θ_C is defined to be the angle between the incident trajectory and the center-to-center line at contact.

simplify this problem, we rotate our reference line by $-\varphi$ so that the incident velocity lies collinear with the reference line. This leaves three unknowns: v_1, θ_1, and v_2. Though the reference frame is rotated, all parameters are the same except for angles. θ_1 and θ_2 are angles after rotation. θ_2 is equal to θ_C in this case. The problem then looks similar to the one-dimensional case, except that the collision can be offset, and the final velocities can have different directions.

Three quantities are conserved in the collision: kinetic energy, eq 7, tangential momentum, eq 8, and momentum in the normal direction, eq 9:

$$\frac{1}{2}m_1{u_1}^2 = \frac{1}{2}m_1{v_1}^2 + \frac{1}{2}m_2{v_2}^2 \tag{7}$$

$$m_1u_1 = m_1v_1\cos\theta_1 + m_2v_2\cos\theta_2 \tag{8}$$

$$m_1v_1\sin\theta_1 - m_2v_2\sin\theta_2 = 0 \tag{9}$$

Solving eqs 7−9 yields

$$v_1 = \frac{\sqrt{{m_1}^2 + {m_2}^2 - 2m_1m_2\cos 2\theta_C}}{m_1 + m_2}u_1 \tag{10}$$

$$\theta_1 = \tan^{-1}\left(\frac{m_2\sin 2\theta_C}{m_1 - m_2\cos 2\theta_C}\right) \tag{11}$$

To calculate TMAC, we need the change in momentum of particle 1 in the plane of the solid surface (Figure 5a) so we must transform the angels back: $\theta_1' = \theta_1 - \varphi$, since the new reference frame has to be rotated by φ to return to the previous frame. Therefore, according to the definition of TMAC (eq 2)

$$\sigma = f(m_1, m_2, \theta_C, \varphi) = 1 - \frac{v_1\cos(\theta_1 - \varphi)}{u_1\cos\varphi} \tag{12}$$

Figure 6 shows plots of the accommodation coefficient as a function of m_1 using eqs 10−12 for the example of $\varphi = 45°$. We do not know m_2, but for our experiments here, it represents some part of the end of the OTS. Therefore, we plot a range of masses, starting with the mass of the terminal methyl group (m = 15 g mol^{-1}).

Figure 6a shows the accommodation averaged over $-90° < \theta_C < 90°$ range. This range includes all molecules that have an initial velocity from the left in Figure 5a; i.e., we are considering the slight excess of molecules that flow to the right in a flow. This is somewhat unrealistic because it included gas molecules that come from within the solid, which produces many collisions where the incoming gas molecules reverses direction and gives a high accommodation coefficient. To make the model more realistic, in part b we show the results only when the gas molecule is reflected above the solid, $\theta_1' > 0$, which occurs when the collisions occurs above the center line of the sphere in Figure 5a. Comparing Figures 5a and 5b, this restriction on the initial angles brings the maximum value of the accommodation coefficient below 0.5. Comparing now the calculation shown in Figure 5b with the data in Figure 4, we see that the 2D model produces the appropriate trend shown in the data.

The important point is that, regardless of whether we consider a one-dimensional or two-dimensional model, the value of the TMAC decreases with the mass of the gas molecule, which is the same trend as observed in the experimental data for the five gases on OTS films and therefore is a possible explanation for the trend. This trend may be useful for predicting the boundary conditions for one gas when the value a different gas is known on the same solid.

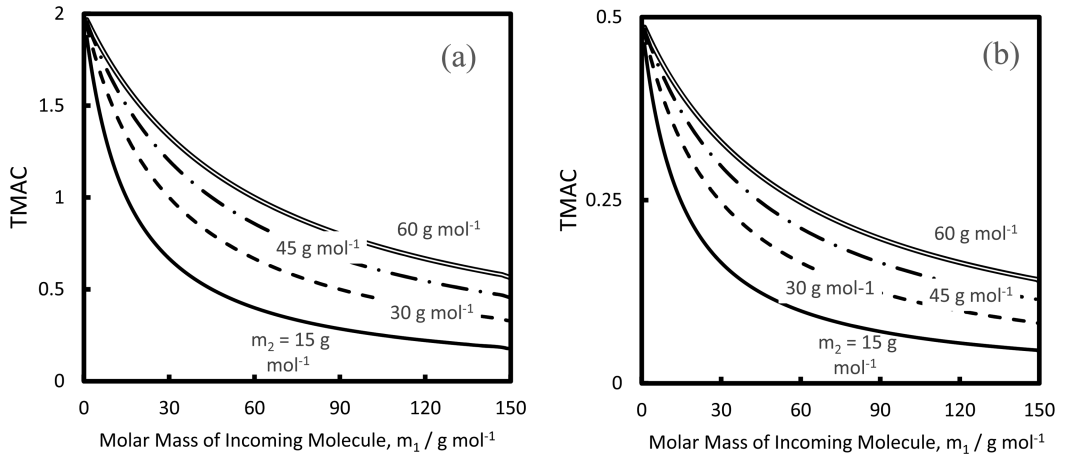

Figure 6. TMAC calculated for a simple two-dimensional collision between two spheres shown in Figure 5a. Each line represents a calculation using a different value of m_2. (a) Average for collisions in the range: $-90° < \theta_C < 90°$. (b) Average for collisions in the range: $0 < \theta_C < 90° - \varphi$.

dx.doi.org/10.1021/jp503416x | J. Phys. Chem. C 2014, 118, 20275−20282

We caution that this relationship between accommodation coefficient and molar mass may not be universal. For example, one expects all rough surfaces to have accommodation coefficients of around one, and therefore one expects no observable trend with molar mass for very rough surfaces. Also, our simple calculation required a light body (e.g., a methyl group) on the surface to absorb the momentum, so it would not apply if there were no such body to accept the momentum.

Application to Gas Separation. A separation based on differences in momentum conservation during collisions with walls has been discussed by Arya et al.[3] Unlike conventional chromatography, where the separation depends on differences in adsorption or filtration, where the separation depends on differences in molecular size, such a separation would depend on differences in momentum accommodation and mean free path of two gas species. For such a separation to be effective, the forward progress of the molecule through the separator must be dominated by collisions with the walls rather than with other molecules because collisions between different species equilibrate the forward momentum between different species. Thus, the application requires Kn near or above 1.

Arya et al.[3] used simulation to show that two identical gases can be separated provided that the accommodation coefficients are different and compared the results to continuum theory. They found that continuum theory shows that same trends at $Kn \sim 1$ but underestimates the degree of separation by neglecting the attractive intermolecular forces that tend to concentrate gas molecules at the walls.

Having demonstrated here that the measured accommodation coefficient varies by gas species, we are now in a position to estimate the effectiveness of such a separation. We use continuum theory (based on the Navier−Stokes equation (NSE)) similar to that by Arya et al. to calculate the ratio of volumetric flows of the two gases, S, in a cylindrical tube, diameter, R_T:

$$S = \frac{1 + \frac{4}{P^*}\frac{\lambda_1}{R_T}\left(\frac{2}{\sigma_1} - 1\right)}{1 + \frac{4}{P^*}\frac{\lambda_2}{R_T}\left(\frac{2}{\sigma_2} - 1\right)} \tag{13}$$

where subscripts 1 and 2 refer to the different gases, P is the inlet pressure, and P^* is a dimensionless pressure defined as $(P_0/P_L - 1)/\ln(P_0/P_L)$. In contrast to Arya's calculation, we allowed the necessary pressure difference at inlet (P_0) and outlet (P_L) to drive flow, which causes variation in the slip length down the tube for constant accommodation coefficient, and ignored differences in viscosity between the gases.

Using eq 13, we consider a sample calculation for the flow of a mixture of N_2 and O_2 at $Kn \approx 1$. This example examines a separation utilizing σ alone because N_2 and O_2 have very similar λ so the separation is based on σ. We consider a single position where there is an equimolar mixture of two gases. From eq 13, the ratio of volumetric flows, $S \approx 0.96$ (i.e., a 4% difference) when $P_0 = 1/14$ atm, $P_L = 1/28$ atm, and $R_T = 1$ μm. Here we chose a subatmospheric pressure to achieve $Kn \approx 1$ at the inlet with an easily achieved cylinder size. Alternatively, if atmospheric pressure is required at the inlet, a smaller value of $R_T = 70$ nm would be required to achieve $Kn \approx 1$. In this calculation, the viscosity and mean free path of the mixed gas were calculated using mean values from two gases, and the accommodation coefficient for O_2 was interpolated based on its molar mass. The ratio of the flows is relatively insensitive to $R_T < 1$ μm, so it is not necessary to use a pore with dimensions similar to the size of the molecule, but only on the order of the mean free path. Obviously, much larger differences in flow rate are expected to occur for pairs of gases that have greater differences in TMAC and λ. (e.g., He/SF_6). Thus, differences in accommodation coefficients alone should be able to separate gases on OTS-coated surfaces and perhaps on other surfaces.

CONCLUSION

For a series of five different gases—He, N_2, Ar, CO_2, and SF_6—the tangential momentum accommodation coefficient on OTS-coated glass surfaces was found to depend on the gas species, and in particular, the accommodation coefficient decreased as the molar mass increased. This trend can be explained using a simple physical model of the collision between two molecules: an incoming molecule to model the gas and an initially stationary molecule to model part of the monolayer adsorbed on the solid. In this simple model, heavier incoming molecules conserve more average tangential momentum than do lighter molecules, consistent with our observations. Accommodation coefficients are specific to particular surface conditions, and it is possible that the relationship to molar mass may depend on the particular surface.

The accommodation coefficients could be used to determine the flow boundary conditions for these surfaces in other geometries. In addition, the method used here could be used to determine the accommodation coefficient for other combinations of gases and solids and thus to determine the flows for these solids in a variety of geometries.

AUTHOR INFORMATION

Corresponding Author

*E-mail: wducker@vt.edu (W.A.D.).

Notes

The authors declare no competing financial interest.

ACKNOWLEDGMENTS

This research was funded by the National Science Foundation via Award CBET-959228.

REFERENCES

(1) Karniadakis, G.; Beskok, A.; Aluru, N. *Microflows and Nanoflows*; Springer-Verlag: New York, 2005.

(2) Frangi, A.; Spinola, G.; Vigna, B. On the Evaluation of Damping in MEMS in the Slip-Flow Regime. *Int. J. Numer. Methods Eng.* **2006**, *68*, 1031−51.

(3) Arya, G.; Chang, H. C.; Maginn, E. J. Molecular Simulations of Knudsen Wall-Slip: Effect of Wall Morphology. *Mol. Simul.* **2003**, *29*, 697−709.

(4) Barisik, M.; Beskok, A. Surface-Gas Interaction Effects on Nanoscale Gas Flows. *Microfluid. Nanofluid.* **2012**, *13*, 789−98.

(5) Bhatia, S. K.; Bonilla, M. R.; Nicholson, D. Molecular Transport in Nanopores: A Theoretical Perspective. *Phys. Chem. Chem. Phys.* **2011**, *13*, 15350−83.

(6) Nicholson, D.; Bhatia, S. K. Fluid Transport in Nanospaces. *Mol. Simul.* **2009**, *35*, 109−21.

(7) Prabha, S. K.; Sathian, S. P. Molecular-Dynamics Study of Poiseuille Flow in a Nanochannel and Calculation of Energy and Momentum Accommodation Coefficients. *Phys. Rev. E* **2012**, *85*, 041201.

(8) Schlamminger, S.; Hagedorn, C. A.; Gundlach, J. H. Indirect Evidence for Levy Walks in Squeeze Film Damping. *Phys. Rev. D* **2010**, *81*, 123008.

(9) Sedmik, R. I. P.; Borghesani, A. F.; Heeck, K.; Iannuzzi, D. Hydrodynamic Force Measurements under Precisely Controlled

Conditions: Correlation of Slip Parameters with the Mean Free Path. *Phys. Fluids* **2013**, *25*, 042103.
(10) Honig, C. D. F.; Sader, J. E.; Mulvaney, P.; Ducker, W. A. Lubrication Forces in Air and Accommodation Coefficient Measured by a Thermal Damping Method Using an Atomic Force Microscope. *Phys. Rev. E* **2010**, *81*, 056305.
(11) Seo, D.; Mastropietro, D.; Ducker, W. A. Gas Flows near Solids Coated with Thin Water Films. *J. Phys. Chem. C* **2013**, *117*, 6235−44.
(12) Mahaffy, P. R.; Webster, C. R.; Atreya, S. K.; Franz, H.; Wong, M.; Conrad, P. G.; Harpold, D.; Jones, J. J.; Leshin, L. A.; Manning, H.; et al. Abundance and Isotopic Composition of Gases in the Martian Atmosphere from the Curiosity Rover. *Science* **2013**, *341*, 263−66.
(13) Maxwell, J. C. On Stresses in Rarefied Gases Arising from Inequalities of Temperature. *Philos. Trans. R. Soc.* **1879**, *170*, 231−56.
(14) Karniadakis, G.; Beşkök, A. *Micro Flows: Fundamentals and Simulation*; Springer: New York, 2002.
(15) Lilley, C. R.; Sader, J. E. Velocity Profile in the Knudsen Layer According to the Boltzmann Equation. *Proc. R. Soc. London, Ser. A* **2008**, *464*, 2015−35.
(16) Barber, R. W.; Emerson, D. R. Challenges in Modeling Gas-Phase Flow in Microchannels: From Slip to Transition. *Heat Transfer Eng.* **2006**, *27*, 3−12.
(17) Arkilic, E. B.; Breuer, K. S.; Schmidt, M. A. Mass Flow and Tangential Momentum Accommodation in Silicon Micromachined Channels. *J. Fluid Mech.* **2001**, *437*, 29−43.
(18) Colin, S.; Lalonde, P.; Caen, R. Validation of a Second-Order Slip Flow Model in Rectangular Microchannels. *Heat Transfer Eng.* **2004**, *25*, 23−30.
(19) Yamaguchi, H.; Hanawa, T.; Yamamoto, O.; Matsuda, Y.; Egami, Y.; Niimi, T. Experimental Measurement on Tangential Momentum Accommodation Coefficient in a Single Microtube. *Microfluid. Nanofluid.* **2011**, *11*, 57−64.
(20) Hsieh, S.-S.; Tsai, H.-H.; Lin, C.-Y.; Huang, C.-F.; Chien, C.-M. Gas Flow in a Long Microchannel. *Int. J. Heat Mass Transfer* **2004**, *47*, 3877−87.
(21) Cooper, S. M.; Cruden, B. A.; Meyyappan, M.; Raju, R.; Roy, S. Gas Transport Characteristics through a Carbon Nanotubule. *Nano Lett.* **2003**, *4*, 377−81.
(22) Seo, D.; Ducker, W. A. In Situ Control of Gas Flow by Modification of Gas-Solid Interactions. *Phys. Rev. Lett.* **2013**, *111*, 174502.
(23) Seo, D.; Ducker, W. A. Control of Gas Flow in Narrow Channels Using an Electric Field to Modify the Flow Boundary Condition. *J. Phys. Chem. C* **2014**, *118*, 7480−7488.
(24) Marsh, E. R.; Arneson, D. A.; Liebers, M. J.; Olson, M. W. Effects of Gas Composition on Asynchronous Error Motion in Externally Pressurized Spindles. *Precis. Eng.* **2008**, *32*, 143−47.
(25) Haynes, W. M. *CRC Handbook of Chemistry and Physics*; CRC Press: Boca Raton, FL, 2013.
(26) Perrier, P.; Graur, I. A.; Ewart, T.; Meolans, J. G. Mass Flow Rate Measurements in Microtubes: From Hydrodynamic to near Free Molecular Regime. *Phys. Fluids* **2011**, *23*, 042004.
(27) Ewart, T.; Perrier, P.; Graur, I.; Meolans, J. G. Tangential Momemtum Accommodation in Microtube. *Microfluid. Nanofluid.* **2007**, *3*, 689−95.
(28) Graur, I. A.; Perrier, P.; Ghozlani, W.; Meolans, J. G. Measurements of Tangential Momentum Accommodation Coefficient for Various Gases in Plane Microchannel. *Phys. Fluids* **2009**, *21*, 102004.
(29) Agrawal, A.; Prabhu, S. V. Survey on Measurement of Tangential Momentum Accommodation Coefficient. *J. Vac. Sci. Technol., A* **2008**, *26*, 634−45.
(30) Maurer, J.; Tabeling, P.; Joseph, P.; Willaime, H. Second-Order Slip Laws in Microchannels for Helium and Nitrogen. *Phys. Fluids* **2003**, *15*, 2613−21.
(31) Vinogradova, O. I. Drainage of a Thin Liquid-Film Confined between Hydrophobic Surfaces. *Langmuir* **1995**, *11*, 2213−20.
(32) Ducker, W. A.; Senden, T. J.; Pashley, R. M. Direct Measurement of Colloidal Forces Using an Atomic Force Microscope. *Nature* **1991**, *353*, 239−41.
(33) Ducker, W. A.; Cook, R. F. Rapid Measurement of Static and Dynamic Surface Forces. *Appl. Phys. Lett.* **1990**, *56*, 2408−10.
(34) Ducker, W. A.; Senden, T. J.; Pashley, R. M. Measurement of Forces in Liquids Using a Force Microscope. *Langmuir* **1992**, *8*, 1831−36.
(35) Hutter, J. L.; Bechhoefer, J. Calibration of Atomic-Force Microscope Tips. *Rev. Sci. Instrum.* **1993**, *64*, 1868−73.
(36) Atkins, P. W.; De Paula, J. *Physical Chemistry*; W.H. Freeman: New York, 2010.
(37) Hadjiconstantinou, N. G. The Limits of Navier-Stokes Theory and Kinetic Extensions for Describing Small-Scale Gaseous Hydrodynamics. *Phys. Fluids* **2006**, *18*.
(38) Bowles, A. P.; Ducker, W. A. Gas Flow near a Smooth Plate. *Phys. Rev. E* **2011**, *83*, 056328.
(39) Bird, R. B.; Stewart, W. E.; Lightfoot, E. N. *Transport Phenomena*; J. Wiley: New York, 2002.
(40) Fredriksson, H.; Akerlind, U. *Physics of Functional Materials*; John Wiley & Sons: Chichester, 2008.

Chapter 6. In situ Control of Boundary Condition with Temperature

I would say the works present in this chapter and the next are the paramount of my research. Unlike my previous work presented so far, and other work from other researchers, I found a way to control boundary condition *in situ*. TMAC is usually determined by the system: the condition of solid surface, composition and species of fluid molecules, temperature and pressure, and so forth. Even though everything is set, boundary condition can be controlled from external stimuli. This concept can possibly be used for fluid control.

In Situ Control of Gas Flow by Modification of Gas-Solid Interactions

Dongjin Seo and William A. Ducker*

Department of Chemical Engineering, Virginia Tech, Blacksburg, Virginia 24061, USA

(Received 24 June 2013; published 25 October 2013)

The boundary condition for gas flow at the solid-gas interface can be altered by *in situ* control of the state of a thin film adsorbed to the solid. A monolayer of ocatadecyltrichlorosilane (OTS) reversibly undergoes a meltinglike transition. When the temperature of an OTS-coated particle and plate is moved through the range of OTS ''melting'' temperatures, there is a change in the lubrication force between the particle and plate in 1 atm of nitrogen gas. This change is interpreted in terms of a change in the flow of gas mediated by the slip length and tangential momentum accommodation coefficient (TMAC). There is a minimum in slip length (290 nm) at 18 °C, which corresponds to a maximum in TMAC (0.44). The slip length increases to 590 nm at 40 °C which corresponds to a TMAC of 0.25. We attribute the decrease in TMAC with increasing temperature to a decrease in roughness of the monolayer on melting, which allows a higher fraction of specular gas reflections, thereby conserving tangential gas momentum. The importance of this work is that it demonstrates the ability to control gas flow simply by altering the interface for fixed geometry and gas properties.

DOI: 10.1103/PhysRevLett.111.174502 PACS numbers: 47.85.mf, 34.35.+a, 47.45.−n, 47.45.Gx

Gas flows are usually calculated from the known geometry of the container, the properties of the gas, and the known or assumed boundary conditions. If the boundary condition becomes a variable that could be user controlled, then it is possible to alter gas flow in applications such as flow control in small radius tubes or perhaps flight control for very small objects, for a constant geometry and gas conditions. In this Letter we demonstrate *in situ* reversible control of gas flow in a narrow channel by changing the state of a film adsorbed to a solid surface. Our demonstration uses a chemically adsorbed monolayer of octadecyltrichlorosilane (OTS) on smooth glass. The hydrocarbon octadecane melts at about 28 °C [1]. OTS is similar to octadecane but can be covalently tethered to silica. When tethered, it undergoes a transition akin to melting whereby there is an increase in the ratio of gauche:trans conformations over a temperature range of 0–100 °C [2–4]. By ''melting'' an OTS film, we aim to change the conservation of gas tangential momentum when gas molecules collide with the surface, and therefore to alter the flow of gas. The importance of the conformational change is that the high temperature ''liquid'' form is expected to be smoother, thereby promoting specular reflection. The high temperature form may also be less stiff, which would decrease the fraction of momentum conserved by the gas.

Temperature-induced melting is a rather clumsy method of control, but we believe that this is the first demonstration of stimulus-response surface controlled flow, and shows the route for more elegant systems such as electrical field- or light-activated flow control.

For macroscopic systems, it is usually accurate to assume the no-slip boundary condition at the gas-solid interface. This assumption has diminishing accuracy at high Knudsen number, $\mathrm{Kn} = \lambda/l$, where λ is mean free path, and l is characteristic length of the system, i.e., at low pressure or for thin gas films. Applications at atmospheric pressure include micro-electro-mechanical systems and nano-electro-mechanical systems [5], as well as lab-on-a-chip systems. Kn in the range of 0.1–0.001 is usually described as the slip-flow regime [6–8], where partial slip occurs. The magnitude of partial slip b was described by Maxwell in terms of a tangential momentum accommodation coefficient (TMAC), σ [9]:

$$b = \lambda\left(\frac{2}{\sigma} - \sigma\right). \tag{1}$$

If a surface accommodates all the tangential momentum from a colliding gas molecule then $\sigma = 1$, giving the minimum slip length of $b = \lambda$. If all the gas tangential momentum is conserved, then $\sigma = 0$, and $b = \infty$. Since Maxwell, many refinements of Eq. (1) have been suggested [5,10]; it is important to note that in this Letter, these refinements will affect our measured values of σ, but not our conclusions [11].

Recent work has shown that gas flows can be measured using atomic force microscopy (AFM) [12] colloid probe measurements [13,14]. Laurent *et al.* [15] used lubrication measurements to show a dramatic increase in fitted slip length at low pressure, as expected from Eq. (1). Using similar AFM measurements, Lissandrello *et al.* [16] examined damping over a range of low pressures, and developed a scaling function to describe damping in terms of mean free path, radius, separation, and the viscous boundary layer thickness. Honig *et al.* [17] showed that adding a molecularly thin film of silane to glass caused a decrease in σ. Seo *et al.* [18] showed that the formation of water films on a glass solid alters σ at 1 atm of N_2. For example, the TMAC on equilibrium water films at 10% relative

humidity (RH) are greater than at 0% humidity, and the TMAC is lower at 88% RH. These two demonstrations of altering the TMAC by addition of a film suggest the possibility of altering the TMAC *in situ* by manipulating the properties of a film. This is the objective of the current work. Accommodation coefficients for various gases have also been determined by measuring the gas flow and pressure difference along microchannels. These measurements often find accommodation coefficients of about 0.85 on silicalike materials [19,20] which is greater than the values reported in this Letter. The difference is that the solids considered here are much smoother and the humidity is kept at 0% RH.

The flow of gas in thin films was determined by the indirect method of measuring the lubrication force between a glass sphere (radius, $r \sim 15$ μm) and a flat glass plate, using the AFM colloid probe technique [18]. In short, both the sphere and the plate were cleaned in oxygen plasma, coated with OTS monolayer in hexadecane solution, and then sonicated in toluene to remove any impurities. The sphere and plate were placed in a sealed chamber; the chamber was purged with dry N_2 at 1 atm. Because previous work showed that the lubrication force was a function of humidity [18], we kept the humidity at 0% with silica gel, as measured by a humidity meter. The temperature was controlled in the range 17–33 °C by changing the temperature of the entire room. The chamber was repurged with N_2 after the temperature was changed, to maintain a pressure of 1 atm, so the experiment is at constant pressure in this range. Above 33 °C, the room was kept at 33 °C and the temperature in the chamber was altered by the use of a small lamp within the chamber; below 17 °C, the chamber was chilled with ice [21].

The clamped end of the cantilever was driven with an amplitude A (about 0.05 nm) at the resonant frequency (about 6 kHz), while the deflection of cantilever z the amplitude of deflection R, and the phase of the cantilever deflection relative to the drive θ were measured using a lock-in amplifier while the plate was driven toward the cantilever. The damping coefficient D was obtained from R and θ as a function of separation, assuming the cantilever executes simple harmonic motion, modeled as

$$m\ddot{z} + D(s)\dot{z} + [k - F'(s)]z = kA\cos(\omega t), \qquad (2)$$

where k is the spring constant, m is the mass, ω is the drive frequency, F' is the stiffness of any material in parallel with the spring, and s is the separation between the sphere and plate. We measure the resonant frequency at infinite separation, $\omega_0(\infty)$, and then drive the cantilever at this frequency at all separations. For a cantilever driven at $\omega_0(\infty)$, the damping is given by [22]

$$D(s) = -\frac{k}{\omega_0(\infty)}\frac{A}{R(s)}\sin\theta(s). \qquad (3)$$

The slip length was determined from $D(s)$ using [23],

$$D_{\mathrm{lub}}(s) = \frac{6\pi\eta r^2}{s} f^*(s, b), \qquad (4)$$

where $D_{\mathrm{lub}}(s) = D(s) - D(\infty)$, η is dynamic viscosity of the nitrogen gas, r is the radius of the sphere, and b is the slip length (assumed identical on both surfaces). f^* is an algebraic expression derived by Vinogradova [23] and written in the form used here in Ref. [18]. The dynamic viscosity is a function of temperature (varying by about 10% at 1 atm in the range 9–42 °C for N_2) and was adjusted accordingly.

The key result of our work is that the accommodation coefficient is a function of the temperature for a single film, as shown in Fig. 1, and thus the accommodation coefficient and slip flow boundary condition can be altered by changing the temperature. Therefore, *in situ* modification of the flow boundary condition is possible, leading to control of flow for a constant geometry and gas type. Since λ is an input in the calculation of σ, we accounted for the linear increase in λ with temperature according to the kinetic theory of gases [24].

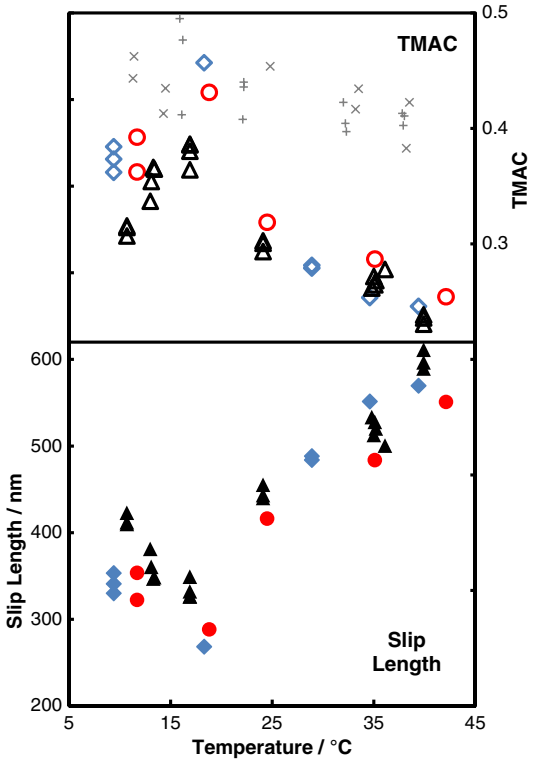

FIG. 1 (color online). Measured TMAC and slip length of 1 atm nitrogen gas on OTS-coated glass. Different symbols represent different sphere-plate pairs prepared by the same method (set 1: diamonds, set 2: circles, set 3: triangles). The slip length data in the bottom pane were used to calculate the accommodation coefficients for the same sphere-plate pair in the top pane. + and × symbols show the TMAC for two sets of *bare* glass surfaces.

In detail, there is a maximum in TMAC of ≈ 0.44 at 18 °C. TMAC decreases to 0.25 at 42 °C, and ≈ 0.3 at 9 °C. There is a systematic relative uncertainty of about 3% in all fitted slip lengths that arises from error in the radius and spring constant. This propagates into an uncertainty of about 3% in the TMAC. There is an additional relative uncertainty of 3% in each separate measurement of slip length, which propagates into ~3% in the TMAC. For each sample, we repeated measurements at the same temperature (see Fig. 1) and the average variability in repeat measurements was about ± 11 nm, or 0.01 in TMAC, which is much smaller than the overall temperature-induced decrease in TMAC of about 0.2. Note that the adjustments for the variation in viscosity and λ with temperature are much smaller than the effects in Fig. 1. Changes in TMAC for bare glass surfaces (no film) over the same temperature range were very slight, as shown in the top part of Fig. 1.

Figure 1 shows results from three sphere-plate pairs. There is a significant variation from pair to pair, but all pairs show the same overall trend with a maximum in the TMAC at about 18 °C. This variation in TMAC is mainly attributed to slight variation in sample preparation. Note also that very similar results are obtained when measuring the TMAC at the same temperature twice, but with several different temperatures in between; i.e., the TMAC can be changed reversibly on the same film.

We now examine hypotheses to explain the measured variation in TMAC. The first hypothesis is that the OTS film becomes less rough with increased temperature, and that this causes a smaller fraction of gas molecules to experience a change in the tangential component of velocity after colliding with the solid. This loss of roughness may be due to loss of crystalline patches of OTS chains during melting. To test this hypothesis, we have measured the roughness of two OTS films as a function of temperature using AFM tapping mode (MFP-3D, Asylum Research; ORC-8 Cantilever A, Bruker), a peltier device to alter the temperature and a glove bag purged with dry air to control the humidity. Fig. 2 shows the measured root mean squared (rms) roughness of two OTS-coated glass plates, measured over an area of $(10\ \mu\text{m})^2$, which enables us to measure roughness on a lateral scale of about 40 nm. We make two observations. First, the rms roughness is of the same order as a nitrogen molecule radius, ~250 pm [24], so the roughness has been changed on a scale that is likely to affect molecular collisions. Second, both plates show a monotonic decrease in rms roughness from about 800 to 50 pm in the temperature range 16 to 41 °C, which is consistent with earlier observations of a more liquidlike conformation distribution at higher temperature. Thus the measured decrease in accommodation coefficient at temperatures above 18 °C is correlated with a decrease in roughness.

The measured decrease in roughness does not explain the decrease in TMAC that occurs below 18 °C. Our hypothesis is that the film stiffness experienced by the nitrogen molecule also decreases with increasing temperature when the chains melt. The decrease in film stiffness leads to an increase in the accommodation coefficient. We cannot examine the stiffness on the scale of a nitrogen molecule, but we can examine the overall stiffness on the scale of the sphere, which should depend on the local stiffness.

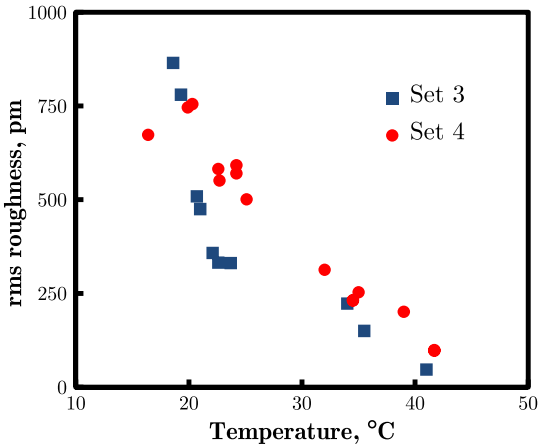

FIG. 2 (color online). rms roughness of two OTS-coated glass surfaces as a function of temperature.

The stiffness of the film was determined by measuring the amplitude and phase of the cantilever driven at $\omega_0(\infty)$ after the sphere makes contact with the solid. In the simple harmonic oscillator model, any spring in parallel to the cantilever has a force gradient (stiffness) given by [22]

$$F'(s) = -\frac{kA}{R(s)}\cos\theta(s). \tag{5}$$

We are interested in the stiffness of the film, which we determined from R and θ immediately after initial contact of the plate. This contact can be identified by a sudden jump in the deflection signal followed by a steep repulsion. Our interest lies in the region -0.5 to 0 nm, where the film is gently compressed. The low load limit is of interest because the film is lightly loaded during the lubrication experiment. The data are noisy, but there is a trend to a stiffer film at lower temperature [Fig. 3(b)], and, in particular, an increase in stiffness between 19 and 12 °C. Thus, the small decrease in accommodation coefficient (increased conservation of gas momentum in the tangential direction) when the temperature drops from 19 and 12 °C correlates with an increase in stiffness of the film.

So far we have elucidated two trends for the OTS film as a function of temperature: the film becomes less rough and less stiff as temperature increases. We expect these two properties of the film have opposite effects on TMAC, which could lead to a maximum. The question now is why they should each control the TMAC in different regimes. Our simple idea is that increases in roughness only affect TMAC up to a certain magnitude of roughness. First, we point out that our AFM cannot be cooled, so only have roughness data at temperatures greater than 16–18 °C, and

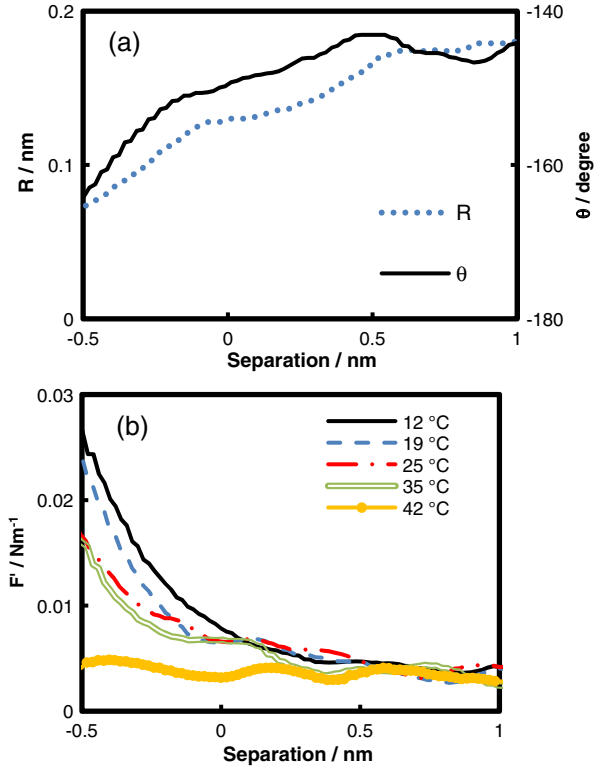

FIG. 3 (color online). Stiffness of OTS film, F', with probe in contact. (a) R (left vertical axis), and θ (right vertical axis) used to calculate stiffness at 25 °C. The lock-in amplifier time constant of 10 ms leads to data averaging of the R and θ over a distance of 0.2 nm in this figure. (b) Stiffness as a function of temperature, calculated using Eq. (5).

it is not clear that the film is increasing in roughness below 18 °C. Also, once the film is fully crystallized, there is no clear mechanism for further roughening. Even if the film were to become rougher, it is not clear that this would continue to affect TMAC indefinitely because we expect roughness on a scale much greater than the nitrogen molecule radius (~ 250 pm) to have a diminishing effect. From Fig. 2 we see that the film roughness has grown to three molecular radii at 18 °C, and there may be no further effect of roughness at that point.

Our final question is on the magnitude of flow changes that can occur by changing the flow boundary condition. We calculated the volume rate of flow $\dot{V}$ through a cylindrical tube with the assumptions of the Hagen-Poiseuille equation, except that partial slip is allowed. This example illustrates flow through a pore in a membrane. Ignoring the pressure dependence of the slip length via the mean free path [Eq. (1)]:

$$\dot{V}(b) = \frac{\pi(P_0 - P_L)R_T^4}{8\mu L}\left(1 + \frac{4b}{R_T}\right), \tag{6}$$

where P_0 is the inlet pressure, P_L is the outlet pressure, R_T is the radius of the tube, and L is the length of the tube. For a given pressure drop, length of tube, radius, and viscosity

$$\frac{\dot{V}(b_1)}{\dot{V}(b_2)} = \frac{(R_T + 4b_1)}{(R_T + 4b_2)}, \tag{7}$$

where b_1 and b_2 represent the slip lengths on two different surfaces. For example, assuming b_1 has the same slip length as OTS at 40 °C (600 nm) and b_2 has the same slip length as OTS at 18 °C (290 nm), and a tube radius of 1000 nm, the volumetric flow increases by about 50%. If we account for the variation in b is a function of pressure along the tube, and the TMAC is assumed independent of pressure, the flow increases by about 45%. Thus the changes in slip length observed in this Letter will cause significant changes in flow through a microscopic cylinder.

In summary, we conclude from this work that the slip length at the solid-gas interface can be altered *in situ* when a responsive surface film is added to a glass solid. In this case, we cause the response for N_2 at 1 atm by changing the temperature. After accounting for the small effect of temperature on the mean free path, we also show that the tangential momentum accommodation coefficient can be altered *in situ* by changing the temperature. We attribute the main changes in accommodation coefficient to changes in surface roughness that are produced in the film by temperature changes. The properties of surface films can also be changed by other stimuli, so changes in tangential accommodation and concomitant flow rates should also be affected by a variety of stimuli such as light or electric fields. The magnitudes of changes in flow are significant for channels with dimensions on the order of 1 μm in size.

The importance of this work is that it demonstrates the ability to control gas flow even for fixed geometry and gas properties. It is the first demonstration of a physical principal that could be used for applications such as controlling the flight of miniature or very high altitude aircraft simply by altering the resistance on selected parts of the aircraft, or for throttling the flow through a microfluidic device without the use of any moving parts.

This research was funded by the National Science Foundation via Grant No. CBET-0959228. The authors also thank Dean Mastropietro for assistance with the AFM equipment. We thank Professor John Morris, Virginia Tech, for useful discussions.

*To whom all correspondence should be addressed.
wducker@vt.edu

[1] *Handbook of Chemistry and Physics*, edited by W. M. Haynes (CRC Press, Boca Raton, 2013), 94th ed.
[2] R. W. Wang, J. Guo, G. Baran, and S. L. Wunder, Langmuir **16**, 568 (2000).
[3] M. Ho and J. E. Pemberton, Anal. Chem. **70**, 4915 (1998).
[4] R. G. Nuzzo, E. M. Korenic, and L. H. Dubois, J. Chem. Phys. **93**, 767 (1990).
[5] G. Karniadakis, A. Beskok, and N. Aluru, *Microflows and Nanoflows* (Springer-Verlag, New York, 2005).

[6] A. Frangi, G. Spinola, and B. Vigna, Int. J. Numer. Methods Eng. **68**, 1031 (2006).
[7] C. D. F. Honig, J. E. Sader, P. Mulvaney, and W. A. Ducker, Phys. Rev. E **81**, 056305 (2010).
[8] F. Ezquerra Larrodé, C. Housiadas, and Y. Drossinos, Int. J. Heat Mass Transfer **43**, 2669 (2000).
[9] J. C. Maxwell, Philos. Trans. R. Soc. London **170**, 231 (1879).
[10] C. R. Lilley and J. E. Sader, Proc. R. Soc. A **464**, 2015 (2008).
[11] For nitrogen gas at 1 atm and the slip length in the range 300–1000 nm, the TMAC calculated using Maxwell's equation is systematically about 5% greater than when calculated using Lilley and Sader's equation.
[12] G. Binnig, C. F. Quate, and C. Gerber, Phys. Rev. Lett. **56**, 930 (1986).
[13] W. A. Ducker, T. J. Senden, and R. M. Pashley, Nature (London) **353**, 239 (1991).
[14] C. D. F. Honig, J. E. Sader, P. Mulvaney, and W. A. Ducker, Phys. Rev. E **81**, 056305 (2010).
[15] J. Laurent, A. Drezet, H. Sellier, J. Chevrier, and S. Huant, Phys. Rev. Lett. **107**, 164501 (2011).
[16] C. Lissandrello, V. Yakhot, and K. L. Ekinci, Phys. Rev. Lett. **108**, 084501 (2012).
[17] C. D. F. Honig and W. A. Ducker, J. Phys. Chem. C **114**, 20 114 (2010).
[18] D. Seo, D. Mastropietro, and W. A. Ducker, J. Phys. Chem. C **117**, 6235 (2013).
[19] E. B. Arkilic, K. S. Breuer, and M. A. Schmidt, J. Fluid Mech. **437**, 29 (2001).
[20] J. Maurer, P. Tabeling, P. Joseph, and H. Willaime, Phys. Fluids **15**, 2613 (2003).
[21] Between 33 °C and 41 °C, and between 17 °C and 11 °C the pressure was not equilibrated with the atmosphere, so the pressure will be about 2.5% greater at 41 °C and 2.7% lower than 1 atm due to the increase or decrease in termperature. This change in pressure due to heating or cooling at constant volume does not change the mean free path.
[22] W. A. Ducker and R. F. Cook, Appl. Phys. Lett. **56**, 2408 (1990).
[23] O. I. Vinogradova, Langmuir **11**, 2213 (1995).
[24] P. W. Atkins, *Physical Chemistry* (Oxford University Press, Oxford, 1994), estimated from the van der Waals constant in Table 1.5.

Chapter 7. In situ Control of Boundary Condition with Electric Field

Though the method of controlling boundary condition is presented in the previous chapter, manipulating temperature of whole system is still inconvenient. Thus, I propose using electric field at low potential difference in the order of several volt or lower to control boundary condition. It was done by manipulating the surface molecules which respond to electric field. This idea can further be used to the concept of micro- and nano-machining.

In the previous chapter as well as in this chapter, I claimed the roughness controls TMAC. I made this claim more affirmative by presenting a mathematical explanation.

THE JOURNAL OF PHYSICAL CHEMISTRY C

Article

pubs.acs.org/JPCC

Control of Gas Flow in Narrow Channels Using an Electric Field To Modify the Flow Boundary Condition

Dongjin Seo and William A. Ducker*

Department of Chemical Engineering, Virginia Tech, Blacksburg, Virginia 24061, United States

ABSTRACT: We demonstrate that the resistance to the flow of gas in a narrow channel can be controlled *in situ* by using an electric field to modify a thin organic surface film. The flow was determined indirectly by measurement of the lubrication forces between a glass sphere and a gold-coated plate. The plate was coated with a self-assembled monolayer of ω-COOH thiol. Application of the field to the ω-COOH plate caused a large decrease in lubrication force whereas application of the field to a ω-CH_3 plate did not. The lubrication force reverts back to the no-field value when the field is removed. We show that the field causes a larger decrease in the roughness of the ω-COOH plate compared to the ω-CH_3 plate. The observed correlation between a decrease in lubrication force and roughness suggests that the mechanism for increasing the flow is decreasing the surface roughness: the roughness affects the tangential momentum accommodation coefficient, which in turn affects the boundary condition for gas flow at the solid. The proposed mechanism for the change in roughness is that the field applies a torque to the dipole on the ω-COOH group, causing a change in average tilt, which decreases the roughness. This research demonstrates a simple alternative method to mechanical valves in microscopic devices: gas flow is controlled *in situ* by molecular scale changes to the wall.

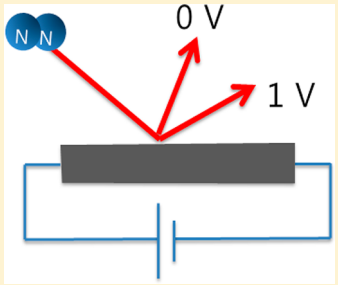

INTRODUCTION

The volumetric flow rate of a simple Newtonian fluid in a tube depends not only on the pressure drop between the ends of the tube, the fluid viscosity, the cross section, and length of the tube but also on the boundary condition at the fluid−solid interface. For everyday macroscopic systems, experience tells us that the boundary condition is fixed for a particular combination of phases: there is no-slip at the fluid−solid interface. Thus, the available methods of reducing the flow are to reduce the pressure difference or to diminish the cross section of the tube (e.g., close a mechanical valve). However, when the characteristic length scale of the system is similar to the mean free path of the fluid, λ, the boundary condition is material-dependent. Such a flow can be controlled, in principle, by changing the boundary condition. Boundary-mediated control of flow was recently demonstrated by altering the temperature of an adsorbed monolayer,[1] but we expect such control to have limited application because the temperature is often set for another reason or difficult to change. The objective of this paper is to describe a realization of boundary-mediated flow control using an electric field. Electric fields are a much more practical means of controlling gas flows than temperature because of (a) facile integration into electronic control systems, (b) relatively rapid switching, and (c) the ability to pattern electrodes.

The Knudsen number is a useful parameter for determining when boundary conditions are important for flow. The Knudsen number is the ratio of the mean free path of fluid, λ, to the characteristic dimension of system, L:[2−4]

$$Kn = \frac{\lambda}{L} \tag{1}$$

When Kn is smaller than about 0.001, the details of the collision between the gas molecule and the solid affect such a small portion of the flow that assumption of no slip boundary condition is usually sufficiently accurate to calculate the flow. For $0.001 < Kn < 0.1$, also known as the slip flow regime, the boundary condition can be modeled using a partial slip boundary condition.[2] In practice, the equations for flow are similar to the continuum equations but with an extra parameter, the slip length, to describe the interaction of the gas with the solid. A positive slip length increases the effective cross section of a tube. For larger values of Kn, the continuum picture fails and the molecular nature of the gas must be considered when calculating the flow.

The microscopic explanation for changes in the boundary condition is that slip length depends on the fraction of tangential momentum conserved in a gas−solid collisions. If all the tangential momentum is conserved, then the full-slip boundary condition applies. As a greater fraction of tangential momentum is lost, the slip length decreases. This concept is parametrized by the tangential momentum accommodation coefficient (TMAC), σ:[2]

$$\sigma = \frac{\text{change in tangential momentum}}{\text{initial tangential momentum}} \tag{2}$$

where $\sigma = 1$ represents zero average tangential momentum after the collision and $\sigma = 0$ represents conservation of tangential momentum. In general, the tangential momentum is difficult to

Received: January 17, 2014
Revised: March 13, 2014
Published: March 14, 2014

calculate and can in principle be affected by the roughness of the surface, the elasticity of collisions, and the relative masses, bonding, and arrangement of the atoms. Accommodation coefficients have been measured by a variety of researchers (e.g., refs 5−10), and theoretical aspects are described in two reviews.[2,3]

The mean free path of nitrogen at 1 atm is about 70 nm, so at 1 atm interactions with the solid walls start to affect the flow when the flow dimensions are smaller than about 70 μm. Thus, boundary-mediated control of flow can be implemented, in principle, for small devices such on lab-on-a-chip, microelectromechanical (MEMS), and nanoelectromechanical systems (NEMS).[2] The mean free path is inversely proportional to the pressure (at constant temperature) so boundary-mediated flow control can also be implemented, in principle, for macroscopic applications at low pressures, such as the reentry of spacecraft or flight in the Martian atmosphere. For example, the Knudsen number is 0.001 for a 0.7 m flow in 10^{-4} atm of N_2.

Here we describe flow boundary control using an electric field. Many previous applications of electrically responsive materials have been described, for example, electronic displays[11] and drug delivery.[12,13] To implement flow boundary control, we begin with a smooth solid where the slip length is sensitive to the film structure. In contrast, a rough solid will give the minimum slip, and the small modification caused by the field may have no measurable effect. We then attach a self-assembled monolayer of 16-mercaptohexadecanoic acid to the gold. The ω-COOH group was chosen so that the electric field might apply a significant torque at the unattached dipolar end of the molecule, thereby causing a change in the monolayer properties.

The effect of the surface on the flow is determined indirectly in this work by measuring the damping on a sphere that is in close proximity to a plate.[9,14−16] The principles of measurement are described below in the Theory section. In earlier work from our group,[1] the boundary condition was controlled through modification of an adsorbed layer of octadecyltrichlorosilane (OTS). The conformation of OTS is a function of temperature: it melts at higher temperature, giving a smoother surface, which decreases the resistance to flow. This was observed as a decrease in damping of the sphere, which can be explained in terms of a greater slip length as described by Vinogradova.[17]

THEORY

The damping force on a sphere near a plate is larger than for a free sphere because of the confinement of the fluid in the thin film between the sphere and plate, as described by Brenner[18] for the no-slip condition and Vinogradova[17] for a partial-slip condition. In our experiments the sphere is attached to an atomic force microscope (AFM) cantilever, which also contributes to the damping. However, the effect of the cantilever on the additional force due to confinement is small because the cantilever is much further than the sphere from the plate. The extra damping due to the proximity of the sphere to the plate is defined as $D_{lub} = D(h) - D(\infty)$, where h is the separation between the sphere and plate. Several methods have been developed to measure the damping on AFM probes;[19−21] we used a method proposed by Ducker and Cook[20] in which the clamped end of cantilever is oscillated with a piezoelectric crystal, and the motion of the free end is modeled as a forced harmonic oscillator with the following equation of motion:

$$m\ddot{z} + m\gamma(h)\dot{z} + [k - F'(h)]z = kA\cos(\omega t) + C \quad (3)$$

where m is the effective mass of the cantilever, z is the cantilever deflection, γ is the damping coefficient, k is the spring stiffness, F' is the gradient of conservative forces, A is the amplitude, ω is the frequency of oscillation at the clamped end of the cantilever, and C is a constant to account for constant forces. The solution is $z = R\cos(\omega t + \theta)$, where R is the amplitude at the free end of the cantilever and θ is the phase lag relative to the oscillation at the clamped end. A lock-in amplifier is used to measure R and θ as a function of h, which is then used to determine the damping, D. When the driving frequency is equal to the resonance frequency of the cantilever at infinite separation, $\omega_0(\infty)$

$$D(h) = m\gamma(h) = -\frac{k}{\omega_0(\infty)}\frac{A}{R(h)}\sin\theta(h) \quad (4)$$

Details, discussion, and application of this method to measuring damping can be found in previous research.[10]

EXPERIMENTAL SECTION

Solid Substrates. Four different gold surfaces were examined, all of which were prepared from commercial 25 mm by 25 mm gold-coated microscope glass slides (Molecular Engineering Inc.). (1) Clean gold: slides were treated with piranha solution, then rinsed with deionized, charcoal-treated (Millipore) water, and then dried with dry nitrogen. (2) ω-COOH: Clean gold was immersed in 5 mM 16-mercaptohexadecanoic acid (90%, Sigma-Aldrich) in ethanol for 24 h, rinsed with ethanol, and dried with dry nitrogen. (3) ω-CH_3: Clean gold was immersed in 5 mM hexadecanethiol (99%, Sigma-Aldrich) for 24 h, rinsed with ethanol, and dried with dry nitrogen. (4) Flattened ω-COOH: The commercial gold slide was pressed against freshly cleft mica surface using a homemade screw press made from steel with Viton jaws to maintain uniform pressure. While under pressure, these samples were placed in an over at 200 °C for 24 h. After cooling, these samples were treated in the same way as for ω-COOH samples.

The electric field was generated in the plane of the gold though wires attached at opposite edges of the glass slide using electrically conducting glue. A function generator (Wavetek 395) was used to maintain a dc potential across the film. The direction of the electric field is perpendicular to the long axis of the cantilever unless stated otherwise.

A soda lime glass sphere (nominal radius, r = 15 μm) (Duke Standard Cat. No. 9030, Thermo Scientific) was attached to an AFM cantilever (ORC-8 D, Bruker Co. 200 μm × 20 μm) with epoxy glue that was melted and frozen in place. This same sphere was used for all the different gold surfaces. This cantilever−sphere set was cleaned in an O_2 plasma (200 mTorr, 5 min, 100 W).

Lubrication Measurement. The overall geometry is shown schematically in Figure 1. The separation between the glass sphere and the gold plate was altered using a piezoelectric crystal stage (P-753 K082, Physik Instrumente) to which the plate was attached. The deflection of the cantilever was measured using the light lever technique,[22] as described in ref 10, using a laser (681 nm, Schäfter+ Kirchhoff GmbH) and a split photodiode (Phresh Photonic), and recorded by an A/D card (PCI-6110, National Instruments) and Igor Pro 6 software (WaveMetrics).

The clamped end of the cantilever was vibrated using a piezoelectric crystal (PL022.31, Physik Instrumente) with

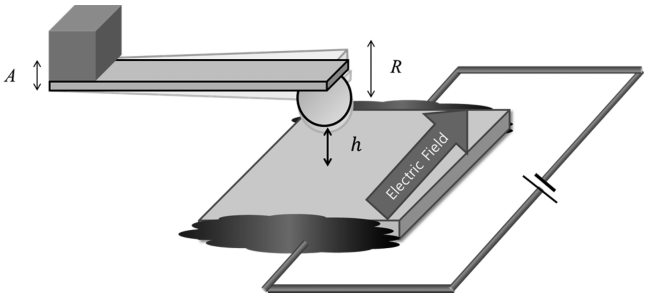

Figure 1. Schematic of the measurement showing the geometry of the field, cantilever, and plate.

amplitude, A, and frequency, ω_0, driven by a lock-in amplifier (SRS830, Stanford Research Systems). The lock-in amplifier was also used to measure R and θ. Typical values were A = 0.1 nm, ω_0 = 6255 Hz, and $R(\infty)$ = 9 nm. The phase angle was set to $-\pi/2$ at the resonant frequency.

The plate and the sphere were exposed to α-particles from a polonium 210 source to reduce the magnitude of static charge, and then the apparatus was enclosed in a vacuum chamber with 100 g of dried silica gel and purged with N_2 gas. All experiments were performed at 1.0 atm, 25 ± 2 °C, and 0% humidity.

RESULTS

Damping Depends on the Applied Field. Equation 4 shows that the damping is proportional to sin θ/R. For the conditions of these experiments, changes in sin θ/R are dominated by R, so if the damping is affected by the field, then changes is R should track the voltage applied to the gold plate. Figure 2 shows that when a ω-COOH plate was positioned

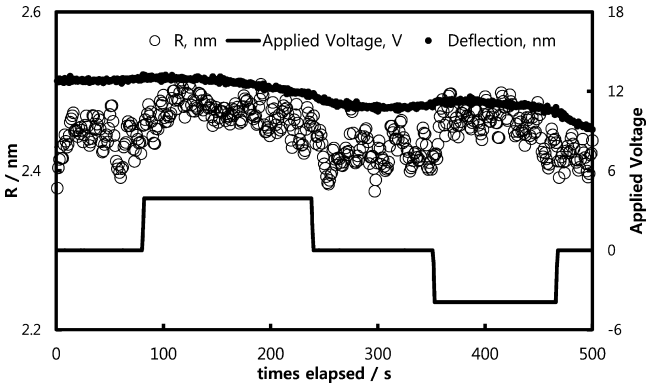

Figure 2. Measured R (open circles) and deflection (closed circles) as a function of time while the voltage across the gold-coated plate was altered (right axis). R increases when a positive or negative potential is applied. The mean distance between the sphere and the plate was about 800 nm. R and the deflection are shown on the same scale (left axis), but there is an arbitrary offset on the deflection.

about 800 nm from the sphere and the cantilever was driven at its resonant frequency, ω_0 = 6239 Hz, R (open circles) increased in response to either a positive or negative applied voltage. This corresponds to a *decrease* in damping; i.e., we have achieved electronic control of the lubrication damping.

The deflection of cantilever has an arbitrary offset, and drifts with time, even with no voltage applied to the film. When the field is applied to the film, there is a small change in deflection (about 1/40 of the change in deflection to cause about 0.1 nm difference in R), showing that there is a very small static (zero frequency) *repulsion* between the sphere and the plate. The use of the lock-in allows us to measure the damping independent of this static repulsion.

A more precise quantification of the damping was obtained by measuring the damping as a function of separation for several types of plates. All further results are presented as D_{lub} obtained using eq 4.

Field Changes the Lubrication Forces by Acting on the Monolayer. First, the effect of the applied field was determined for clean gold plates. Figure 3a shows that the

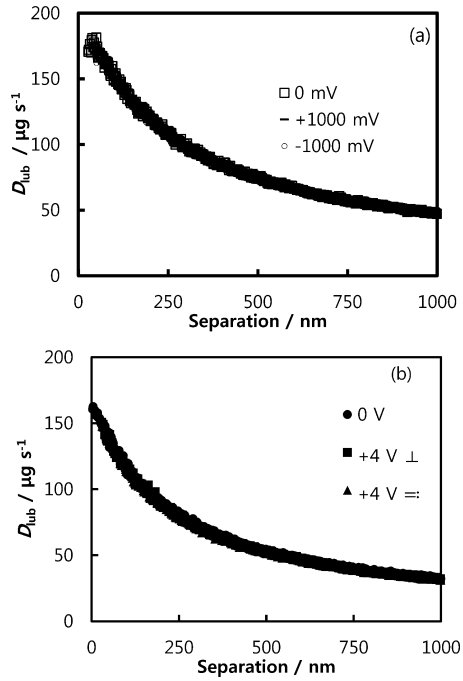

Figure 3. D_{lub} for clean gold. (a) Effect of positive and negative voltage. (b) Effect of direction of field, perpendicular or parallel to the long axis of the cantilever. (Data for various voltages overlay each other.)

applied voltage has no effect on the lubrication force. (The symbols representing the D_{lub} for each of three different voltages overlay each other.) We also examined the effect of rotating the field direction in the plane of the gold such that the field was parallel to the long axis of the cantilever (Figure 3b). A field parallel to the cantilever also has no measurable effect.

Next, the effect of the field was measured on the ω-COOH plates. Figure 4 shows that the application of a field decreases the lubrication force. Because the field had no effect on lubrication for clean gold surfaces, we conclude that the field-induced decrease in the lubrication force shown in Figure 4 is caused by a change to the self-assembled monolayer. We also conclude that the effect of the field saturates between 1 and 2 V. Finally, we note that the magnitude of reduction in D_{lub} is about 25% at small separations. This reduction was achieved by modifying only one solid−gas interface. One might expect a significantly larger effect if both surfaces were modified.

Changes in Lubrication Force Are Correlated with Changes in Surface Roughness. To facilitate comparison of D_{lub} under different applied voltages, we summarize each $D_{lub}(h)$ curve with a single parameter. Ideally, we would like this parameter to have some theoretical meaning, so we experimented with fitting the Vinogradova equation[17] to our

dx.doi.org/10.1021/jp500579b | J. Phys. Chem. C 2014, 118, 7480−7488

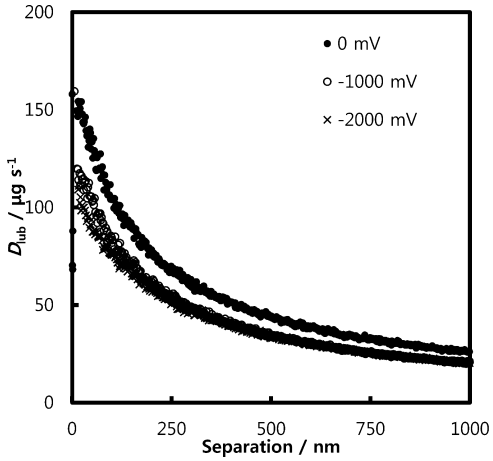

Figure 4. D_{lub} for glass sphere and ω-COOH gold surface. As voltage increases, the lubrication force decreases.

data using the slip length as a free parameter. Although the 0 V curves fit well, the data at 1 V and higher voltages did not. This was inconvenient, but not unexpected, if the slip lengths are a large fraction of the separation or radius of the sphere. So, we parametrized our data using the distance-average value of $D_{lub,\ average}$ in the range 20−1500 nm:

$$D_{lub,average} = \frac{\int D_{lub}(h)\ dh}{\int dh} \quad (5)$$

The range of 20−1500 nm was chosen because smaller separations contains significant errors in analysis and data at greater separations have a high signal-to-noise ratio.

The values of $D_{lub,\ average}$ as a function of applied voltage for three different ω-COOH plates (Figure 5) show that (a) the lubrication force diminishes when the magnitude of the applied voltage is increased. Also, the effect of a positive voltage is the same as for a negative voltage. This is expected for the radially symmetric flow examined here: whichever way the field points in the plane of the gold, the flow is directly partly with, partly against, and partly orthogonal to the field. Figure 5 also shows the measured rms roughness of each of the ω-COOH plates measured with AFM tapping mode (MFP-3D, Asylum Research; ORC-8 Cantilever A, Bruker Corporation). The image size was 10 μm by 10 μm with 1024 × 1024 pixels such that the smallest pixel has a length of about 10 nm. In all three sets, the trends for $D_{lub,\ average}$ and rms roughness are the same, suggesting that the decrease in $D_{lub,\ average}$ is caused by the decrease in roughness of the surfaces. The van der Waals radius of nitrogen molecule is 250 pm, so the observed change in roughness of 1 nm has the appropriate magnitude to affect a collision with a nitrogen molecule.

Field-Induced Changes in Lubrication Are Smaller for Smoother Films. If the field were affecting the lubrication force by causing a reduction in surface roughness, then one would expect that there might exist a sufficiently smooth surface at zero applied voltage such that application of a voltage would make no difference to the lubrication force. To test this hypothesis, we created smoothed gold surfaces, as described in the Experimental Section. Since we hypothesize that the roughness change is effected through the thiol monolayer, which is about 2 nm in thickness,[23] we created gold films with a with a roughness of <2 nm. The results of lubrication and roughness measurements on smoothed ω-COOH plates are

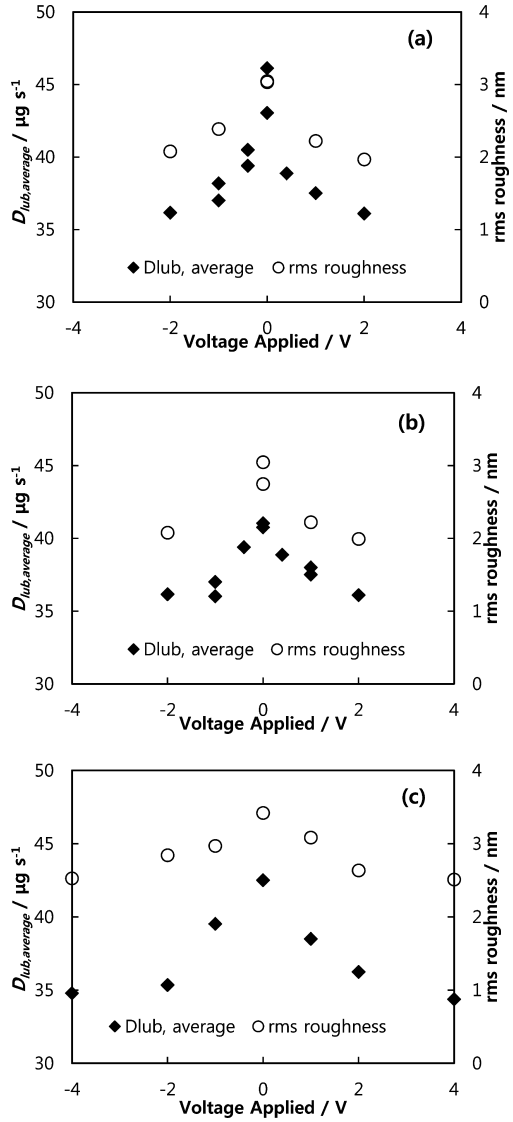

Figure 5. $D_{lub,average}$ and rms roughness over 10 μm measured as a function of voltage applied in the plane of the ω-COOH plate. The three panes show data from three different plates, all of which show the same trend as the magnitude of voltage increases: the damping and roughness decrease.

shown in Figure 6. The changes in roughness and the changes in lubrication force on application of the field are clearly smaller than for the ω-COOH plates that were not smoothed, which is consistent with the idea that changes in roughness are the mechanism for changes in lubrication force: if the films are already sufficiently smooth, the field has little effect.

Field-Induced Changes in Lubrication Are Smaller for an ω-CH_3 Monolayer. Our original hypothesis was that alterations to the film could be effected via application of an electrostatic force to the molecules in the self-assembled monolayer. To obtain a large force on the molecules, we fabricated the monolayer from a molecule containing a dipolar ω-group (COOH). To examine the effect of the polarity of the ω-group, measurements were repeated for a ω-CH_3 monolayer.

Figure 7 shows that the electric field causes little or no change in damping when the gold is coated in the ω-CH_3 film. The large change in lubrication for the dipolar ω-COOH film compared to the small change in nonpolar ω-CH_3 film is

dx.doi.org/10.1021/jp500579b | J. Phys. Chem. C 2014, 118, 7480−7488

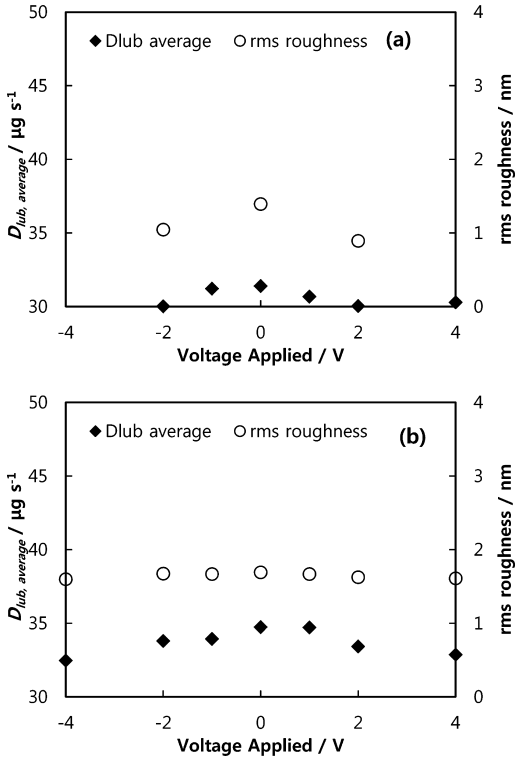

Figure 6. $D_{lub,average}$ and rms roughness as a function of applied voltage for flattened gold films coated in a ω-COOH monolayer displayed on the same scale as the data for rougher surfaces shown in Figure 5. The changes in $D_{lub,average}$ and rms roughness are much smaller for the flattened gold. (a) and (b) show results from two different flattened gold films.

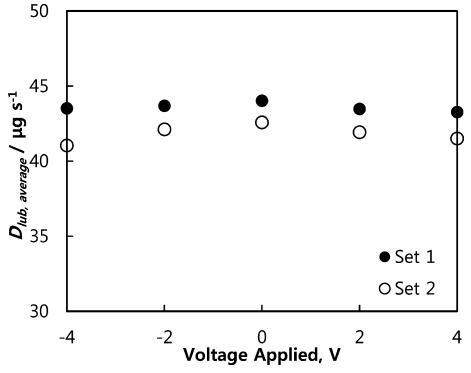

Figure 7. $D_{lub,average}$ as a function of voltage for ω-CH_3 films. The variation in $D_{lub,average}$ is much smaller than for the ω-COOH films shown in Figure 5.

consistent with the hypothesis that the changes in roughness and lubrication forces are caused by the field acting on the thin organic film and probably acting on the ω-COOH group.

Correlations between $D_{lub,average}$ and Plate Roughness. Without a detailed molecular investigation, it is difficult to determine the exact mechanism of how the field alters the organic monolayer, but *all* our measurements with different factors separately show that when we diminish the roughness, the lubrication force decreases. To show this trend more clearly, we have plotted in Figure 8 the experimental values of $D_{lub,average}$ as a function of rms roughness for all experiments. There is a clear correlation between $D_{lub,average}$ and roughness,

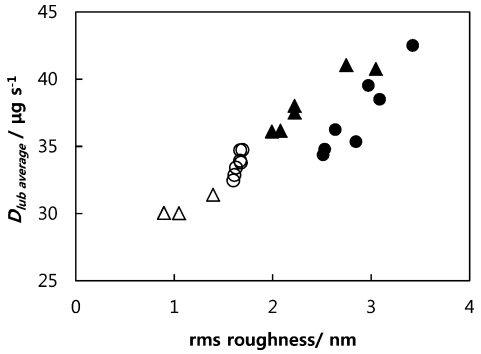

Figure 8. $D_{lub,average}$ plotted against rms roughness for two ω-COOH plates (filled symbols) and two flattened ω-COOH plates (open symbols).

suggesting that rms roughness is an important determinant of the flow boundary condition at the gas−solid interface.

DISCUSSION

Proposed Mechanism for Changes in Lubrication. Our observations that the electric field has no effect in the absence of the thiol suggests that the mechanism for the field-induced change in lubrication operates via the thiol layer. Furthermore, the diminished effect of the ω-CH_3 film compared to the ω-COOH film on the lubrication is consistent with a field applying a torque to the terminus of the monolayer molecules. Considering this evidence, we propose that the field reduces the lubrication force by changing the tilt on the molecules so as to reduce the roughness. The electric field could also be changing the stiffness or elasticity of the surface, but these possibilities will not be considered further in this paper.

Figure 9 is a schematic showing how an increase in tilt angle (relative to the overall surface normal) could diminish the

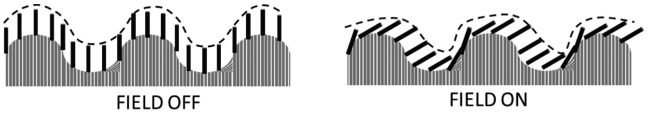

Figure 9. Schematic showing potential mechanism for diminished roughness arising from a change in tilt angle.

magnitude of surface roughness. The measured change in roughness was about 1 nm, whereas the thickness of the unperturbed film is about 2 nm.[23] Considering that in the absence of a field, the molecules are already tilted by an angle of 27°,[24] reducing the roughness by 1 nm would require a significant change in angle. In the absence of a field, the thiols are arranged in domains with the same tilt angle, but the direction is probably random. It is possible that the smoothening effect could also be due to alignment of the tilt angles in the various domains.

Length Scales of Roughness That Affect Momentum Change. In the Results section, we noted that the field induced changes in rms height (~1 nm) were on about the same length scale as the radius of a N_2 molecule (~0.25 nm), but recall that those roughness measurements were obtained with a pixel size of 10 nm, so we were examining roughness on a lateral scale that is much greater than the impinging molecule. Although it is not intuitively obvious that large-scale features should affect the accommodation coefficient, the Appendix shows that it does for the example of a sawtooth surface. An intuitive understanding

dx.doi.org/10.1021/jp500579b | J. Phys. Chem. C 2014, 118, 7480−7488

can be achieved by reference to Figure 10. Compared to molecules striking a horizontal surface, molecules striking a

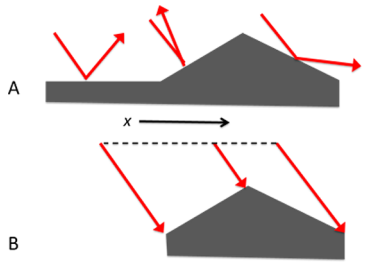

Figure 10. Schematic showing effect of inclined slopes on changes in tangential momentum. (A) Compared to a horizontal surface, a positive slope causes a decrease in *x*-momentum, and a negative slope causes an increase in *x*-momentum. (B) There is a greater range of starting positions from which a molecule traveling from the left can strike the positive slope.

positive slope have a diminished *x*-component of momentum, and molecules striking a negative slope have an increase *x*-component of momentum. However, two factors diminish the effect of the negative slope: (a) there is a diminished chance of the molecules striking the negative slope, and (b) some of the molecules that strike the negatively sloped surface go on to strike the positive slope. Therefore, the effect of the negative slope is smaller, and there is a net decrease in *x*-momentum of the gas caused by collision with this surface. This argument was independent of the lateral distance between the peaks, and therefore we should be considering roughness on both large and small scales.

First we examine the roughness on smaller lateral scales by capturing AFM images with smaller pixel sizes. Figure 11 shows a 1 μm by 1 μm area with 2 nm pixels and a 0.5 μm by 0.5 μm area with 0.5 nm pixels. The best effort was made so that images at different voltages were taken on the same location, but thermal drift forced small changes in location. Even on these smaller-scale images, the rms roughness includes roughness on various length scales. To narrow the lateral-length scale, we processed the images by first taking a two-dimensional fast Fourier transform (2D FFT), deleting length scales greater than a cutoff, performing an inverse fast Fourier transform (2D IFFT), and then measuring the roughness. In this way we are able to show, in Figure 11, the roughness on a 2−3 nm lateral scale (part a) and on a 0.5−2 nm lateral scale (part b). The results show that the voltage causes a change in roughness of about 0.9 nm for scales up to 1 μm and about 0.1 nm in the 2−3 nm lateral scale. For the 0.5−2 nm scale, the changes in roughness are on a similar order to the noise: the lateral resolution of the AFM cantilever tip used for imaging is not known but is expected to be on this order. The important point is that the roughness changes on a variety of length scales, all the way from micrometer size down to at least 3 nm. As discussed above, roughness on all of these scales could change the accommodation coefficient.

CONCLUSIONS

The resistance to the flow of gas in a narrow channel can be controlled by applying an electric field to a solid. The change in resistance is tunable and can be repeatedly turned on or off. This electrically tunable resistance may be useful in NEMS, microfluidic devices, or other applications.

The example of field applied tunable resistance was achieved using a self-assembled monolayer on gold. For this example, the field also caused a reduction in the rms roughness of the solid. The correlation between the decrease in roughness and decrease in flow resistance suggests that the reduction in roughness may be the mechanism for the reduction in flow resistance. The *change* in roughness can be characterized by two dimensions: (a) the vertical dimension, which is 0−1 nm, and thus of appropriate magnitude to alter the trajectory of a (0.25 nm) nitrogen molecule, and (b) the horizontal dimension, which is mainly <2 to 500 nm. We show that for some model surfaces roughness on any horizontal scale can cause an increase in accommodation coefficient.

Independent of the means of producing changes in roughness (e.g., applying a voltage, changing the sample), the accommodation coefficient increases with the roughness over a range of a few nanometers for the samples studied here.

APPENDIX

In this Appendix we consider the effect of roughness on the tangential momentum accommodation coefficient (TMAC), σ, which is the fractional change in gas tangential momentum as a

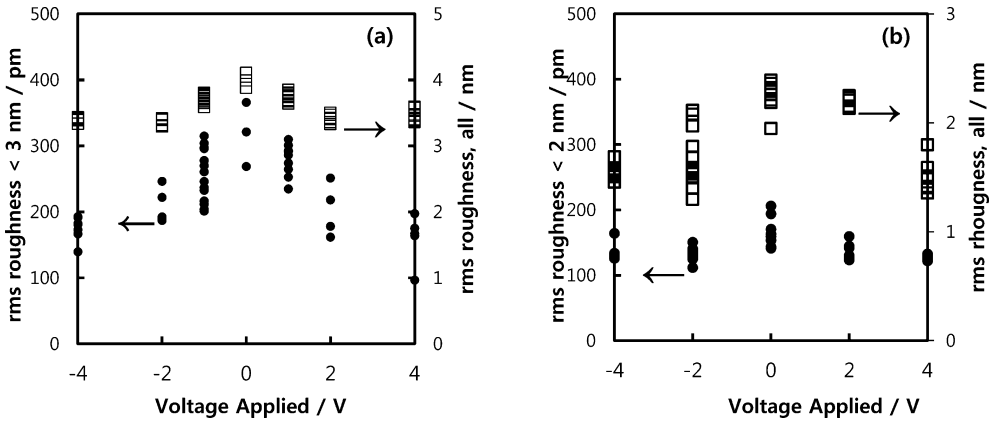

Figure 11. Measured roughness of ω-COOH films as a function of applied voltage, measured at different lateral scales. (a) 1 μm × 1 μm image with 2 nm pixels showing roughness on all scales (hollow squares, right axis) and filtered to retain only 2−3 nm scale lateral features (filled circles, left axis). (b) 0.5 μm × 0.5 μm image with 0.5 nm pixels showing roughness on all scales (hollow squares, right axis) and filtered to retain only 0.5−2 nm scale lateral features (filled circles, left axis).

dx.doi.org/10.1021/jp500579b | J. Phys. Chem. C 2014, 118, 7480−7488

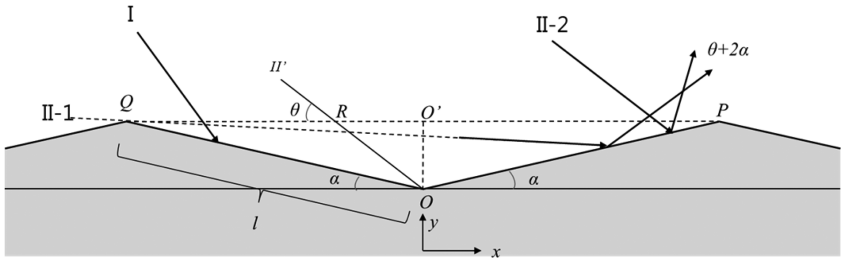

Figure 12. Schematic showing geometry of triangle-wave surface and some pathways. The origin is at point O, and the peaks are labeled Q and P. Arrows show the trajectory of particles, and dotted lines are guides for the eye. Angles of incidence (θ) and reflection (ϕ) are measured relative to the x-axis, not the local plane of the solid.

Table 1. Summary of Paths, Their Limits, and Probabilities

	negative slope			positive slope		
incident angle	probability[a]	ϕ[b]	path	probability	ϕ	path
$0 < \theta < \alpha$	0	none	none	1	$(\theta + 2\alpha)$	II-1
$\alpha < \theta < 2\alpha$	$(1/2)[1 - (\tan \alpha/\tan \theta)]$	$(4\alpha - \theta)$	I-3	$(1/2)[1 + (\tan \alpha/\tan \theta)]$	$(\theta + 2\alpha)$	II-2
$2\alpha < \theta < 3\alpha$	$(1/2)[1 - (\tan \alpha/\tan \theta)]r$	$(4\alpha - \theta)$	I-2ii	$(1/2)[1 + (\tan \alpha/\tan \theta)]$	$(\theta + 2\alpha)$	II-2
	$(1/2)[1 - (\tan \alpha/\tan \theta)](1 - r)$	$(\theta - 2\alpha)$	I-2i			
$3\alpha < \theta < \pi/2$	$(1/2)[1 - (\tan \alpha/\tan \theta)]$	$(\theta - 2\alpha)$	I-1	$(1/2)([1 + (\tan \alpha/\tan \theta)]$	$(\theta + 2\alpha)$	II-2

[a]Probability of a molecule colliding with slope within given range of incident angles. [b]Angle of reflection, relative to the x-axis. r is defined by eq 8.

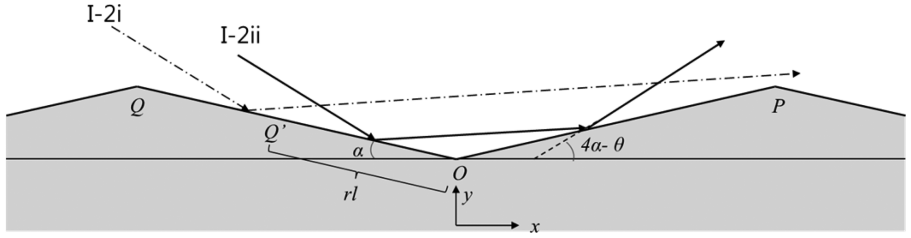

Figure 13. Details of path I-2.

result of the collision. For flows in the slip-flow regime, the TMAC can be used to calculate the effect of the solid surface on the damping.[2−4] For example, TMAC = 1 represents minimum slip whereas TMAC = 0 represents the full-slip boundary condition.

We consider the accommodation of a simple surface consisting of symmetrical inclined planes to show that, even for this simple case, roughness can affect the accommodation at both small and large lateral scales. First, we consider a perfectly smooth plate, with particles flowing from left to right. In reality, particles travel in both directions, but we only consider the net imbalance that is going to the right (x-direction) during net flow. This plate is infinitely wide (x direction) and long (z direction). These particles would collide with the plate with momentum of magnitude, A_{coll}, and angle, θ, *relative to the x-axis* that ranges from 0 to $\pi/2$ because of the assumption that the flow is in one direction. Therefore, the x-direction momentum or tangential momentum is $A_{coll} \cos \theta$. We assume that all collisions are elastic, and the surface is smooth, so the tangential momentum after the collision is also $A_{coll} \cos \theta$. Thus, $\sigma = 0$.

Next we examine the effect of roughness by considering a plate with a surface that is a symmetrical triangle wave, slope, α, in cross section in the x direction, and linear in cross section in the perpendicular direction (Figure 12). The origin is at point O, and the length of slope, OQ or OP, is l. The coordinates for P and Q are $P(l \cos \alpha, l \sin \alpha)$ and $Q(-l \cos \alpha, l \sin \alpha)$. The height of the ridges is less than the mean free path, so gas−gas collisions occur only beyond the topography ($y > l \sin \alpha$). For convenience, the slope OQ is called the negative slope and OP the positive slope. We examine the case where α is sufficiently small that gas−gas collisions within the roughness are not considered and there are at most two bounces with the solid. The particles still conserve momentum and energy, so all the collisions are specular but occur at tilted surfaces, leading to changes in x component of momentum. Thus, the incident angle remains θ, but the angle of reflection is ϕ.

We assume that the probability of a molecule crossing the line QP is the same at all points, and we classify collisions into two categories, depending on the site of the first collision with the surface: path I is for collision on negative slope, and path II is for collision with the positive slope. All the paths are summarized in Table 1.

Path II can be further divided into two parts: II-1 when $\theta < \alpha$ and II-2 when $\theta > \alpha$. When a molecule entering QP has $\theta < \alpha$, it cannot strike the negative slope (path II-1). However, if $\theta > \alpha$, some molecules strike the positive slope and some strike the negative slope. The probability of colliding on the positive slope, P(p.s.), can be calculated by calculating the ratio of the lengths of RP and QP. QP has a length $2l \cos \alpha$, and by considering the triangle RPO and the law of sines, RP has a length, $l \sin(\theta + \alpha)/\sin \theta$. Thus

$$P(\text{p.s.}) = \frac{1}{2}\left(1 + \frac{\tan \alpha}{\tan \theta}\right) \quad (6)$$

dx.doi.org/10.1021/jp500579b | J. Phys. Chem. C 2014, 118, 7480−7488

Molecules on trajectory II-1 or II-2 both have $\phi = \theta + 2\alpha$, resulting in the decrease in the tangential momentum.

Equation 6 shows the probability of a molecule colliding on the left side when $\theta > \alpha$, $P(\text{n.s.}) = 1 - P(\text{p.s.})$. This is the probability for path I.

Molecules following path I can have four different trajectories depending on the angle of first reflection, ϕ'. The particles colliding on the negative slope with the incident angle, θ, have the an angle of reflection, $\phi' = (\theta - 2\alpha)$.

If $\phi' > \alpha$, the particles cannot subsequently collide with the positive slope. $\phi' = (\theta - 2\alpha)$; therefore $\phi' > \alpha$ is equivalent to $\theta > 3\alpha$. This path is designated as I-1. The final angle of reflection is $\phi = (\theta - 2\alpha)$.

If $0 < \phi' < \alpha$, or $2\alpha < \theta < 3\alpha$, some molecules hit the negative slope, while others may fly over point P as depicted in Figure 13. The trajectories close to O have the possibility of striking both the negative and then the positive slope. We define the point Q′ such that, after collision to the left of Q′, the molecule misses the positive slope (path I-2i) whereas collision to the left of Q′ results in a further collision with positive slope (path I-2ii) OQ′ has length rl, r being the fraction of length l less than which value leads to double bounces. The equation for path I-2 colliding at Q′ is $y = \tan(\theta - 2\alpha)x + rl[\sin\alpha + \tan(\theta - 2\alpha)\cos\alpha]$, whereas the equation for OP is $l\cos\alpha$. Clearly the trajectory strikes OP if it does make it over the peak (at $x = l\cos\theta$), i.e., if

$$l\sin\alpha > \tan(\theta - 2\alpha)l\cos\alpha + rl[\sin\alpha + \tan(\theta - 2\alpha)\cos\alpha] \tag{7}$$

Thus

$$r = \frac{\tan\alpha - \tan(\theta - 2\alpha)}{\tan\alpha + \tan(\theta - 2\alpha)} \tag{8}$$

For path I-2i, the final angle $\phi = \theta - 2\alpha$, while for path I-2ii, $\phi = 4\alpha - \theta$.

If $\phi < 0$, or $\alpha < \theta < 2\alpha$, all molecules will strike the negative slope because the trajectory has a negative slope after the collision. This path I-3 has $\phi = 4\alpha - \theta$.

Table 1 summarizes all possible paths for collisions and their probability within the angle limits. The average tangential momentum after collision is found by integrating the product of the final momentum and the probability. For example, the contribution for path I-2ii is

$$\int_{2\alpha}^{3\alpha} \frac{1}{2}\left(1 - \frac{\tan\alpha}{\tan\theta}\right) rA_{\text{coll}}\cos(4\alpha - \theta)\,\mathrm{d}\theta \tag{9}$$

Our analysis ignores double bounces from right side then to left side (which can occur for θ near $\pi/2$ and for starting positions near $x = 0$) or >2 collisions with the solid. These multiple collisions become more likely with greater α so we consider only $0° < \alpha < 30°$. Figure 14 shows the calculated TMAC as a function of α. TMAC is defined by change in tangential momentum divided by initial tangential momentum. First we see that TMAC increases from zero for a flat surface up to higher values as the slope, α increases. That is, TMAC increases with roughness, as expected. Second, Table 1 and thus Figure 14 are independent of the horizontal scale (x-dimension) of the roughness. That is, *TMAC is increased by roughness at a variety of horizontal scales*. Note that our analysis ignores inelasticity of the collisions, which is a further mechanism for increasing TMAC.

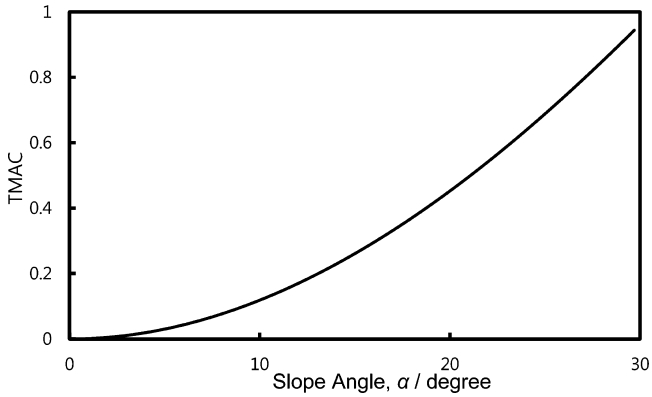

Figure 14. Calculated TMAC as a function of slope angle, α, for a surface that is sawtooth in cross section (Figure 12).

AUTHOR INFORMATION

Corresponding Author

*E-mail: wducker@vt.edu (W.A.D.).

Notes

The authors declare no competing financial interest.

ACKNOWLEDGMENTS

This research was funded by the National Science Foundation via Award CBET-0959228.

REFERENCES

(1) Seo, D.; Ducker, W. A. In Situ Control of Gas Flow by Modification of Gas-Solid Interactions. *Phys. Rev. Lett.* **2013**, *111*, 174502.

(2) Karniadakis, G.; Beskok, A.; Aluru, N. *Microflows and Nanoflows*; Springer-Verlag: New York, 2005.

(3) Sharipov, F.; Seleznev, V. Data on Internal Rarefied Gas Flows. *J. Phys. Chem. Ref. Data* **1998**, *27*, 657−706.

(4) Zhang, W. M.; Meng, G.; Wei, X. Y. A Review on Slip Models for Gas Microflows. *Microfluid. Nanofluid.* **2012**, *13*, 845−82.

(5) Chambers, A.; Chew, A. D.; Troup, A. P. Rotating-Disk Gauge for Absolute Total Pressure Measurement in High-Vacuum. *J. Vac. Sci. Technol., A* **1992**, *10*, 2655−60.

(6) Bentz, J. A.; Tompson, R. V.; Loyalka, S. K. The Spinning Rotor Gauge: Measurements of Viscosity, Velocity Slip Coefficients, and Tangential Momentum Accommodation Coefficients for N_2 and CH_4. *Vacuum* **1997**, *48*, 817−24.

(7) Martin, M. J.; Boyd, I. D. Momentum and Heat Transfer in a Laminar Boundary Layer with Slip Flow. *J. Thermophys. Heat Transfer* **2006**, *20*, 710−19.

(8) Arkilic, E. B.; Schmidt, M. A.; Breuer, K. S. Gaseous Slip Flow in Long Microchannels. *J. Microelectromech. Syst.* **1997**, *6*, 167−78.

(9) Honig, C. D. F.; Ducker, W. A. Effect of Molecularly-Thin Films on Lubrication Forces and Accommodation Coefficients in Air. *J. Phys. Chem. C* **2010**, *114*, 20114−19.

(10) Seo, D.; Mastropietro, D.; Ducker, W. A. Gas Flows near Solids Coated with Thin Water Films. *J. Phys. Chem. C* **2013**, *117*, 6235−44.

(11) Meng, H.; Hu, J. L. A Brief Review of Stimulus-Active Polymers Responsive to Thermal, Light, Magnetic, Electric, and Water/Solvent Stimuli. *J. Intell. Mater. Syst. Struct.* **2010**, *21*, 859−85.

(12) Kwon, I. C.; Bae, Y. H.; Kim, S. W. Electrically Erodible Polymer Gel for Controlled Release of Drugs. *Nature* **1991**, *354*, 291−93.

(13) Murdan, S. Electro-Responsive Drug Delivery from Hydrogels. *J. Controlled Release* **2003**, *92*, 1−17.

(14) Laurent, J.; Drezet, A.; Sellier, H.; Chevrier, J.; Huant, S. Large Variation in the Boundary-Condition Slippage for a Rarefied Gas Flowing between Two Surfaces. *Phys. Rev. Lett.* **2011**, 107.

(15) Lissandrello, C.; Yakhot, V.; Ekinci, K. L. Crossover from Hydrodynamics to the Kinetic Regime in Confined Nanoflows. *Phys. Rev. Lett.* **2012**, *108*.
(16) Honig, C. D. F.; Sader, J. E.; Mulvaney, P.; Ducker, W. A. Lubrication Forces in Air and Accommodation Coefficient Measured by a Thermal Damping Method Using an Atomic Force Microscope. *Phys. Rev. E* **2010**, *81*, 056305.
(17) Vinogradova, O. I. Drainage of a Thin Liquid-Film Confined between Hydrophobic Surfaces. *Langmuir* **1995**, *11*, 2213−20.
(18) Brenner, H. The Slow Motion of a Sphere through a Viscous Fluid Towards a Plane Surface. *Chem. Eng. Sci.* **1961**, *16*, 242−51.
(19) Sader, J. E. Frequency Response of Cantilever Beams Immersed in Viscous Fluids with Applications to the Atomic Force Microscope. *J. Appl. Phys.* **1998**, *84*, 64−76.
(20) Ducker, W. A.; Cook, R. F. Rapid Measurement of Static and Dynamic Surface Forces. *Appl. Phys. Lett.* **1990**, *56*, 2408−10.
(21) Zhang, W.; Turner, K. Frequency Dependent Fluid Damping of Micro/Nano Flexural Resonators: Experiment, Model and Analysis. *Sens. Actuators, A* **2007**, *134*, 594−99.
(22) Meyer, G.; Amer, N. M. Novel Optical Approach to Atomic Force Microscopy. *Appl. Phys. Lett.* **1988**, *53*, 1045−47.
(23) Bain, C. D.; Troughton, E. B.; Tao, Y. T.; Evall, J.; Whitesides, G. M.; Nuzzo, R. G. Formation of Monolayer Films by the Spontaneous Assembly of Organic Thiols from Solution onto Gold. *J. Am. Chem. Soc.* **1989**, *111*, 321−35.
(24) Dubois, L. H.; Nuzzo, R. G. Synthesis, Structure, and Properties of Model Organic Surfaces. *Annu. Rev. Phys. Chem.* **1992**, *43*, 437−63.

Chapter 8. Future Work

In Chapter 3 to Chapter 7, I described my work to describe the factors affecting the tangential momentum accommodation; in this chapter, I present applications of this knowledge.

8.1. Effect of Roughness

Chapter 6 and Chapter 7 claims *in situ* control of roughness changes the boundary conditions. It is intuitively obvious that gas flows easily along a smooth surface. A roughened surface would hinder gas flow. This idea was proven with a mathematical model in Chapter 7. However, the surfaces used in Chapter 6 and Chapter 7 are coated with molecules and have different substrate beneath them. There may be other factors. I believe there is no other factor, and the gases used in Chapter 6 and Chapter 7 have no chemical reaction, physisorption, chemisorption, and nothing else other other than the roughness affects the collision. Future work should directly test whether a change in roughness, *for the same material*, does cause a change in TMAC.

Therefore, while using the same experimental setup as in Chapter 4 to Chapter 7, I would use only one inert gas, nitrogen, and only one kind of substrate, mica. Mica would be bombarded with another *inert* gas, argon, to increase roughness with the minimum change in chemistry. This will exclude all other factors, but leaving roughness as one single variable in determining the slip length.

I have completed initial experiments using glass spheres and mica plates bombarded with energized argon at 200 mTorr for 0 minutes, 30 minutes, and 90 minutes. For the preliminary investigation, the slip length on both glass sphere and the mica plates were assumed the same.

Figure 1 in this chapter shows the result. For one set of experiments, one glass sphere was used while changing the mica surfaces. Figure 1 shows the "Combined Slip Length" which I define as the sum of slip lengths on both sphere and plate. The rms roughness was measured not with the actual sample used in Sets 1 and 2, but with the mica plates made with the same method for preparing the samples for experiments. Figure 1 clearly shows that an increase in time of plasma treatment leads to an increase in the roughness of the mica and a decrease in the slip length, as expected. Future work would involve (a) repeats of this experiment and (b) experiments to determine the slip length on the plate alone.

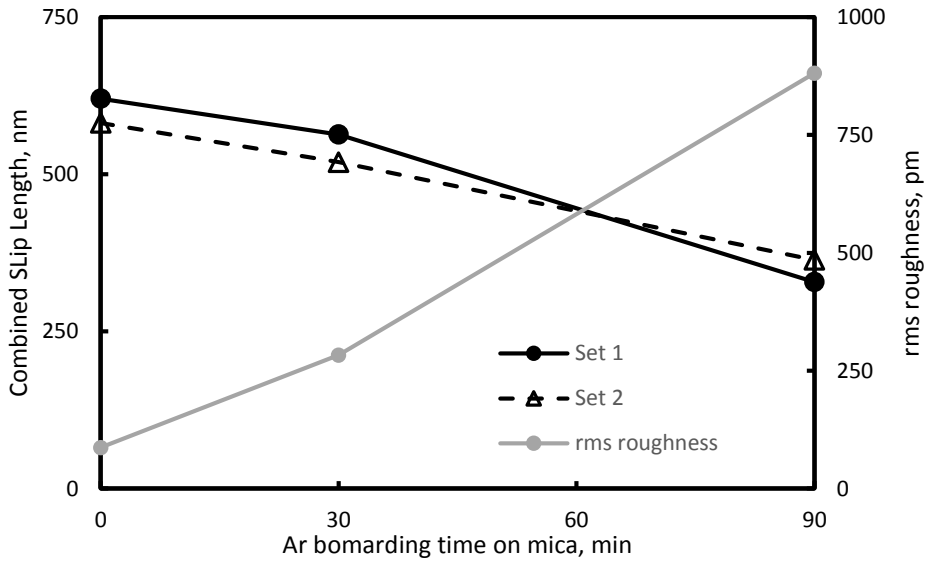

Figure 1 Combined slip length of a glass sphere and a mica plate bombarded with energized argon for different time duration, and rms roughenss of bombarded mica plates as function of bombarding time.

8.2. Roughening of Aerosol for Deep Lung Delivery

With the conviction that an increase in roughness of a surface increases the TMAC, in other words, increases the (repulsive lubrication force), this principle can be applied to aerosol medication to help cure Chronic Obstructive Pulmonary Diseases (COPDs).

COPDs are the third leading cause of mortality in the United States[55], and about 15 million adults have reported they have COPD in 2011.[56] Another form of lung disease, asthma, is more common both for adults and children. In the United States, 1 out of 12 adults and 1 out of 11 children have asthma, costing $56 billion each year.[57] The treatment of COPD, asthma, and other pulmonary diseases is to deliver medicine to the respiratory system via aerosol sprays into the mouth. Because the path into the lungs is not straight, this method of delivery naturally results in unnecessary deposition at the back of the mouth and near the entrance to the lung, rather than travel though the bronchioles. A longer travel distance of these aerosol particles is desired for better treatment.

The aim of this work is to enhance the travel distance of inhalant aerosol medication inside lungs by increasing the resistance between the aerosol and lung walls. As suggested by this thesis increased resistance is achieved with increased roughness. The method will be to roughen the surface of the aerosol with added surfactant. The added surfactant would increase the force around the aerosol particles by changing the flow boundary condition, preventing them from making contact with the inner surfaces of lungs. Whether the aerosol particles make contact with lung passage walls due to gravity, or due to curvature blocking the straight pathway of aerosol, this prevention would help utilize momentum along the wall, which would be unavailable after aerosol particles make contact. This project will enhance the knowledge regarding gas transport,

and may assist in developing an improved product. This idea is shown schematically in Figure 2 of this chapter.

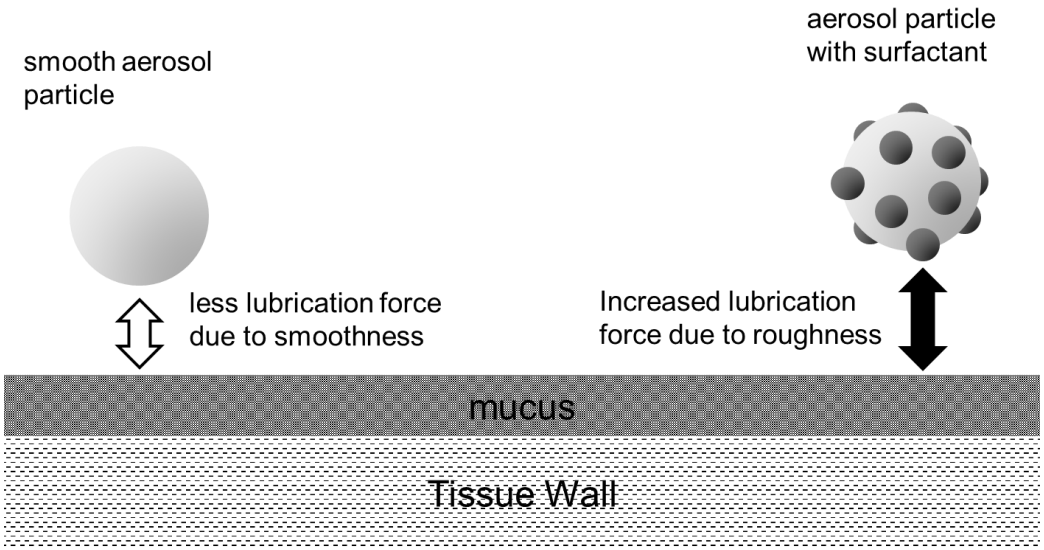

Figure 2 Schematics of roughened aerosol particles approaching tissue wall in the respiratory system

First a simulation will be done to examine whether this small change in roughness would actually make a difference in lubrication with computer simulation. Finite element method will be used to simulate the situation to see if there would be any change.

Adsorption of common and FDA-approved surfactant on the solution of common aerosol medication as ProAir ® HFA, or water vapor for mist treatment will be tested. For selected surfactants, the roughness of liquid surface adsorbed with the surfactants will be sought. This could be measured by X-ray scattering. The lubrication force could be measured by the methods described in this thesis. As a first step, the aerosol could be simulated with a solid particle that is coated with liquid, with and without surfactant. If the results show that lubrication does increase, the next step is actual spraying experiments. This would be tested in a mimic of the lung that is made from branching glass tubes.

8.3. Momentum Swing Separation

At the end of Chapter 5, the possible application towards gas separation was discussed. When the interaction of gas molecules and solid surface dominates over gas-gas interaction, i.e. $Kn \approx 1$, the differences in tangential momentum accommodation phenomena for different gases can be utilized to separate different gases. The theoretical discussion was presented in Chapter 5.

The actual experiments will be done in a batch system. First, a bundle of 1 μm glass capillary tubes will be fabricated so that greater volumes of gas can be tested. The inlets and outlets of these tube will be connected to one inlet and one outlet. The outlet will have a gas detector. For example in case of oxygen and carbon monoxide mixture, carbon monoxide detector and oxygen detector are installed. A batch of the mixture is connected to the inlet. The valve at the inlet is open and different molecules flow toward the outlet. If the level of minimum detection is the same for both detector, and if the velocity is actually different, the time profiles will be different.

The principle of chromatography can be used to detect molecules. For example gas chromatography discerns the difference in eluting time of different species caused by the interaction of the species (mobile phase) and the material coated or packed (stationery phase) inside a tubing (column). Another way is using mass spectroscopy, which ionize the samples, and differentiate them by their different response to electromagnetic field cause by different mass to charge ratio.

The success of this idea lead to the invention of Momentum Swing Separation with control valves operated by gas detectors.

Chapter 9. Monolithic Two Cantilever System

When I began my PhD, I was given two projects, one grew into the work published in this thesis and the other was discontinued due to the success of the now-published work. The discontinued work is described briefly here.

The purpose of this project was to measure the single molecule properties on polymers that were tethered between two cantilevers. That project ultimately became the subject of Milad Radiom's research.[58, 59] At the time that we worked together, it was apparent that a major problem was the thermal drift of the cantilevers, which changed the separation between the tips and prevented long measurements of polymer properties under a single extension. My objective was to produce a device where the thermal drift was negligible for hours, and the tips were separated by only a few tens of nanometers. The thermal drift was to be removed by using a device with no more than millimeter dimensions and with matched coefficients of expansion. The small gap was created by a combination of ion milling and deposition. Although the device was never used, a prototype was successfully fabricated and is described here.

1) Two commercial cantilevers were aligned so that the ends are touching. After aligning them, their position was fixed by freezing heat responsive epoxy glue binding them together. A pair of such cantilevers is shown in Figure 1(a) of this chapter and in more detail in Figure 1(b). Images were taken with a scanning probe microscope, which requires gold coating.
2) To simplify analysis of polymer properties, it is better if only a single molecule straddles the gap between the cantilevers. To decease the chance of tethering multiple molecules between the ends, the end were faceted with focused ion beam as shown in part (c).

3) To decrease the distance between the tips, more gold were deposited with gold sputtering.

4) To further decease the length of two ends over which molecules could bridge, further ion milling was performed as shown in part (d).

5) In an attempt to further decrease the gap, more gold was sputtered. However, as shown in part (e), the distance became larger. Later I found that the act of sputtering bent the cantilevers, which is shown in (e) (the cantilever on the right is bent forward). To fix the problem, more gold was sputtered onto the opposite side, and the cantilevers bent back.

The final result is shown in part (f): the closest distance between the cantilevers is 50 nm. 50 nm is about the contour length of a 10,000 monomers or the radius of gyration of a much longer polymer. Thus the cantilevers were positioned at the appropriate separation as required. It would be useful to have some variability in separation, for example a smaller separation for initial tethering and then a larger separation. Perhaps this could be achieved by temporarily heating the cantilevers and then returning to room temperature.

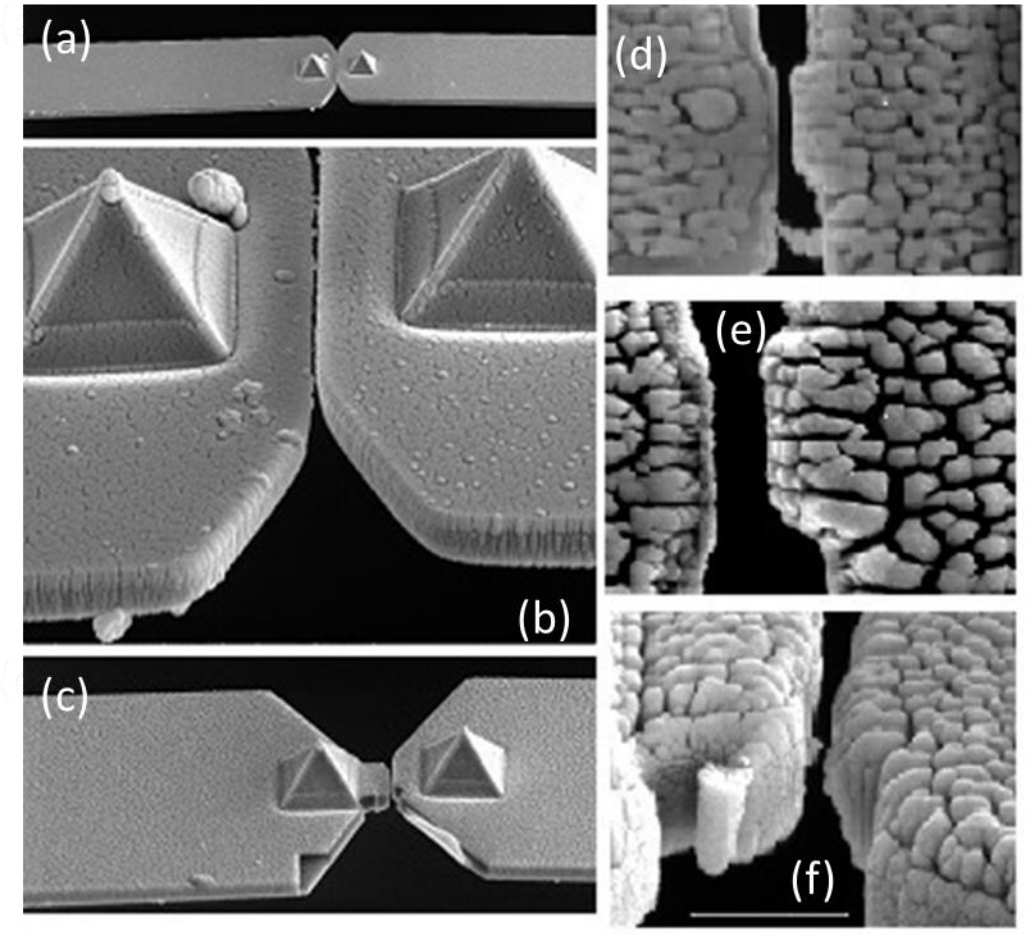

Figure 1. Steps for preparing monolithic, two cantilever system. Part (f) shows two fixed cantilevers separated by only 50 nm. The length of the white line is the scale of 1 μm.

Chapter 10. Conclusion

1) The tangential momentum accommodation coefficient (TMAC) and thus the slip length at a solid–gas interface is not constant, but depends on both the gas and the solid.

2) Different gas species can have a different accommodation coefficient on a single solid surface, and in principle, this effect could be used to separate gases. For a series of five gases, the TMAC decreases with greater molar mass.

3) The TMAC can be varied using surface films. A water film, created by changing the humidity, causes a complex change to the TMAC. Up unto about 80% humidity, TMAC decreased, but after that, TMAC increased significantly.

4) All results in this thesis are consistent with the idea that a rougher solid surfaces, produces a higher TMAC, resulting in a shorter slip length. This principles could, in principle, be used to deliver aerosol medication deeper into lungs.

5) Boundary lubrication can be altered in advance, by adsorbing surface molecules or controlled *in situ,* by changing the state of an adsorbed molecule. For an octadecyltrichlorosilane film on glass the surface becomes smoother as the temperature increases, and this leads to a decrease in TMAC. For a16-mercaptohexadecanethiol self-assembled monolayer on gold, the surface becomes smoother after an increase in the magnitude of the DC voltage applied parallel to the solid surface, and this also leads to a decrease in TMAC.

6) A microscopic gas pressure sensor can be constructed from an AFM cantilever.

References

The references here are for those used in Chapter 1, Chapter 2, Chapter 8, Chapter 9, and Chapter 10.

1 Vashchenkov, P.; Ivanov, M.; Krylov, A.; Levin, D. A.; Wysong, I. J.; Garcia, A. L., Numerical Simulations of High-Altitude Aerothermodynamics of a Promising Spacecraft Model, in *AIP Conference Proceedings-American Institute of Physics* (2011), p. 1337.

2 Mahaffy, P. R.; Webster, C. R.; Atreya, S. K.; Franz, H.; Wong, M.; Conrad, P. G.; Harpold, D.; Jones, J. J.; Leshin, L. A.; Manning, H.; Owen, T.; Pepin, R. O.; Squyres, S.; Trainer, M.; Team, M. S. Abundance and Isotopic Composition of Gases in the Martian Atmosphere from the Curiosity Rover. *Science* **2013**, *341*, 263-66.

3 Karniadakis, G.; Beskok, A.; Aluru, N. *Microflows and Nanoflows*; Springer-Verlag: New York, 2005.

4 Martini, V.; Bernardini, S.; Bendahan, M.; Aguir, K.; Perrier, P.; Graur, I. Microfluidic Gas Sensor with Integrated Pumping System. *Sensors and Actuators B: Chemical* **2012**, *170*, 45-50.

5 Velasquez-Garcia, L. F.; Gassend, B. L. P.; Akinwande, A. I. Cnt-Based Mems/Nems Gas Ionizers for Portable Mass Spectrometry Applications. *Microelectromechanical Systems, Journal of* **2010**, *19*, 484-93.

6 Kleinstreuer, C.; Feng, Y. Computational Analysis of Non-Spherical Particle Transport and Deposition in Shear Flow with Application to Lung Aerosol Dynamics—a Review. *Journal of Biomechanical Engineering* **2013**, *135*, 021008-08.

7 Peng, Y.; Lu, X.; Luo, J. Nanoscale Effect on Ultrathin Gas Film Lubrication in Hard Disk Drive. *Journal of Tribology* **2004**, *126*, 347-52.

8 Butt, H. J.; Jaschke, M. Calculation of Thermal Noise in Atomic-Force Microscopy. *Nanotechnology* **1995**, *6*, 1-7.

9 Saulson, P. R. Thermal Noise in Mechanical Experiments. *Physical Review D* **1990**, *42*, 2437-45.

10 Boskovic, S.; Chon, J. W. M.; Mulvaney, P.; Sader, J. E. Rheological Measurements Using Microcantilevers. *Journal of Rheology* **2002**, *46*, 891-99.

11 Paul, M. R.; Clark, M. T.; Cross, M. C. The Stochastic Dynamics of Micron and Nanoscale Elastic Cantilevers in Fluid: Fluctuations from Dissipation. *Nanotechnology* **2006**, *17*, 4502-13.

12 Paul, M. R.; Cross, M. C. Stochastic Dynamics of Nanoscale Mechanical Oscillators Immersed in a Viscous Fluid. *Phys Rev Lett* **2004**, *92*.

13 Frangi, A.; Spinola, G.; Vigna, B. On the Evaluation of Damping in Mems in the Slip-Flow Regime. *International Journal for Numerical Methods in Engineering* **2006**, *68*, 1031-51.

14 Honig, C. D. F.; Sader, J. E.; Mulvaney, P.; Ducker, W. A. Lubrication Forces in Air and Accommodation Coefficient Measured by a Thermal Damping Method Using an Atomic Force Microscope. *Physical Review E* **2010**, *81*, 056305.

15 Ezquerra Larrodé, F.; Housiadas, C.; Drossinos, Y. Slip-Flow Heat Transfer in Circular Tubes. *International Journal of Heat and Mass Transfer* **2000**, *43*, 2669-80.

16 Maxwell, J. C. On Stresses in Rarefied Gases Arising from Inequalities of Temperature. *Philos. T. Roy. Soc.* **1879**, *170*, 231 - 56.

17 Karniadakis, G.; Beşkök, A. *Micro Flows : Fundamentals and Simulation*; Springer: New York, 2002.

18 Lilley, C. R.; Sader, J. E. Velocity Profile in the Knudsen Layer According to the Boltzmann Equation. *P Roy Soc a-Math Phy* **2008**, *464*, 2015-35.

19 Barber, R. W.; Emerson, D. R. Challenges in Modeling Gas-Phase Flow in Microchannels: From Slip to Transition. *Heat Transfer Engineering* **2006**, *27*, 3-12.

20 Tekasakul, P.; Bentz, J.; Tompson, R.; Loyalka, S. The Spinning Rotor Gauge: Measurements of Viscosity, Velocity Slip Coefficients, and Tangential Momentum Accommodation Coefficients. *Journal of Vacuum Science & Technology A* **1996**, *14*, 2946-52.

21 Vinogradova, O. I. Drainage of a Thin Liquid-Film Confined between Hydrophobic Surfaces. *Langmuir* **1995**, *11*, 2213-20.

22 Seo, D.; Mastropietro, D.; Ducker, W. A. Gas Flows near Solids Coated with Thin Water Films. *Journal of Physical Chemistry C* **2013**, *117*, 6235-44.

23 Bianco, S.; Cocuzza, M.; Ferrero, S.; Giuri, E.; Piacenza, G.; Pirri, C. F.; Ricci, A.; Scaltrito, L.; Bich, D.; Merialdo, A.; Schina, P.; Correale, R. Silicon Resonant Microcantilevers for Absolute Pressure Measurement. *Journal of Vacuum Science & Technology B* **2006**, *24*, 1803-09.

24 Christian, R. G. The Theory of Oscillating-Vane Vacuum Gauges. *Vacuum* **1966**, *16*, 175-78.

25 Bao, M. H.; Yang, H.; Yin, H.; Sun, Y. C. Energy Transfer Model for Squeeze-Film Air Damping in Low Vacuum. *Journal of Micromechanics and Microengineering* **2002**, *12*, 341-46.

26 Hosaka, H.; Itao, K.; Kuroda, S. Damping Characteristics of Beam-Shaped Micro-Oscillators. *Sensors and Actuators a-Physical* **1995**, *49*, 87-95.

27 Lissandrello, C.; Yakhot, V.; Ekinci, K. L. Crossover from Hydrodynamics to the Kinetic Regime in Confined Nanoflows. *Phys Rev Lett* **2012**, *108*, 084501.

28 Lübbe, J.; Schnieder, H.; Reichling, M. Pressure Dependence of the Q-Factor of Cantilevers Used for Nc-Afm. *e-J. Surf. Sci. Nanotech.* **2011**, *9*, 30-33.

29 Keskar, G.; Elliott, B.; Gaillard, J.; Skove, M. J.; Rao, A. M. Using Electric Actuation and Detection of Oscillations in Microcantilevers for Pressure Measurements. *Sensors and Actuators a-Physical* **2008**, *147*, 203-09.

30 Fremerey, J. The Spinning Rotor Gauge. *Journal of Vacuum Science & Technology A* **1985**, *3*, 1715-20.

31 Bentz, J. A.; Tompson, R. V.; Loyalka, S. K. The Spinning Rotor Gauge: Measurements of Viscosity, Velocity Slip Coefficients, and Tangential Momentum Accommodation Coefficients for N-2 and Ch4. *Vacuum* **1997**, *48*, 817-24.

32 Gabis, D. H.; Loyalka, S. K.; Storvick, T. S. Measurements of the Tangential Momentum Accommodation Coefficient in the Transition Flow Regime with a Spinning Rotor Gauge. *Journal of Vacuum Science & Technology A* **1996**, *14*, 2592-98.

33 Acharya, T.; Falgoust, J.; Martin, M. J. Measurement of Viscous Drag on a Disc Rotating in a Low Pressure Gas. *American Institute of Aeronautics and Astronautics, AIAA-2012-3192, New Orleans* **2012**.

34 Loyalka, S. K. Theory of the Spinning Rotor Gauge in the Slip Regime. *Journal of Vacuum Science & Technology A* **1996**, *14*, 2940-45.

35 Colin, S.; Lalonde, P.; Caen, R. Validation of a Second-Order Slip Flow Model in Rectangular Microchannels. *Heat Transfer Engineering* **2004**, *25*, 23-30.

36 Arkilic, E. B.; Schmidt, M. A.; Breuer, K. S. Gaseous Slip Flow in Long Microchannels. *J Microelectromech S* **1997**, *6*, 167-78.

37 Arkilic, E. B.; Breuer, K. S.; Schmidt, M. A. Mass Flow and Tangential Momentum Accommodation in Silicon Micromachined Channels. *Journal of Fluid Mechanics* **2001**, *437*, 29-43.

38 Deissler, R. G. An Analysis of Second-Order Slip Flow and Temperature-Jump Boundary Conditions for Rarefied Gases. *International Journal of Heat and Mass Transfer* **1964**, *7*, 681-94.

39 Colin, C. A., StÉphane High-Order Boundary Conditions for Gaseous Flows in Rectangular Microducts. *Microscale Thermophysical Engineering* **2001**, *5*, 41-54.

40 Laurent, J.; Drezet, A.; Sellier, H.; Chevrier, J.; Huant, S. Large Variation in the Boundary-Condition Slippage for a Rarefied Gas Flowing between Two Surfaces. *Phys Rev Lett* **2011**, *107*, 164501.

41 Honig, C. D. F.; Ducker, W. A. Effect of Molecularly-Thin Films on Lubrication Forces and Accommodation Coefficients in Air. *Journal of Physical Chemistry C* **2010**, *114*, 20114-19.

42 Hsieh, S.-S.; Tsai, H.-H.; Lin, C.-Y.; Huang, C.-F.; Chien, C.-M. Gas Flow in a Long Microchannel. *International Journal of Heat and Mass Transfer* **2004**, *47*, 3877-87.

43 Cooper, S. M.; Cruden, B. A.; Meyyappan, M.; Raju, R.; Roy, S. Gas Transport Characteristics through a Carbon Nanotubule. *Nano Letters* **2003**, *4*, 377-81.

44 Arya, G.; Chang, H. C.; Maginn, E. J. Molecular Simulations of Knudsen Wall-Slip: Effect of Wall Morphology. *Mol Simulat* **2003**, *29*, 697-709.

45 Sedmik, R. I. P.; Borghesani, A. F.; Heeck, K.; Iannuzzi, D. Hydrodynamic Force Measurements under Precisely Controlled Conditions: Correlation of Slip Parameters with the Mean Free Path. *Phys Fluids* **2013**, *25*, 042103.

46 Perrier, P.; Graur, I. A.; Ewart, T.; Meolans, J. G. Mass Flow Rate Measurements in Microtubes: From Hydrodynamic to near Free Molecular Regime. *Phys Fluids* **2011**, *23*, 042004.

47 Ewart, T.; Perrier, P.; Graur, I.; Meolans, J. G. Tangential Momemtum Accommodation in Microtube. *Microfluid Nanofluid* **2007**, *3*, 689-95.

48 Graur, I. A.; Perrier, P.; Ghozlani, W.; Meolans, J. G. Measurements of Tangential Momentum Accommodation Coefficient for Various Gases in Plane Microchannel. *Phys Fluids* **2009**, *21*, 102004.

49 Raman, A.; Melcher, J.; Tung, R. Cantilever Dynamics in Atomic Force Microscopy. *Nano Today* **2008**, *3*, 20-27.

50 Barth, F. G.; Humphrey, J. A.; Secomb, T. W. *Sensors and Sensing in Biology and Engineering*; Springer: 2003.

51 Ducker, W. A.; Senden, T. J.; Pashley, R. M. Direct Measurement of Colloidal Forces Using an Atomic Force Microscope. *Nature* **1991**, *353*, 239-41.

52 Systems, S. R., 'Dsp Lock-in Amplifier Model Sr830', Standford Research Systems, (1999) <http://www.thinksrs.com/downloads/PDFs/Manuals/SR830m.pdf> [Accessed September 1st 2014].

53 Ducker, W. A.; Cook, R. F. Rapid Measurement of Static and Dynamic Surface Forces. *Applied Physics Letters* **1990**, *56*, 2408-10.

54 Hutter, J. L.; Bechhoefer, J. Calibration of Atomic-Force Microscope Tips. *Rev Sci Instrum* **1993**, *64*, 1868-73.

55 Hoyert, D. L.; Xu, J. Deaths: Preliminary Data for 2011. *National vital statistics reports* **2012**, *61*, 1-51.

56 Prevention, C. f. D. C. a. Chronic Obstructive Pulmonary Disease among Adults — United States, 2011. *Morbidity and Mortality Weekly Report (MMWR)* **2012**, *61*.

57 Center for Disease Control and Prevention, Asthma's Impact on the Nation, (2014) <http://www.cdc.gov/asthma/impacts_nation/asthmafactsheet.pdf> [Accessed June 12th 2014].

58 Radiom, M.; Honig, C. D. F.; Walz, J. Y.; Paul, M. R.; Ducker, W. A. A Correlation Force Spectrometer for Single Molecule Measurements under Tensile Load. *Journal of Applied Physics* **2013**, *113*.

59 Radiom, M.; Robbins, B.; Honig, C. D. F.; Walz, J. Y.; Paul, M. R.; Ducker, W. A. Rheology of Fluids Measured by Correlation Force Spectroscopy. *Rev Sci Instrum* **2012**, *83*.